Introduction

Contents

1

Introduction to the Satellite observations

1.1 Satellite observations

The purpose of this chapter is to give a brief introduction to the principles behind the satellite observations of sea surface temperature and sea surface height. The attention will be given to the temporal and spatial sampling of the satellites in areas relevant to this study. In addition, only corrections and associated errors of importance to this study will be discussed. For a thorough review on the principles behind the satellite altimetry and the corrections applied to the measurements the reader is referred to Chelton et al. (2001) for altimetry and Emery et al. (2001), Barton (1995) for sea surface temperatures. Finally, this chapter is also used to describe the different versions of the altimetry data set that are used throughout the thesis.

1.2 Satellite altimetry

The satellite observations of sea surface heights (SSH) that will be used in the following chapters are from the French/American satellite TOPEX/POSEIDON (T/P) which was launched in September 1992 and (as of March 2002) still provides data, and the European satellites ERS 1 (July 1991-June 1996) and ERS 2 (April 1995-present). The T/P and the ERS 2 satellites have been flown in the same orbit configuration since launch with exact repeat periods of 10 days and 35 days, respectively. Whereas the T/P satellite is a dedicated mission to study the sea surface topography, the ERS satellites carry several instruments besides the altimeter such as the Synthetic Aperture Radar (SAR) and the Along Track Scanning Radiometer (ATSR). The multipurpose mission of ERS 1 is reflected in different orbit configurations with repeat cycles of 3, 35 and 168 days. Data are used here only from the ERS 1 phase C and G where the repeat period was 35.0 days resulting in a data gap of 15 months.

1.2.1 Principle

The three satellites T/P, ERS 1 and 2 use the radar principle to measure the height of the sea surface. The satellites emit microwave radar pulses towards the sea surface and measure the return time of the pulse reflected at the sea surface. As the atmosphere is very transmittant to the microwaves emitted by the T/P and ERS satellites, the observations are not limited by cloud cover but the propagation speed of the signal depends on the atmospheric and oceanic conditions. The impact from these processes are important to know in detail in order to convert the measured time into a distance between the satellite and the sea surface. Furthermore, through

a precise determination of the satellite orbit the distance is converted into the desired observation of sea surface height above a reference ellipsoid.

The height above a reference ellipsoid includes the marine geoid which is the gravitational equipotential surface. The dynamic topography is the difference between the reference ellipsoid and can be used to estimate the barotropic currents. A severe limitation in the current estimation at the moment is the uncertainty in the geoid (Fu and Chelton, 2001) that does not allow to resolve details in the absolute current circulation.

The measurement principle of the satellite altimetry observations is shown in figure 1.1 where some of the atmospheric processes that influence the observations are also

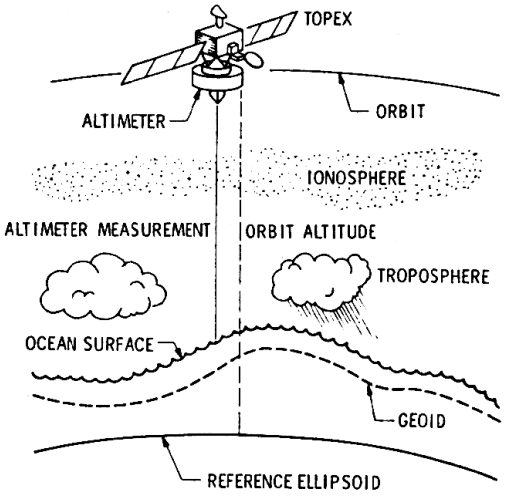

Figure 1.1: Measurement principle of the satellite altimetry observations, after Parke et al. (1987).

indicated. It is outside the scope of this study to describe and discuss all the 40 algorithms and corrections and only selected processes will be described here for the T/P satellite.

Dry Troposphere: The dry component of the atmosphere delays the propagation of the signal compared to the speed of light in vacuum. Corrected by assuming perfect gas law and hydrostatic equilibrium. Sea level pressure from operational meteorological model is used.

Wet Troposphere: Propagation delay caused by the atmospheric water vapor. Correction based on the estimated atmospheric water content from the T/P onboard Microwave Radiometer.

Ionospheric Refraction: The presence of free electrons primarily in the ionosphere, affects the propagation velocity of the radio pulse. As the ionospheric delay is frequency dependent, the correction can be obtained from a dual-frequency altimeter like the TOPEX instrument.

EM bias: It is observed that troughs of ocean surface waves reflect radar pulses better than crests. This effect is called Electro-Magnetic (EM) bias. Thus, EM bias is dependent on the significant wave height, which can be assessed from the shape of the reflected radar signal.

Orbit determination Crucial to the accuracy of the observations is a precise determination of the satellite orbit and much effort has been put into development of this topic. The orbit determination is a combination of a complex mathematical model for the motion of the satellite and precise observations of the position and velocity. The T/P utilizes positioning systems such as Global Positioning System (GPS), Satellite Laser Ranging (SLR) and Doppler Orbitography and Radiopositioning Intgrated by Satellite (DORIS) to determine the position.

1.2.2 Temporal and spatial resolution

As discussed in Parke et al. (1987), the sampling characteristics of the satellite are given when three orbital parameters have been determined: The altitude of the satellite, the inclination of the orbit and the repeat period. The parameters chosen for the two satellites are shown in table 1.1 where it is clear that the two satellites have

	TOPEX/POSEIDON	ERS 1+2 (35 days)
Altitude (km)	1336	800
Track spacing equator (km)	316	77
Repeat period (days)	9.916	35.0
Orbit inclination (degrees)	66.0	98.5
Turning latitude (degrees)	66.2	80
Distance of alongtrack obs. (km)	6	7

Table 1.1: Selected satellite parameters for the two satellites

distinctly different sampling characteristics with a higher temporal and lower spatial sampling of the T/P satellite compared to the ERS. Another important difference is the turning latitude of the satellites. Whereas the T/P satellite with turning latitude of 66.2°N covers most of the Scotland-Greenland ridge but not all of the Denmark Strait, the ERS satellites with a maximum latitude of 80° cover all of the ridge and the Nordic Seas north of the ridge. The spatial sampling of the satellites are shown in figure 1.2 for T/P over the northern North Atlantic and for both T/P and ERS 1+2 in the Denmark Strait. It is clear from the figure that as the turning latitude of the satellites is approached, the ground tracks become closer and closer with larger crossing angles at cross-overs. With the turning latitude of 66.2 for the T/P satellite, the sampling in e.g. the Denmark Strait between Greenland and Iceland is thus very dense compared to lower latitudes. This will be used advantageous in chapter 2.

An important effect determined by the orbital characteristics is the tidal aliasing frequencies. As the repeat periods of 10 and 35 days of the satellites are far to long to resolve e.g. the diurnal and semidiurnal tidal variations, these constituent will alias into the satellite observations as signals with longer periods (see Schlax and Chelton,

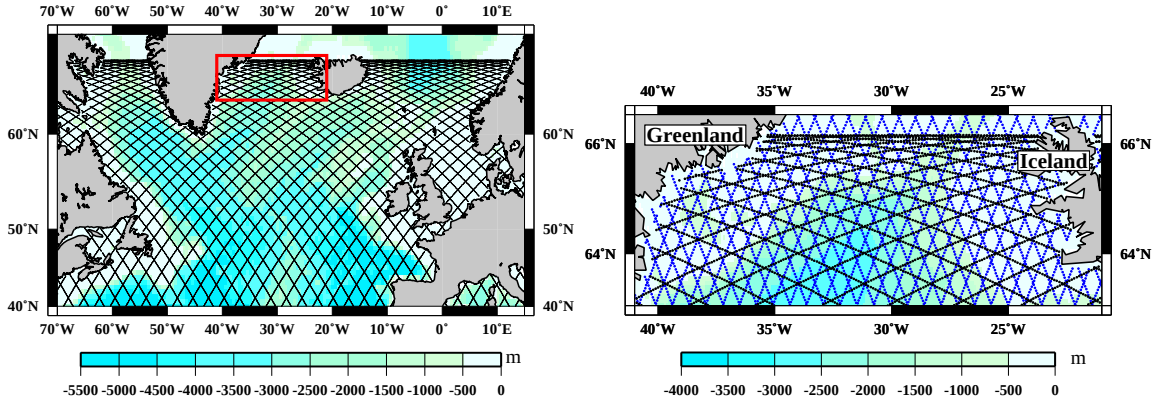

Figure 1.2: Left: T/P satellite ground tracks (black) for the North Atlantic. Right: T/P (black) and ERS (blue) satellite ground tracks for the Denmark Strait area outlined with the red box in left figure. The bathymetry is indicated with the colors.

1994). Favorable aliasing periods that did not coincide with geophysical signals was a major priority with the T/P mission. The selected T/P orbit, result in aliasing periods of major constituents like M_2 and S_2 into variations around 60 days.

Similar priority to the aliasing issue was not given when the ERS orbits were determined which resulted in problematic aliasing periods. The 35 days orbit that was chosen is a sun synchronous orbit where the satellite always have the same relative position to the sun. This means that the semidiurnal tidal constituent S_2 always is sampled with the same phase and is impossible to determine from the ERS satellite. Furthermore, the two large diurnal constituents, K_1 and P_1 alias exactly into the annual period of 365.25 days, which is unfortunate compared to the important geophysical processes of interest with an annual period. The tidal aliasing periods for the six major tidal constituents are summarized in table 1.2 for the T/P and the ERS satellites.

Tide	Period, (hours)	T/P aliasing period (days)	ERS 1+2 aliasing period (days)
M_2	12.42	62.11	94.49
S_2	12.00	58.74	∞
N_2	12.66	49.53	97.39
K_1	23.93	173.19	365.25
O_1	25.82	45.71	75.07
P_1	24.07	88.89	365.25

Table 1.2: Tidal periods and T/P and ERS 1+2 aliasing periods for the six major diurnal and semidiurnal tidal constituents. The table is taken from Chelton et al. (2001).

The contamination from land effects may play a role for the North Sea study (chapter 4) and sea ice will be present in some of the observations in the Denmark

Strait (chapter 2). Brooks et al. (1990) showed that in the Geosat data, effects from islands can give an error of 4 meters in the sea surface height measurement and it is therefore important to assess how far from the coast the observations are influenced. The circular area of the ocean that reflects the radar beam (the footprint) is of the order of 4–8 km in diameter and depends upon the significant wave height. For land or sea-ice contamination, the beam width of the antenna may be important as returns may come from anywhere within it. The 1.5 m antenna on the T/P satellite corresponds to an antenna beam width of 25 km in diameter. The distance within land that was influenced by land effects was determined by Høyer (1999) to be about 30 kilometers off the Chilean Coast. However, this was in the presence of the Andes mountain chain with steep land surface slopes close to the sea. The low lying areas surrounding the North Sea are more suitable for retrieving altimetry observations and the distance influenced by land effect is probably reduced to 15-20 km. Accurate altimetry observations can, however, be obtained as close as 10 km off the Danish west coast as will be shown in chapter 4.

The effect of ice will drastically influence the radar altimetry signal as described in Zwally and Brenner (2001). The contaminated observations are flagged by the Pathfinder team. The Denmark Strait region is the only region used in this thesis where the presence of sea ice is a concern and the influence from sea ice was seen in the lower data return, compared to rest of the North Atlantic region. The data return was observed to decrease towards the East Greenland shelf where the highest concentration of sea ice is found in the East Greenland current. After editing the data, only about 80 percent of the T/P data were available in the Denmark Strait region compared to 94 % for the North Atlantic region (regions are outlined in figure 1.2).

1.2.3 Corrections/Accuracy

The key to the success of the T/P satellite lies in the high accuracy that has been obtained in the estimation of the SSH. The high accuracy is a result of more than 40 corrections and algorithms applied to the radar measurements to convert the observed time difference into a SSH elevation.

The error budget for a single altimeter observation is listed in table 1.3 together with the errors of the individual corrections The table only shows the errors on individual corrections for the T/P satellite because an equivalent analysis of the errors has not been made for the ERS satellites. As displayed in the table the largest error contribution are from the orbit determination, the EM bias and from noise in the radar altimeter. Together with errors in the other corrections they result in a root-sum-square error of 4.1 cm for a single observation in a T/P track. This is a remarkable achievement, and much better than the pre-launch requirement of 13.7 cm (Fu et al., 1994). The errors on the ERS observations are 4-5 centimeters higher primarily due to imprecision in the orbit determination, but currently work is being made to reduce these errors to 5 cm (Scharroo and Visser, 1998).

The accuracy described above applies to a single observation in one track, but spatial and temporal averaging can increase the accuracy even more because of the decorrelation scales associated with some of the errors. As described in Tapley et al.

T/P errors	Altimeter noise	1.7
	Ionosphere	0.5
	EM bias	2.0
	Skewness	1.2
	Dry Troposphere	0.7
	Wet Troposphere	1.1
	T/P Orbit	2.5
Total T/P	T/P RSS	4.1
ERS errors	ERS measurement prec	3
	ERS 1 orbit	8-15
	ERS 2 orbit	7-8

Table 1.3: Assessment of measurement errors in centimeters for the altimetry satellites. RSS is root-sum-square and values are taken from Chelton et al. (2001).

(1994) the spatial scales of instrument noise and the wet troposphere and Ionosphere corrections are from 20-50 km. The associated T/P accuracies of 1.7, 1.1 and 0.5 cm, respectively, can thus be significantly enhanced by along track averaging over larger spatial scales. The reduction depends upon the spatial scales of the errors compared to the averaging scales but Cheney et al. (1994) showed that an accuracy of 2 cm can be obtained when averaging T/P data over a few hundred km.

The error in the determination of the orbit is a significant error in the total budget and with decorrelation scales of 10000 km (Tapley et al., 1994) it is clear that along track smoothing will not reduce this error. The same problem exist for the dry troposphere correction with decorrelation scales of 1000 km. However, as it will be discussed in chapter 2, the large spatial scales are useful when detecting variations in the SSH standard deviations along ground tracks. The large spatial scales of the orbit errors means that these errors will only affect the background noise level along the track. The uncertainty in detecting variations away from the background level are thus only from errors in the corrections with small (< 100 km) error decorrelation scales. Neglecting the large scale errors in the error estimate thus reduces the root-sum-square to 3.1 cm.

In addition to these corrections, the sea surface height variations from tides and the inverse barometer effect are regarded as unwanted signals in chapter 2 and 3 to be removed. The tidal signals are subtracted with a state of the art global ocean tide model (GOT99.2) which is believed to agree within 2-3 cm in the deep ocean (Shum et al., 1997). The correction for atmospheric loading depends upon an isostatic inverted barometer assumption Gill (1982), where an increase in the sea level pressure of 1 mbar results in an instantaneous sea level fall of 9.95 mm. The errors associated with this effect is estimated to be about 10% of the response (Chelton et al., 2001). In the region of the northern North Sea where low pressure systems travels through, the SSH variability from the inverse barometer effect can be up to 7 cm, as discussed in chapter 4.

1.2.4 Version

The altimeter data used throughout this thesis are obtained from the NOAA/NASA at the Goddard Space Flight Center where the Pathfinder team processed and validated all the altimetry data as described in Koblinsky et al. (1999a,b). The altimetry data consist of exact repeat observations from TOPEX/POSEIDON and merged ERS data from ERS 1 phase C (18 repeat cycles), ERS 1 phase G (13 repeat cycles) and ERS 2. The merged ERS 1+2 record contains a gap of 15 months and an overlap of 10 months and the Pathfinder team have used cross-over residuals to compute and correct for offsets between the missions.

As the work in this thesis extend over a period of three years, the data versions and number of observations differ between the different chapters. The versions used for this study are summarized in table 1.4 where the repeat cycles and the time span

Version	Repeat cycles	Dates	Chapter	Note
T/P 5	232	Sep 1992 - Dec 1998	2	All corr.
T/P 8.2	294	Sep 1992 - Sep 2000	3	All corr.
T/P 8.4noib	300	Sep 1992 - Nov 2000	4	No I.B., No tide
ERS 5	31+50	April 1992 - Aug 1998	2	All corr.
ERS 5noib	31+50	April 1992 - Aug 1998	4	No I.B., No tide

Table 1.4: Overview of the different satellite altimetry data versions used for this study and the chapters where they are used. The data set where the inverse barometer effect is not removed are marked with: No I.B.. Data set where no tidal subtraction has been performed are marked with: No tide

of the observations are also included. Tides have been removed with a global ocean tide model unless stated otherwise.

Editing the data

Rain influences the microwave signals by attenuation and the effect is difficult to correct for. To avoid large errors from this effect, observations with heavy rain are flagged by the Pathfinder team and discarded in the analysis

If any of the geophysical corrections applied to the observations attained unrealistic values an edit flag was set by the Pathfinder team and the flagged observations were discard from further analysis. The variations in the mean sea surface can induce a SSH variability signal when the observations in a ground track are displaced from the exact repeat repeat positions. To minimize the influence from this effect, the Pathfinder team used a mean sea surface to interpolate off-track observations to the repeat ground track. For T/P version 5.2, the mean sea surface was the UTCSR mean sea surface from university of Texas. In versions 8.1, 8.4 and ERS version 5 the GSFC00.1 mean sea surface from Goddard Space flight center has been used. The validity of this correction of course depends on the accuracy of the mean sea surface and as will be shown in chapter 2 a significant variability signal may still be found in regions with large variations in mean sea surface. An edit flag was set if the crosstrack distance between the observations and the repeat ground was more than 1 km and this was used to discard data in chapter 2. The final editing of bad data consisted of applying a 3-standard deviation filter to the time series in every point to remove outliers. This was tested and improved the quality of the data.

1.3 Sea surface temperature from satellites

The sea surface temperatures (SST) that will be used in chapter 2 and 3 are obtained from the Advanced Very High Resolution Radiometer (AVHRR) observations onboard the polar orbiting NOAA satellites. In contrast to the radar altimeters described above, the AVHRR instrument is a passive sensor that only measures electromagnetic radiation without emitting any itself. The observations are performed in 5 spectral bands as listed in table 1.5 ranging from red in channel 1 to thermal infrared in

AVHRR Channels	1	2	3	4	5
Wavelengths (μm)	0.58-0.68	0.73-1.10	3.55-3.93	10-3-11.3	11.5-12.5

Table 1.5: Wavelengths of the different channels in the AVHRR radiometer

channel 4 and 5. The first satellite that carried a 5-channel AVHRR instrument was the NOAA-7 which was launched in 1981. Subsequent launches of NOAA-9 in 1984, NOAA-11 in 1988, NOAA-12 in 1991 and NOAA-14 in 1994 has ensured that at least one satellite has been operating since.

The SST data that will be described here and used throughout this thesis are processed by the NOAA/NASA AVHRR Pathfinder team which has as a main goal to provide a global SST product that is processed consistently throughout the years with observations (see e.g. Kilpatrick et al., 2001).

1.3.1 Principle

The AVHRR imager uses a cross track scanning system to retrieve observations in a 2700 km wide area perpendicular to the direction of flight. The resolution immediately under the satellite (nadir) is up to 1.1 km for regional studies and 4 km for global studies.

The infra red observations from channel 4 and 5 are the most often used for estimating the sea surface temperature. The advantages of these channels are indicated in figure 1.3 where the thermal emission curves for a black body at temperature T is

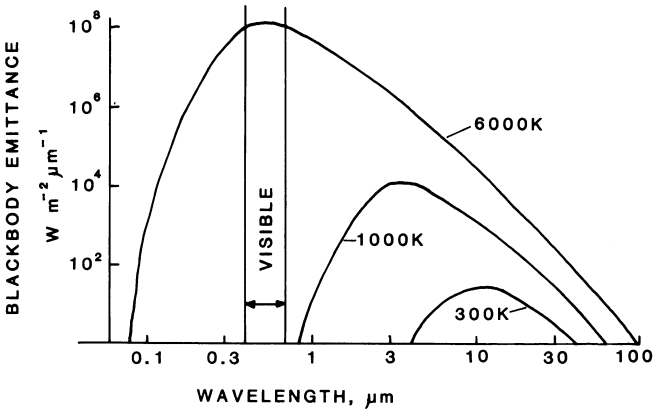

Figure 1.3: Top: Black body emittance as a function of wavelength for different temperatures according to equation 1.1. 6000 Kelvin corresponds to the temperature of the Sun and 300 Kelvin to the Earth. After Robinson (1985)

shown as a function of wavelengths. The curves in the figure are shown according to Plancks radiation law

$$M_\lambda = \frac{C_1}{\lambda^5(exp(C_2/\lambda T) - 1)} \tag{1.1}$$

Where M_λ is the emittance at a given wavelength, λ and C_1 and C_2 are constants. It is clear from the figure that the emittance curve for a black body with temperature equal to the surface of the Earth (300 K) has a maximum in the thermal infrared band around 10 μm wavelength. The emittance curve for a black body with temperature like the sun (6000 K) is also seen in figure 1.3 with a peak in the visible. The infra red emittance for the Sun is much higher than for the Earth in the figure but this is not the case when the distance between the Earth and the Sun and the real emission spectra is taken into account. At the altitude of the satellites, the the energy radiated by the Earth in the infra red region around 10 μm far exceeds the energy from the Sun.

The transmittance spectrum in figure 1.4 shows that the atmosphere is very irreg-

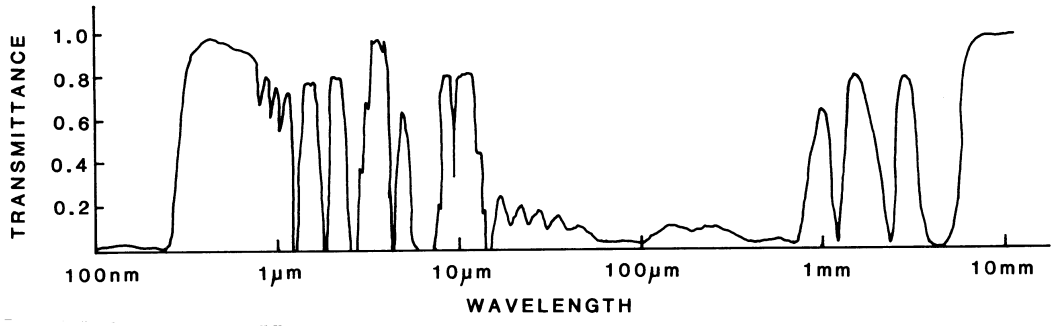

Figure 1.4: Transmittance of the atmopshere for different wavelengths. After Robinson (1985)

ular in what wavelengths that are allowed to pass through. The wavelength bands with high transmittance are called windows and besides the obvious window in the visible, it is clear from the figure that there is a window in the thermal infra red region around 10 μm with high atmospheric transmittance.

In the thermal infrared channels we thus have a maximum in emission from the sea surface and a weak attenuation by the atmosphere. Furthermore, as the emission from the Earth is dependant on the temperature as indicated by equation 1.1, SST can be estimated from infra red satellite observations.

An atmospheric window is also seen in figure 1.4 for AVHRR channel 3, indicating that it can also be used for SST retrievals. However, contamination from reflected sun light during daytime and noise from the instrument has limited the use of this channel to estimate sea surface temperature.

Even though channel 4 and 5 are in a transmittance window, atmospheric effects in cloud free conditions attenuate the radiation from the sea surface and will thus

results in a to low SST if not corrected for. The strongest absorption is from water vapor, but aerosols and gases like CO_2, CH_4 and NO_2 also effect the radiation from the surface. The atmospheric absorption is different for channel 4 and 5 and this is exploited to estimate the atmospheric effects. Several algorithms have been used for the AVHRR observations as described by Barton (1995) but they all originate from the basic equation of

$$SST = aT_4 + \gamma(T_4 - T_5) + c \tag{1.2}$$

Where a and c are constants and γ is the differential absorption. T_i is brightness temperature in channel i and it is defined as the temperature that is required for a perfect emitter to produce the measured radiance according to equation 1.1. The latest algorithm is the nonlinear SST algorithm (NLSST) where γ is assumed to depend upon a first-guess SST value (Kilpatrick et al., 2001). An additional term has been introduced to account for the increased atmospheric path length for larger zenith angles. The nonlinear SST algorithm is then

$$SST = a + bT_4 + c(T_4 - T_5)SST_{guess} + d(T_4 - T_5)(sec(\theta) - 1) \tag{1.3}$$

Where θ is the incidence angle of the upcoming radiation, a,b,c and d are constants to be determined by least squares regression and SST_{guess} is derived from the weekly SST from National Centers for Environmental Prediction (NCEP) (Reynolds and Smith, 1994).

The drawback of estimating SST with a passive infrared sensor is the limitation in the method when clouds are present. No observations can be obtained in cloudy conditions and as shown in section 1.3.2 this gives a drastic reduction in the data return in regions with persistent cloud cover.

It is important to be aware that the SST observations derived from equation 1.3 are from the very top of the sea surface. The surface layer that emits the infrared radiation is only about 0.1mm thick (Robinson, 1985) hence the temperature observed by satellite is called the skin SST in contrast to the bulk SST measured by e.g. buoys or ships. The skin and the bulk temperatures can differ up to ± 1°C due to processes such as a diurnal thermocline in the upper meters and evaporative cooling of the upper millimeters of the surface (Stewart, 1985, Schluessel et al., 1990).

1.3.2 Data coverage and cloud limitations

All the polar orbiting NOAA satellites mentioned above have a sun synchronous orbit configuration and thus pass a given latitude at the same local time. The altitude of the satellite is 850 km with an orbit inclination of 98.9° and orbital period of 102 minutes. This configuration produces daytime observations from the ascending pass and nighttime observations from the descending pass with a daily global coverage.

As mentioned above, there are data gaps in the daily global coverage due to clouds and the impact of this effect varies of course for different regions. The region around Iceland is for instance well known to have a persistent cloud cover. The data loss due to clouds were investigated for the different regions where the AVHRR data are used in the following chapters. The results are seen in figure 1.5 where the left figure shows the mean SST for the North Atlantic. Outlined in the figure are also two regions along

the AX03 XBT line in blue and magenta (see chapter 3), a region in the Denmark Strait in red (chapter 2) and the region around the ocean weather ship M in green (chapter 3). Figure 1.5b shows the mean SST for these boxes in the upper plot and

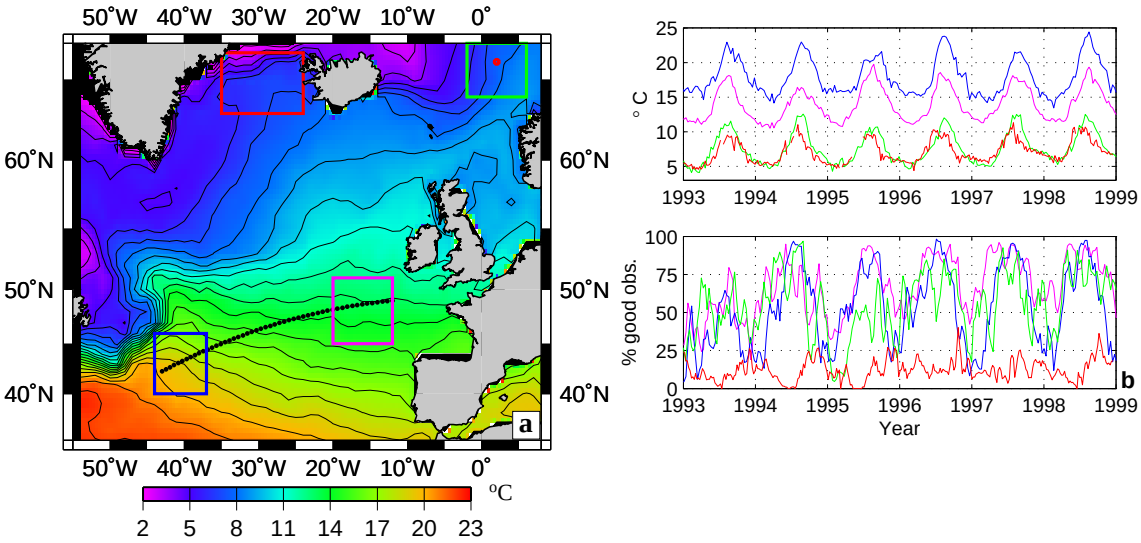

Figure 1.5: a: Mean sea surface temperature from AVHRR satellites. Contour interval is 1°C. The colored boxes correspond to regions where SST data will be used in the following chapters. b: mean SST and percentage of 9x9 km pixels with at least one cloud free observation during 10 days. The colors of the curves corresponds to the color of the boxes in the left figure. The thick black line indicate the position of the AX03 XBT observations and the ocean weather ship M is marked with the red dot. Data from both sites are used in chapter 2.

the lower curves display the percentage of the 9x9 km pixels in the boxes where at least one cloud free observation is available during 10 days.

The three regions in blue, magenta and green, display a data return above 50 percent with most observations in the eastern end of AX03 (magenta) with a mean about 65%. Large annual variations in the amount of clouds are seen in these regions where maximum cloudiness is found during winter and minimum during summer.

The Denmark Strait region shown in red is distinctly different from the other regions. A persistent cloud cover result in a very low data return with maximum 40 percent with no pronounced annual variation. The mean percentage of good pixels during the repeat period of 10 days is as low as 12 and this includes occasions where not a single pixel in the red region has been determined to be cloud free of the 20 images available during the 10 day period. The example in figure 1.5 thus demonstrates the inherent limitation by clouds in the passive infrared AVHRR observations which may reduce the number of observations substantially in cloudy regions.

1.3.3 Data processing and accuracy

The AVHRR Pathfinder observations were obtained from the Physical Oceanography Distributed Active Archive Center home page[1] and consist of daily observations from January 1992 to November 20, 1999. The Pathfinder product used here is the "Best SST" daytime observations in a nominal 9 km resolution (see Vazquez et al., 1998). The data are provided in an equal angle grid with a resolution of 4096/360 degrees which means that the actual pixel size varies with latitude from 9×9 km at equator to e.g. 6×9 km at 48° latitude.

The SST time series from 1992-1999 contains data from version 4.0 and 4.1 that both uses the NLSST algorithm in equation 1.3. The coefficients a,b,c and d were determined from a least squares regression to in situ observations over a 5 months period. The regression was performed separately for a dry atmosphere where $T_4 - T_5 \leq 0.7$°C and a wet atmosphere with $T_4 - T_5 > 0.7$°C.

The two versions differ mainly in the quality flags that are assigned to every pixel during the data processing and cloud identification. Declouding was performed by running a series of tests to assess the likelihood that a given pixel is contaminated by clouds. The criteria in the cloud masking algorithm include uniformity tests and brightness temperature tests of T_4 and T_5 (Kilpatrick et al., 2001, Vazquez et al., 1998). The "Best SST" data set that was used here implies that all observations with suspicious cloud pixels have been discarded to avoid possible contamination from clouds.

Accuracy

As it is bulk temperature that is useful for this study, the difference between the skin and the bulk temperature can be considered as additional noise in the data. On a cruise in the eastern North Atlantic, Schluessel et al. (1990) found differences between skin and bulk SST from -1°C to 1°C with a mean difference of 0.3°C during day and 0.11 during night. They also found the skin and bulk temperatures to be highly correlated on large spatial scales O(100 km). This is an interesting finding to this study because chapter 3 uses changes in SST over large areas and the skin-bulk difference is therefore likely to be reduced.

The errors associated with the Pathfinder atmospheric attenuation and correction have been investigated by Kearns et al. (2000) who compared skin SST observed with the Marine Atmosphere Emitted Radiance Interferometer (MAERI) mounted on a ship, with AVHRR observations. Five cruises from 1996 and 1998 resulted in a mean discrepancy between the two SST estimates of 0.14°C and a standard deviation of 0.36°C.

In an thorough analysis of the performance of the Pathfinder data, Kilpatrick et al. (2001) compared the satellite SST observations with several thousands in situ observations from moored and drifting buoys. The differences between the in situ SST and PFSST is 0.02°C in the mean with a standard deviation of 0.53°C. The discrepancies in the SST estimates are summarized in table 1.6 for the different error contributions described above. Note that the Pathfinder vs. Bulk include errors in the atmospheric correction (Pathfinder vs. Skin SST), the Bulk vs. Skin difference and errors in the buoy measurements. However, it may be of some importance that the

[1] http://podaac.jpl.nasa.gov/

Error Contribution	Mean μ (°C)	Std. dev. σ (°C)	Reference
Bulk vs. Skin SST	0.1-0.2	0.11-0.3	Schluessel et al. (1990)
Pathfinder vs. Skin SST	0.14	0.36	Kearns et al. (2000)
Pathfinder vs. Bulk SST	0.02	0.53	Kilpatrick et al. (2001)

Table 1.6: Overview of the uncertainties involved in the satellite observations of SST

observations from the buoys are not completely independent of the Pathfinder SST because the same observations have been used in the regression analysis to determine the coefficients in equation 1.3. Also, the difference between the skin temperatures measured by the AVHRR instrument and the bulk SST is probably reduced, as the satellite data are regressed onto the bulk SSTs from the buoys.

The good performance of the Pathfinder SST is also seen in several climatologies constructed from the SST observations (Casey and Cornillon, 1999, Armstrong and Cuervo, 2001). In a comparison with in situ data, the Pathfinder derived 9 km climatologies had smaller residuals than other global SST products such as the NCEP climatology (Reynolds and Smith, 1994).

An alternative to the AVHRR observations exists in the Along Track Scanning Radiometer which is mounted on the ERS 1 and 2 satellites. The instrument makes infrared observations as with AVHRR, but the scanning mechanism gives two observations of every pixel with different atmospheric paths and thus allow for a more accurate SST estimation (Barton et al., 1995, Barton, 1998). However, the swath with of the instrument is only 500 km (compared to 2700 for AVHRR) hence the coverage is substantially reduced compared to the AVHRR. In the light of the importance of the cloud cover, as seen in figure 1.5 I therefore decided to use the AVHRR pathfinder for this study. The higher accuracy for a single ATSR observation will thus be matched by the accuracy that can be obtained when averaging over several AVHRR observations.

In summary, the Pathfinder data set appears to be one of the most accurate and consistent global SST data set that are available at present with an accuracy of ± 0.5°C for a single observation in the 9 km resolution data. Averaging over N observations will reduce the random noise by a factor of $\sqrt{N}$ and as the skin-bulk SST variations are correlated over $\sim$100 km the uncertainty from this effect will probably be very low when averaging over 500×500 km as in chapter 3. The substantial reduction in data return in some regions with persistent cloud cover is the main argument for not using the ATSR data with higher accuracy because the lower spatial sampling.

As mentioned above, the SST data used in chapter 3 are averages over 500 km latitude by 500 km longitude regions. To reduce the spatial contamination that can be induced by a combination of a temperature gradients and a cloud cover, the 9 km data were first averaged in 1° bins and subsequently averaged over the large regions.

2

Overflows In the North Atlantic

2.1 Introduction

2.1.1 Global thermohaline circulation

The global thermohaline circulation is related to deep convection at a few sites around the world. In the present climate, deep convection associated with the thermohaline circulation is found only in the Labrador Sea, the Arctic Mediterranean and in the Weddell Sea in the Southern Ocean. The high latitude location of the convection sites means that the deep water flowing equatorward is replaced by warm and salty surface water from lower latitudes, giving rise to a poleward heat transport. This meridional overturning circulation is responsible for about half of the poleward heat transport in the ocean-atmosphere system (Macdonald and Wunsch, 1996).

The impact of the thermohaline circulation is easily seen from global mean sea surface temperature (SST) observations in figure 2.1. The SST north of 50°N in the

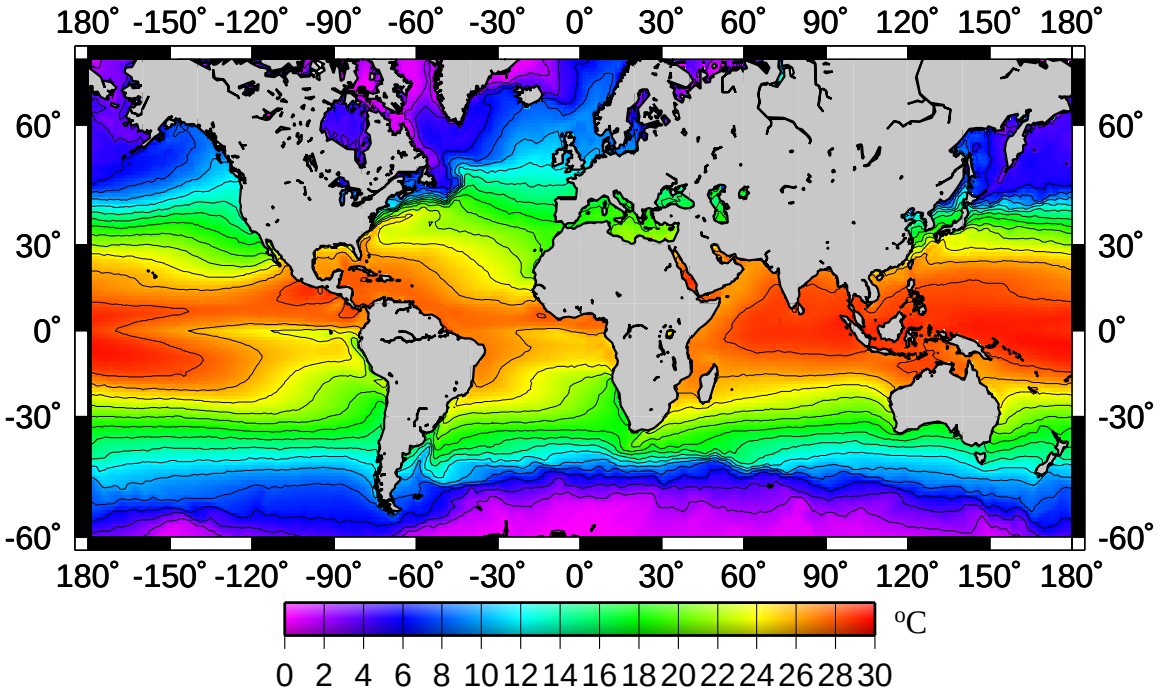

Figure 2.1: Global mean sea surface temperature observed by the AVHRR satellites. Increments between contours are 2 degrees Celcius

North Atlantic is significantly higher than at the same latitude in the Northern Pacific

and is has been estimated that Europe is 5-8 degrees warmer due to the thermohaline driven heat contribution (Broecker, 1991, Ganopolski and Rahmstorf, 2001). Observations since decades in the North Atlantic have shown significant inter annual and inter decadal changes in the amount of deep water produced in the Labrador Sea and in the Arctic Mediterranean (Dickson et al., 1996). The changes have been in phase but with opposite sign, a seesaw behavior with maximum convection in Labrador Sea at present. In this study I will focus on the deep water formed in the Nordic Seas and in particular the use of satellite altimetry data to study the deep water when it overflows the Greenland-Scotland ridge. After an introduction to the overflows in section 2.1.2, the theory about what controls the transport through the straits will be described in section 2.3. In situ observations and the variability from the sills are presented in section 2.4 together with a description of 3 mechanisms that are able to generate the fluctuations in section 2.5. The sea surface variability related to the fluctuations is estimated in section 2.6. Results from satellite observations in section 2.7 demonstrate that the mixing associated with the overflows can be detected as enhanced sea surface height (SSH) variability in the Denmark Strait and the Faroe Bank channel. Finally, section 2.8 discuss the limitation of this method in regions with large variations in the mean sea surface. Most of the results described in this chapter are also presented in Høyer and Quadfasel (2001) and Høyer et al. (2002) and some of the figures have been taken from these publications.

2.1.2 Overflows in the North Atlantic

As indicated in figure 2.2, the overflow of dense bottom water from the Nordic seas into the North Atlantic occurs mainly through the two deepest gaps in the Greenland-Scotland ridge: The Denmark Strait (sill depth 620 meters) and the Faroe Bank Channel (sill depth 850 meters). The mean transports of the overflows are ~ 2.9 Sv through the Denmark Strait and ~ 1.5 Sv through the Faroe Bank Channel (Hansen et al., 2001, Dickson and Brown, 1994). Overflows between Iceland and the Faroe Islands and across the Wywille–Thomson ridge have a more intermittent character and add up to a transport around 1 Sv (Hansen and Østerhus, 2000).

Downstream of the sills, the dense plumes are primarily in geostrophic balance and follow the bathymetry on the right as indicated in figure 2.2. However, the plumes have a downslope velocity component associated with bottom friction and entrainment of ambient water. An alternative pathway was found during the Overflow 73 project where one survey from the Faroe Bank Channel found fairly undiluted overflow water north of Lousy Bank corresponding to a southwesterly path of the overflow (Hansen and Østerhus, 1998). This is the only study that reports such an ageostrophic path and it is probably not important considering mean transports. This is corroborated by results from the Poseidon 264 cruise in 2000, where a section off Lousy Bank only showed signs of overflow water in very diluted form.

2.2 Characteristics of overflow water

The dense water that overflows the two sills originates in the Nordic Seas and the Arctic ocean. The formation of the deep and intermediate waters is fairly complex (see e.g. Marshall and Schott, 1999) and will not be described in detail here. Suffice

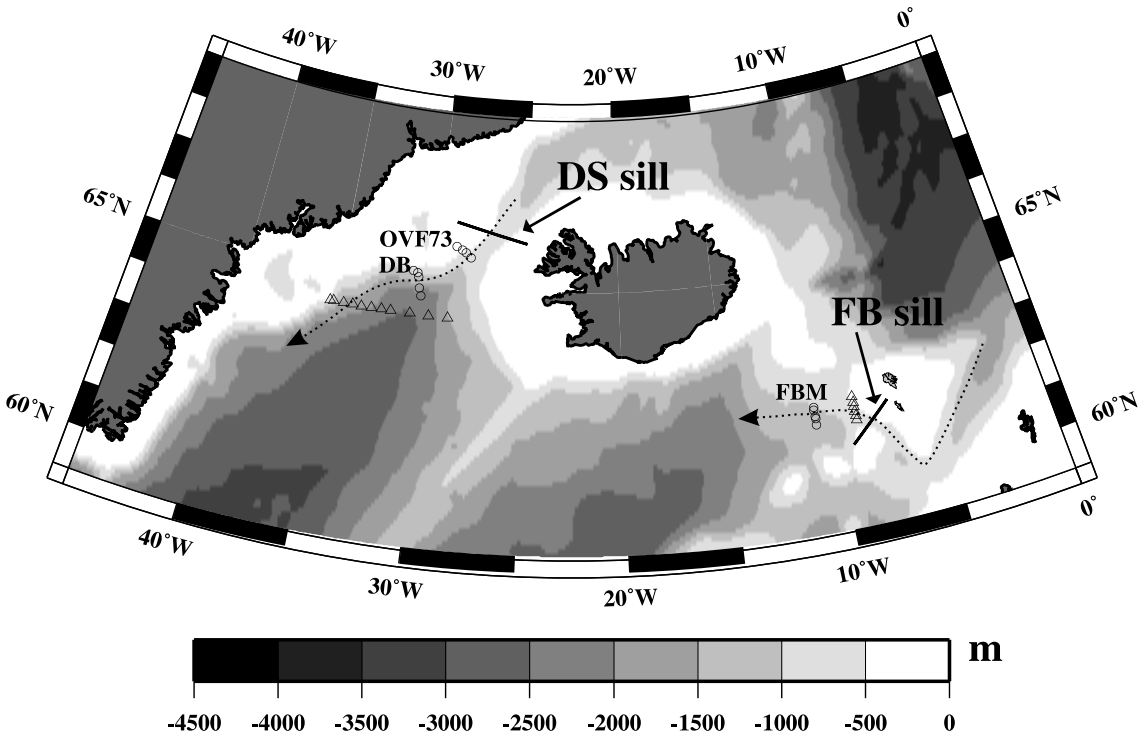

Figure 2.2: Bathymetry of the North Atlantic in gray shading. The thin dotted lines indicate the mean path of the overflow water through the Denmark Strait and the Faroe Bank Channel. The Dohrn Bank (DB), the Overflow 73 (OVF73) and the Faroe Bank (FBM) mooring arrays are indicated with circles. Triangles mark the position of the conductivity-temperature-depth (CTD) casts downstream of Denmark Strait sill (from Veins data) and of the Faroe Bank Channel sill (Poseidon 264 data). The sills are indicated with bold solid lines.

to say that three processes are recognized as important to the formation of deep and intermediate waters: Open ocean convection in the Nordic seas, shelf convection in the Arctic Ocean and frontal processes within the Norwegian Sea (Blindheim and Ålandsvik, 1995). The literature traditionally divides the important source waters for the two overflows into two water masses: The Norwegian Sea Deep Water (NSDW; T$\leq$ -0.5°C, S=34.91) and Norwegian Sea Arctic Intermediate Water (NSAIW; $-0.5 \leq T \leq 0.5$°C, $34.87 \leq S \leq 34.91$).

The water that overflows the FBC sill is composed primarily of NSDW but CTD profiles from the sill show a salinity minima in the water around 0°C due to a contribution from NSAIW (Turrell et al., 1999). At the sill the core of the FBC overflow water has temperatures below -0.5°C and salinities around 34.91. Observations from three ADCPs located at the sill have shown that maximum speeds exceed 1 m/s. The cross-channel temperature and along-channel velocity isolines slope down from the Faroe Plateau with a mean plume thickness of about 200 meters in the center of the channel. After the sill, entrainment of Atlantic water makes it difficult to distinguish between overflow water across Wywille-Thompson ridge and FBC. Often the term Iceland-Scotland Overflow Water (ISOW) is used for waters with $\sigma_\theta \geq 27.8$.

The source of the water that overflows the DS is more complicated than the FBC

overflow (Rudels et al., 1999). Dickson and Brown (1994) estimate that out of the 3 Sv of dense water exported out of the Nordic seas, the Arctic Intermediate Water makes 2.5 Sv of the overflow and that Upper Polar Deep Water from the Canadian Basin makes 0.5 Sv. The densest water masses of the Arctic Mediterranean and the Nordic Seas do not overflow the DS because the sill is too shallow. Instead, the deep water has been observed to be turned at the Jan Mayen Fracture Zone (Rudels and Quadfasel, 1991) or at the entrance to the DS in the Iceland Sea (Buch et al., 1992) and flows into the Norwegian Sea where it may contribute to formation of NSDW. The composition and sources of the DS overflow are not resolved and significant discrepancies can be found in the literature. Jonsson (1999) argue for the idea that the Iceland Sea is the main contributor to the DS overflow, whereas (Mauritzen, 1996) estimates that over 80% of the total overflow comes from modified Atlantic water from the Arctic Ocean that has been joined in the Fram strait by recirculating Atlantic Water in the Nordic Seas. The discrepancies in the descriptions may be due to the inter annual and decadal changes in the sources and compositions of the outflows (Bacon, 1998, Dickson et al., 1996).

The core of the DS overflow has temperatures of 0°C and salinities of 34.90 (Swift, 1984). In the vicinity of the sill, the overflow is 150 meters thick with southward current speeds of 35 cm/s (Girton and Sanford, 2001). As with the FBC overflow, the DS overflow plume is shifted to the right when looking in the direction of the flow. The characteristics of the cores of overflow waters close to the sills are summarized in table 2.1. Site descriptors such as sill depth and width are also included.

	Faroe Bank Channel	Denmark Strait
Temperature(°C)	-0.5	0
Salinity	34.91	34.90
Speed cm/s	≥ 100	35
Thickness(m)	200	150
Transport (Sv)	1.5	2.9
Width (km)	15	50
Sill depths (m)	850	620

Table 2.1: Characteristics of the DS and FBC overflows in the sill regions

2.3 Topographic control

The description of a fluid that is influenced by rotation and flowing from an upstream basin through a constriction is called rotating hydraulics. The pioneering work was done by Stern (1972) and Whitehead et al. (1974) and their work serves as the basis for this section together with more recent reviews (Pratt and Lundberg, 1991, Whitehead, 1998).

The nonlinear nature of the problem makes it a difficult task to find analytical solutions except for the simplest cases. The theory presented here is one such example where we consider two deep basins connected with a channel in a rotating coordinate system. The channel is oriented in the y direction with the right wall located at

$x = 0$ looking from the upstream basin. The other wall is at $x = -b$ and the vertical z-axis is assumed parallel to the rotation axis. The basins contain two homogeneous inviscid layers with different density where the top layer is stagnant. Overflow occurs from one basin through the channel at a constant rate since the interface height above the channel floor is held constant in the upstream basin. If we assume hydrostatic balance and steady state the starting point is the horizontal momentum equation.

$$\vec{u} \cdot \nabla \vec{u} + f\hat{k} \times \vec{u} + \frac{1}{\rho}\nabla_h p = 0 \tag{2.1}$$

where $\vec{u}$ is the horizontal velocity vector, ρ is the density, f the Coriolis parameter, ∇_h the horizontal gradient, $\hat{k}$ a unit vector in the z direction and p the pressure deviation from the hydrostatic value at rest. The equation can be transformed into the well known Bernoulli equation describing the energy of the system

$$\frac{1}{2}|\vec{u}|^2 + \frac{p}{\rho} = G(\psi) \tag{2.2}$$

Where the function G has to be determined for the problem and depends only upon the streamfunction ψ which can be defined as

$$\nabla \times \psi\hat{k} = h\vec{u}. \tag{2.3}$$

Where h is the height of the interface above the bottom. Another relation can be derived by taking the curl of equation 2.1 and integrating over the height of the layer to get the conservation of potential vorticity. Assuming steady state we get

$$\frac{1}{h}\left(\frac{\partial v}{\partial x} - \frac{\partial u}{\partial y} + f\right) = F(\psi) \tag{2.4}$$

where F is a function of ψ that has to be determined. When we use the two assumptions that the x-scales are much smaller than the y scales and that v is much larger than u we can derive the geostrophic equation, the Bernoulli equation and the Potential Vorticity equations for this problem from equation 2.1, 2.2 and 2.4:

$$-fv + \frac{1}{\rho}\left(\frac{\partial p}{\partial x}\right) = 0 \tag{2.5}$$

$$\frac{v^2}{2} + \frac{p}{\rho} = G(\psi) \tag{2.6}$$

$$\frac{1}{h}\left(\frac{\partial v}{\partial x} + f\right) = F(\psi) \tag{2.7}$$

The three equations in 4.1, 2.6 and 2.7 constitute the basis for the derivation of the rotating hydraulics below. The three equations are not fully independent because it can be shown that G and F are related through

$$\frac{\partial G}{\partial \psi} = F. \tag{2.8}$$

The determination of F and G is simplified a great deal if we assume that the velocity of the fluid in the upstream basin is very small (~ 0). With h_u being the upstream interface height above the bottom of the channel we get an expression for the Bernoulli potential G from equation 2.6

$$G = \frac{\rho_2 - \rho_1}{\rho_2} h_u = g' h_u \tag{2.9}$$

where g' is the reduced gravity. G is now independent of ψ resulting in zero potential vorticity as F is also zero. Away from equator the Coriolis parameter is never zero hence, the first assumption about zero upstream velocity implies that the depth of the upstream basin is infinitely deep according to equation 2.7. Integration of 2.7 with $F = 0$ gives an estimate of the velocity in the channel as a function of x

$$v = -fx + v_0 \tag{2.10}$$

Where the integration constant v_0 is the velocity at $x = 0$.

We now want an expression for the interface height h above the channel floor and combine equation 4.1 together with the pressure $p = gh(\rho_2 - \rho_1)$ to get

$$fv = g' \frac{\partial h}{\partial x}. \tag{2.11}$$

Inserting the value for v from equation 2.10 into equation 2.11 and integration on both sides gives the wanted relationship

$$h = \frac{f^2 x^2}{2g'} + \frac{f v_0 x}{g'} + h_o \tag{2.12}$$

Where h_0 is another integration constant that describes the interface height at $x = 0$.

We now have the expressions for the velocity and the interface height in the channel that are necessary to calculate the transport. The Bernoulli relation applied to the streamline at x=0,

$$\frac{v_0^2}{2} + g' h_0 = g' h_u \tag{2.13}$$

is used to relate the two undetermined integration constants h_0 and v_0 and the number of unknowns are thus reduced to one. Several critical conditions can be imposed in order to determine the integration constant. The most common, which is also used here, is the assumption that h_0 is chosen so that the transport Q is maximized for a given h_u. In nonrotating hydraulics this condition is equivalent to setting the Froude number $Fr = v/\sqrt{g'h}$ at the sill to one.

In order to calculate the transport through the channel, the flux in the lower layer is integrated from the interface intersection with the bottom or the side wall ($-x_b$) to the other side of the channel ($x = 0$). Equation 2.11 is used to rearrange before integration

$$Q = \int_{-x_b}^{0} vh dx = \int_{-x_b}^{0} \frac{g' h}{f} \frac{\partial h}{\partial x} dx = \frac{g'}{2f} \left(h_0^2 - h^2(-x_b) \right) \tag{2.14}$$

The general expression above is now treated for two cases, one where the interface intersects the bottom and one where it intersects the other wall in the channel. In the first case it is evident that $h(-x_b) = 0$ and the assumption of maximum transport result in $h_0 = h_u$. With these parameters the maximum transport through the channel is

$$Q_{max} = \frac{g' h_u^2}{2f} \tag{2.15}$$

The point where the interface intersects the channel floor is found by combining equation 2.10 and 2.12 and using that $v_0 = 0$,

$$x_b = \sqrt{\frac{2g' h_u}{f^2}} \tag{2.16}$$

It is thus clear that equation 2.15 applies when the condition $(2g' h_u / f^2)^{1/2} \leq b$ is satisfied. Note that the length scale that separates the two regimes resembles the baroclinic Rossby radius except for a factor $\sqrt{2}$. When the width of the channel is smaller than this, the interface intersects the other side of the channel (i.e. $-x_b = -b$) and the condition $h(-x_b) = 0$ can not be used. The expression of the height of the interface from equation 2.12 is inserted in equation 2.14 with $-x_b = -b$ to obtain

$$Q = \frac{1}{2g'} \left(\frac{fb^2}{2} + v_0 b \right) \left(2h_u g' - v_0^2 - \frac{f^2 b^2}{2} - f b v_0 \right) \tag{2.17}$$

Where the Bernoulli relation from equation 2.13 have been used to eliminate h_0. The maximum transport through the channel is found by calculating $\partial Q / \partial v_0 = 0$ and inserting the maximum v_0 in equation 2.17

$$Q_{max} = \left(\frac{2}{3} \right)^{3/3} b g^{1/2} \left(h_u - \frac{f^2 b^2}{8g'} \right)^{3/2} \tag{2.18}$$

Equation 2.15 and 2.18 describe the transport of water through a channel depending on the width of the channel compared to the baroclinic Rossby radius multiplied by $\sqrt{2}$. In both cases it is straightforward to predict the transports through straits from only four parameters: The Coriolis parameter, the width of the strait, the density difference and the upstream height of the interface above the sill.

Laboratory studies confirm the predictions by equations 2.15 and 2.18 (Whitehead et al., 1974) and ratios of predicted to observed transports of 1-2.7 has been obtained for several oceanic overflows, including the DS and FBC (Whitehead, 1998). The estimates can be improved by including more realistic bottom topography (Borenäs and Lundberg, 1988, Killworth, 1995, 1992). In the FBC, Borenäs and Lundberg (1988) fitted a parabolic curve to the topography and obtained transports of 1.5 and 2.5 Sv through the FBC compared to the 3.0 Sv that Whitehead (1998) obtained from equation 2.15 assuming a rectangular bottom. The high predictions by the simple theory compared to the observed transports can probably be attributed to the assumption of a rectangular sill bottom together with the neglection of friction and mixing. The theory has been extended to include constant upstream potential

vorticity (Gill, 1977, Pratt and Armi, 1987, Whitehead, 1989, Borenäs and Pratt, 1994) which is equivalent to an finite depth basin with a nonzero current. However, Whitehead (1989) suggest that this effect may play a minor role as their transports with constant PV are within 22% of the zero PV transports.

A 3-dimensional model set up for the Denmark Strait also showed a close relationship between the height of the interface at the sill and the transports, corroborating that the topographic control described above is the primary mechanism (Käse and Oschlies, 2000).

It is thus clear that the theory of rotating hydraulics perform well in describing the control of transports through straits.

2.4 In situ variability

In situ observations of temperature, salinity and currents have revealed that the conditions upstream of the two sills are fairly stable on subannual time scales (Smith, 1976). This is in contrast to the conditions downstream of the sills, where large fluctuations with time scales of a few days have been observed in both the DS and the FBC overflow (Worthington, 1969, Mann, 1969, Saunders, 1990). Figure 2.3 shows

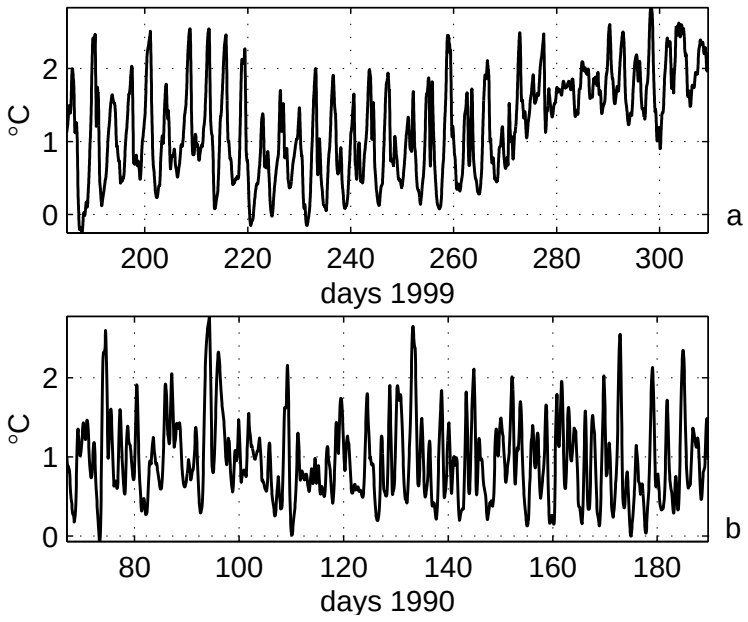

Figure 2.3: Near bottom temperature observations from the core of the overflows ~150 km downstream of the two sills. a: mooring from the Faroe Bank Channel, b: mooring from the Denmark Strait.

near bottom temperature records from the core of the two overflows about 150 km downstream of the two sills. It is evident that large fluctuations of several degrees are observed with periods of a few days in the two overflows. The energy spectrum reveals that the characteristic periods are $\sim$ 2.8 days for the Denmark Strait overflow and $\sim$ 3.5 days for the Faroe Bank Channel overflow. The absence of annual variations in the overflows is supported by observational records extending more than a year

(Saunders, 1994, Dickson and Brown, 1994). However, recent results from five years of mooring data at the sill in the FBC show some annual and inter annual variability (Hansen et al., 2001).

Near bottom temperature and currents from mooring arrays 150 km downstream (see figure 2.2 for location) are shown as time latitude plots in figure 2.4. The temperature observations are interpolated between the moorings and shown as colored contours and the arrows represent velocity anomalies. The mean velocity is removed from each mooring time series and the length and orientation of the arrows correspond to the speed and the direction, respectively (up is northward flow). The longest arrows represent a current anomaly of $\sim$ 30 cm/s for the Faroe Bank Channel and

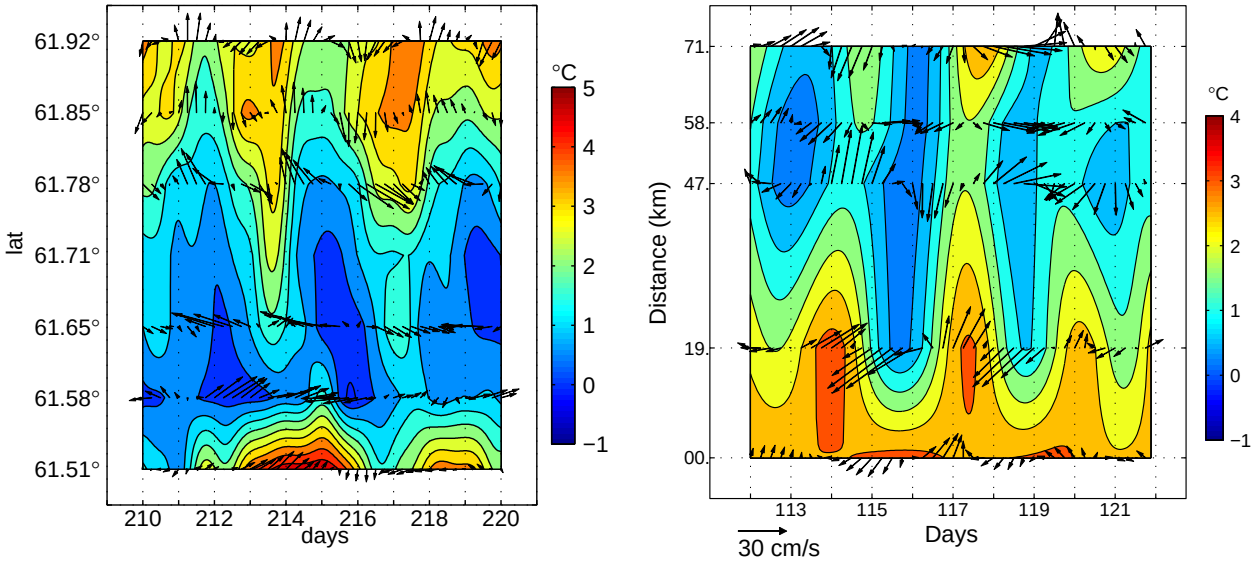

Figure 2.4: Temperature (colored contours) and current anomalies (arrows) from the Dohrn Bank mooring array downstream of the DS (left) and the Faroe Bank mooring array downstream of the FBC (right). Both arrays are located ~150 km downstream of the sill FBC. Temperature contour interval is 0.5°C. See figure 2.2 for the position of the moorings.

$\sim$ 40 cm/s for the Denmark Strait. The two 10-day periods that are shown in the figure are representative of the conditions in the more than 100 days of observations from the two mooring arrays. The arrays intersect the mean path of the overflow plume, and the fluctuations in temperature are seen to be correlated in time across the overflow. Thus, the variations in the overflow are not due to a meandering in the plume of cold water but arise from pulses of cold water. Furthermore, it is evident that variations in temperature are correlated with current fluctuations in the FBC and DS. In particular it is very clear at the northern flank in the FBC that minima or maxima in temperature are associated with reversals of the currents.

The correlation between current and temperature fluctuations agrees very well with the presence of meso scale eddies that have been observed downstream of sill in

the Denmark Strait. Results from drifters, Infrared satellite observations and high density ship surveys agree that a train of eddies is located along the East Greenland slope, extending as far south as $62.50°N$ (Krauss, 1996, Bruce, 1995, Krauss and Käse, 1998). The typical eddies have a core diameter of 20-40 km and propagate along the East Greenland slope with ~ 30 cm/s.

The existence and generation of meso scale eddies have also been reproduced in 3–dimensional models of the DS overflow (Jiang and Garwood, 1996, Jungclaus et al., 2001, Krauss and Käse, 1998, Käse and Oschlies, 2000, Shi et al., 2001) indicating that the overflow plume is accelerated by anticyclonic eddies on the shallow side of the plume and cyclonic eddies on the deeper down slope side.

The variations in near bottom temperature associated with the eddies correspond to a variability in the thickness of the overflow plume. Conductivity-temperature-depth (CTD) profiles were occupied on a cruise with R/V Poseidon fall 2000 a north-south section 30 kilometers downstream of the sill (see figure 2.2 for mooring position). The section was repeated 5 times in 6 days and from the potential temperature displayed in figure 2.5 it is evident that the amount of cold overflow water changes rapidly. The variability is largest in the southern part of the section and when overflow water is defined as water colder than 3°C, an increase in the thickness of 230 meter is observed. The last 4 sections in the figure are only 12 hours apart, and even on these short time scales the variations can clearly be seen.

Downstream of the Denmark Strait, mooring data from the Overflow 73 array (CM3) and the Dorn Bank array (9003) (see figure 2.2) were used to estimate the mean thickness and variations of the overflow plume. Both moorings were equipped with 3 temperature sensors in the vertical. According to Smith (1976) the overflow water is distinguished in the Overflow 73 array by temperatures less than 2°C. When this criterion is applied to the temperature profiles obtained by linear interpolating between the three sensors, the thickness is estimated to vary from 110 meters (Deepest mooring) to 260 meters (shallowest mooring) with a mean of 220 meters. The estimated thickness of the plume was insensitive to other interpolation methods such as cubic splines. A temperature criterion of 3°C was used at the Dohrn Bank array as it is located further downstream where entrainment of warm water has increased the temperature of the overflow. The mean thickness was estimated to fluctuate between 18 (deepest mooring) and 550 meters with a mean of 320 meters. These estimates derived from mooring data at three depths are obviously more uncertain due to the limitation in the vertical resolution. Knockdown of the mooring can also introduce a false variability in the thickness of the overflow plume. Data from a pressure sensor mounted on the shallowest Dohrn Bank sensor indicate that the mean knockdown was around 40 meters with a standard deviation in the pressure of 31 meters.

2.5 Mechanisms generating the fluctuations

From observational and model studies several mechanisms have been proposed for the generation of meso scale variability in the overflow plume. A review of all the different ideas will not be given here but 3 mechanisms are presented.

Based upon the observations from the Overflow 1973 project in the Denmark Strait, Smith (1976) formulated a quasi geostrophic model with two uniform layers

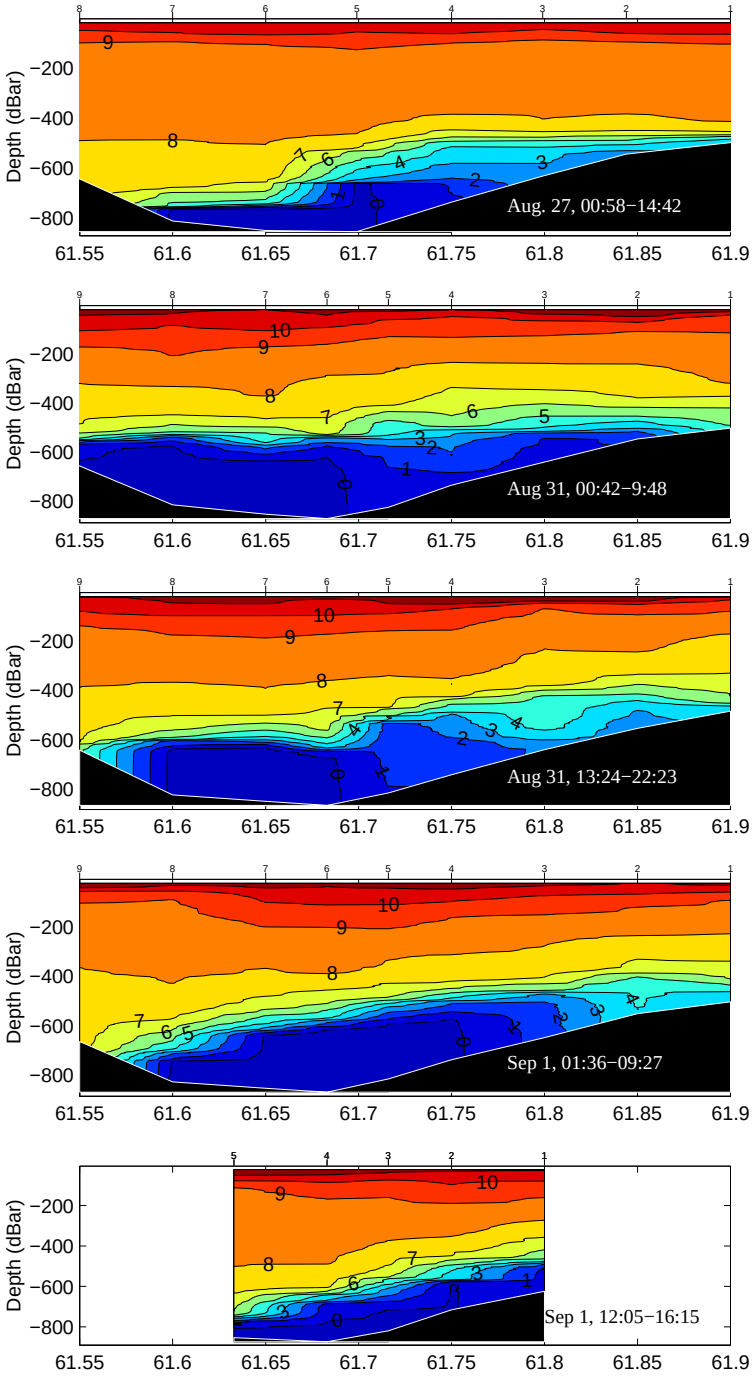

Figure 2.5: Potential temperature for the 5 repeats of the section taken ∼30 km downstream of the Faroe Bank Channel (see figure 2.2). Contour interval is 1°C and the top numbers indicate the CTD casts.

on a sloping bottom. Baroclinic instabilities on the interface between the two layer lead to perturbations that amplifies and propagate downstream. With a bottom velocity of 60 cm/s the regime of maximum amplifications of the perturbations is at

a wavelength about 80 km with a period of 2.1 days. Some of the assumptions about linearity and small perturbations may be violated but the simple two layer model accomplish to generate variability of the order a few days with steady upstream conditions.

From one of the first 3 dimensional models of overflows on a sloping bottom (Jiang and Garwood, 1996) it was evident that cyclonic eddies were generated as the plume descended the slope. Jiang and Garwood (1996) suggested that the generating mechanism was vortex stretching and conservation of vorticity as water column was stretched. The equation for relative vorticity $\zeta = \frac{\partial v}{\partial y} - \frac{\partial u}{\partial x}$ when molecular and turbulent dissipation are neglected can be described as (Krauss and Käse, 1998)

$$\frac{\partial \zeta}{\partial t} = -\vec{v} \cdot \nabla \zeta + (f + \zeta)\frac{\partial w}{\partial z} - \beta v \tag{2.19}$$

where f is the Coriolis parameter and $\beta = \frac{\partial f}{\partial y}$ is the latitudinal change in the Coriolis parameter. Krauss and Käse (1998) investigate the different terms in equation 2.19 and find in agreement with the results from Jiang and Garwood (1996) that the dominating terms on the right hand side are the first two terms. These terms describe that vorticity changes due to advection of vorticity or from stretching of the water column:

$$\frac{\partial \zeta}{\partial t} = -\vec{v} \cdot \nabla \zeta + (f + \zeta)\frac{\partial w}{\partial z} \tag{2.20}$$

From this equation it is clear that on the downslope side of the overflow plume the descend and vertical stretching of the plume will produce cyclonic vorticity ($\partial w/\partial z > 0$) manifested by cyclonic eddies. Equation 2.20 allow that anticyclonic eddies $\zeta < 0$ can exist in the upslope side of the plume due to vortex tube squeezing. Anticyclonic eddies was not seen by Jiang and Garwood (1996) but recent model results and observations have confirmed the presence of anticyclonic eddies in the Denmark Strait (Krauss and Käse, 1998, Jungclaus et al., 2001). Cyclonic vorticity is advected on the downslope side and anticyclonic on the up slope side of the plume when eddies have been generated. These type of eddies resemble topographic Rossby waves but Krauss and Käse (1998) note that the vertical velocity structure of the eddies is different from the structure predicted from linear wave theory and neither the long wave nor the shortwave approximation applies to these eddies. They conclude that the strong nonlinearity associated with the eddies and the interaction with the current field does not allow the formulation of simple linear theory for the eddies.

The generating of eddies by a lens of dense of water on a sloping bottom is corroborated by laboratory experiments conducted by Whitehead et al. (1990). They demonstrate that generation of eddies is a general feature of a dense current on a rotating sloping bottom.

A third generating mechanism apply to the Faroe Bank channel overflow and suggest that variability in the upstream conditions are important. The interface between Atlantic water and Norwegian Sea Deep Water in the Faroe-Shetland channel is observed to fluctuate with time scales of a few days. Section 2.3 demonstrated that the overflow is subject to hydraulic control and the transport across the sill depends on the interface height as described by equation 2.17 and 2.15. In channel pulsations

in the interface will therefore result in fluctuations in the amount of deep water that overflows the sill. As the overflow descends after the sill the pulses are enhanced due to the other mechanisms which generates the eddies with time scales of a few days. The origin of these in channel fluctuations has not been explained but is currently under investigation (*Quadfasel, personal communication*). This mechanism does not apply to the Denmark Strait due to different bottom topography upstream of the sill but figure 2.3 allow contributions from different generating mechanisms because the variations in the Faroe Bank Channel are much more regular than the Denmark Strait observations.

The schematic in figure 2.6 summarizes the results from observations and models:

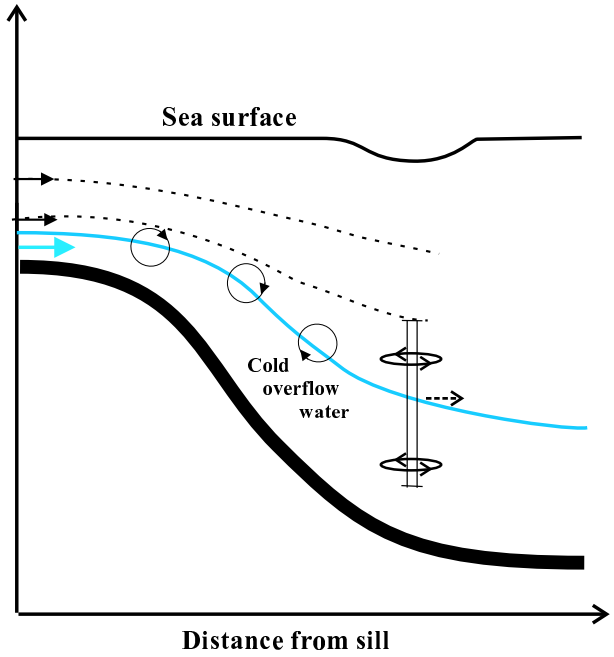

Figure 2.6: A schematic of the overflow process: Descending cold water mixes with the ambient water and eddies are generated. The fluctuations give rise to a sea surface signal.

As the overflow of dense and cold bottom water mixes and entrains ambient water, the plume descends toward greater depths and eddies are generated on both sides of the overflow plume. Cyclonic eddies (as shown in figure 2.6) on the downslope side of the overflow plume predominates but anticyclonic eddies are also present.

2.6 Estimated sea surface height variability

The density of sea water $\rho(S,T,P)$ is dependent on temperature and salinity and pressure. Changes in one of these parameters will result in density changes which again will give rise to and expansion or contraction of the water column. To calculate how much a water column between two depths is expanding or contracting, the

equation for the steric height is used (see e.g. Tomczak and Godfrey (1994))

$$h(z_1, z_2) = \int_{z_1}^{z_2} \delta(S, T, P)\rho_0 dz \tag{2.21}$$

Where ρ_0 is a reference density and the specific volume anomaly, δ is defined as:

$$\delta(S, T, P) = \frac{1}{\rho(S, T, P)} - \frac{1}{\rho(35, 0, P)} \tag{2.22}$$

In the calculation of steric heights from CTD profiles the pressure is used instead of the depths. When pressure is used in decibars, the difference between a meter and a decibar is negligible and the equation now becomes:

$$h(p_1, p_2) = \int_{p_1}^{p_2} \delta(S, T, P)\rho_0 dp \tag{2.23}$$

CTD profiles were used downstream of the Faroe Bank Channel sill to calculate estimated steric sea surface height variability from equation 2.23. The steric height from the maximum pressure (about 10 meters above bottom) to 50 meters below the surface was calculated from the 5 repeats (42 profiles) of the hydrographic section 30 km downstream of the sill (see figure 2.2). To avoid a steric height variability introduced from the mean conditions of the overflow plume, estimates are only compared from profiles within 5 km. The steric height anomalies for the different repeats are shown in figure 2.7 plotted against latitude. In agreement with figure 2.5, the variability

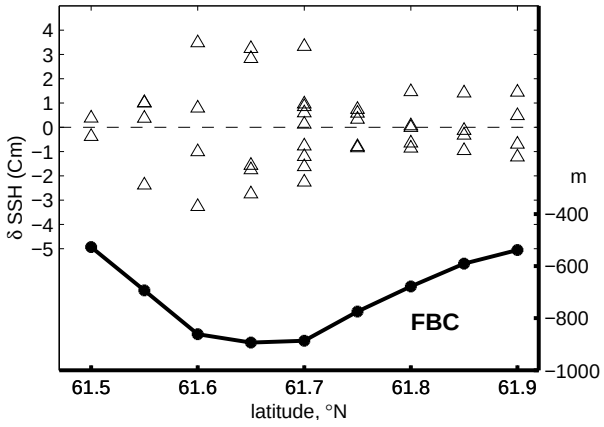

Figure 2.7: Steric height anomalies (triangles, left axis) calculated from CTD profiles along the section 30 km downstream of the Faroe Bank Channel sill (see Figure 2.2). The depth in meters is shown in solid (right axis). The anomalies are relative to mean values calculated at the positions marked with dots. All CTD casts are taken within 6 days in August 1999.

is largest in the southern section of the channel with a difference in steric height of more than 6 cm between the first and the second occupation. The variability of the steric height anomalies exceeds 2.9 cm in the southern part of the section.

About 140 km from the sill, 30 CTD profiles from 4 years of cruises with R/V Valdivia were available. The casts were located within 10.7-11.1°W along the Faroe

Bank mooring array in figure 2.2 and the steric heights calculated over the deepest 500 meters in order to avoid steric effects from seasonal or inter annual changes in the upper layers. Again the variability was calculated for latitude boxes resulting in steric height variability of up to 2.0 cm. Interannual variability in the bottom 500 meters can not be ruled out but the effect is probably small as the steric height differences within the year were as large as the interannual differences.

The steric height variability in the Denmark Strait was calculated on the basis of the mooring observations described in section 2.4. The plume was assumed to be homogenous with temperature as observed by the bottom sensor. With a plume thickness of 220 m at the Overflow 73 array and 320 m at the Dohrn Bank array (see section 2.4) the steric height variability was 2.1 cm for the Overflow 73 array and 1.9 cm for the Dohrn Bank array.

90 CTD profiles were taken along a section about 400 km away from the Denmark Strait sill (2.2) during the Variability of Exchanges In the Northern Seas (VEINS) project. The section intersects the overflow plume at a depth of about 1800 meters on the East Greenland slope. Stations along the section were occupied between 6 and 13 times from 1997-2000. The steric heights were again calculated over the deepest 500 meters in every profile to exclude seasonal and interannual variability in the upper layers. The mean steric height was removed in every station and the anomalies are shown in figure 2.8. It is seen from the figure that the location of the overflow plume

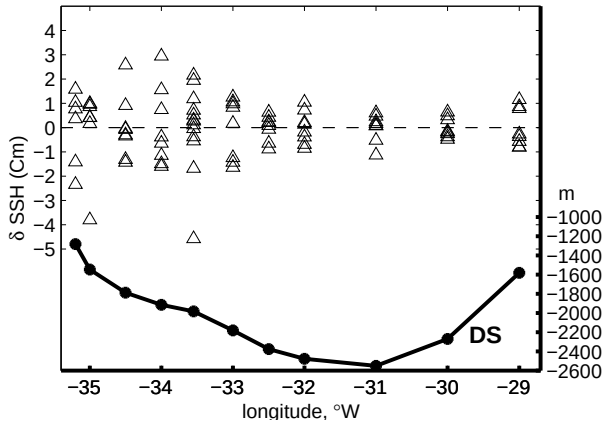

Figure 2.8: Steric height anomalies (triangles, left axis) calculated from 90 CTD profiles along the section is about 400 km downstream of the Denmark Strait sill (see Figure 2.2). The depth in meters is shown in solid (right axis). The anomalies are relative to mean values calculated at the positions marked with dots. The profiles are taken from 1997 to 2000 and the steric heights are calculated over the deepest 500 meters.

coincides with the largest variability in the steric heights anomalies with a maximum variability of 1.7 cm at 33.5°W. This variability is probably related to fluctuations with periods of days because variability with periods longer than 10 days is small for the Denmark Strait overflow (Saunders, 2001).

The results from the steric height estimates are summarized in table 2.2. The variability of the overflows is also evident from observations of near bottom current

Sill		Distance from sill (km)	σ_{ssh} (cm)
DS	Record length (days)		
	37	55	2.1
	120	160	1.9
	Number of profiles		
	90	400	1.7
FBC			
	42	30	2.9
	30	140	2.0

Table 2.2: Maximum estimates of steric height standard deviation, based on Overflow 73, Dohrn Bank 1990 mooring data and CTD profiles from the VEINS project from the Denmark Strait, and CTD profiles from the Faroe Bank Channel. The positions of the observations are indicated in figure 2.2.

velocities downstream of the sills. A typical measure of the current variability is the eddy kinetic energy, E', calculated as

$$E' = \frac{1}{2}\langle u'^2 + v'^2 \rangle \tag{2.24}$$

Where u' and v' are the northward and eastward velocity anomalies, respectively and $\langle \cdot \rangle$ denotes the time mean. The results from moorings located in the path of the DS and FBC overflows are summarized in table 2.3. Besides the significant SSH

Sill	Number of moorings	Distance from sill (km)	E' cm^2/s^2
DS	4	55	309-635
	5	160	59-263
	22	480	24-131
FBC	1	0	70
	2	30	213,375
	6	140	77-210

Table 2.3: Eddy kinetic energy downstream of the two sills from near bottom moorings. The data used in the Denmark Strait (DS) are from the Overflow 1973 mooring array, the Dohrn Bank 1990 and from the Angmassalik array (see Smith (1976), Dickson and Brown (1994)). Current meter data from the Faroe Bank Channel (FBC) are from B. Hansen, personal communication, 2000.

variability due to overflow processes, tables 2.2 and 2.3 also reveal the downstream behavior of variability in the overflow plumes. The maximum variability is found immediately downstream of the sills in both E' and steric height about 30-55 km from the sills and decreases further downstream.

2.7 Satellite observations

Previous studies of overflows employing remote sensing techniques used passive infrared imagery (Bruce, 1995). Infrared satellites suffer from very poor data return in the Denmark Strait due to persistent cloud cover and rely on a gradient in the sea surface temperature (which is not present in the Faroe Bank Channel) to detect the eddies. When a front in SST present, there will always be an ambiguity whether the eddies are generated by frontal instabilities or by overflow processes.

In this section I will use the altimetry versions 5.1 for T/P and 5 for ERS 1+2 where all the standard corrections (including the tides and inverse barometer effect) have been applied as described in chapter 1. As the observations from ERS and T/P are active microwave radar measurements they are not limited by cloud cover or dependant upon SST signal associated with the overflows. However, the repeat periods of 10 days for the T/P satellite and 35 days for the ERS satellites gives Nyquist periods of 20 and 70 days. Thus, the altimeter data can not be used to resolve fluctuations with time scales of a few days. If the satellite time series are long enough the variability from the fluctuations will still be contained in the observations due to aliasing and they can be detected by calculating second order statistics such as standard deviation and eddy kinetic energy. Two signals with the same spectral characteristics as the two temperature signals in figure 2.3 were constructed to test the convergence of the standard deviation as a function of subsampled observations. With a 9.916 days subsampling of the time series the variability converged towards 90 % of the true values in only 20 samples. The convergence did not change if the subsampled times were shifted with 1 day and we would thus expect the variability observed by the satellites to represent the true variability if the measurements were perfect.

Flagged data were discarded as described in chapter 1 and a 3-standard deviation filter was applied to the remaining observations to remove outliers. The results in the following sections are based upon minimum 100 observations for T/P and 30 for ERS.

The assumption about geostrophy is valid on spatial scales larger than the baroclinic Rossby radius defined as:

$$r = \frac{c}{f} \tag{2.25}$$

where c is the baroclinic gravity wave phase speed. The Rossby radius decreases polewards due to the latitude dependance of the Coriolis parameter and is generally less than 10 km in the North Atlantic above 60 degrees (Chelton et al., 1998). Meso scale eddies with spatial scales of the order 20-40 km are Thus in geostrophic balance and the slope of the sea surface can be related to the surface velocities through the relations:

$$\frac{\partial \eta}{\partial x} = \; fv \tag{2.26}$$

$$\frac{\partial \eta}{\partial y} = -fu \tag{2.27}$$

Where η is the observed sea surface height. Uncertainties in the geoid limit the estimation of absolute velocities to very large spatial scales on the order of the gyre

circulation (Ganachaud et al., 1997). However, the variability in the geostrophic currents can be estimated from the alongtrack slopes observed by the altimetry satellites. A measure of the variability is the time mean eddy kinetic energy estimated from

$$K_e = \frac{g^2}{f^2}\langle(\frac{\partial\eta}{\partial s})^2\rangle \tag{2.28}$$

where η is SSH anomaly, s the along track distance, $\langle\cdot\rangle$ denotes time average, g is gravity. Equation 2.28 gives twice the eddy kinetic energy from the cross track geostrophic surface velocity which corresponds to the total eddy kinetic energy under the assumption of local isotropy. This assumption is in good agreement with the DB1990, O73 and the Angmassalik current meter moorings downstream of the DS and from FBC moorings. In all current records the deep current variability in the mean direction of the flow was the same size as the variability of the currents perpendicular to the mean flow.

2.7.1 *Faroe Bank Channel*

The small spacing between the ERS groundtracks in the Faroe Bank region makes it possible to perform an interpolation of the calculated standard deviations. An objective gridding routine with a second order covariance model and correlation scales of ~150 km was used to grid the standard deviation and K_e results shown below. The noise level applied in the gridding algorithm was based upon the errors on the results which will be estimated below.

From figure 2.9 it is evident that elevated SSH variability is seen downstream of

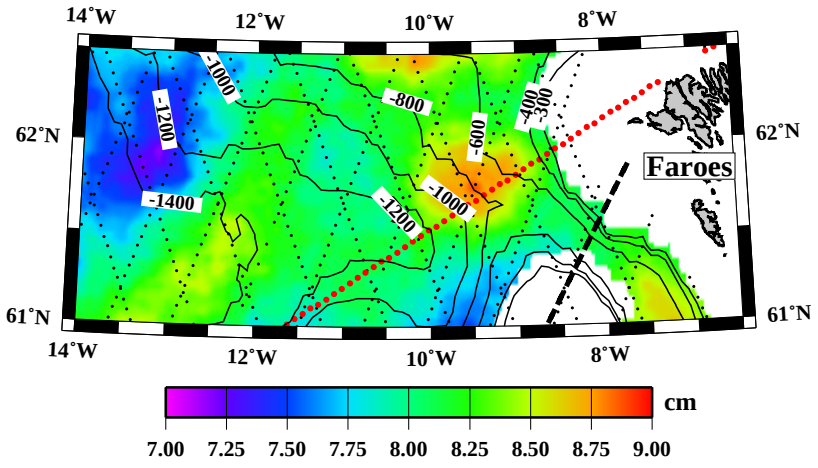

Figure 2.9: Gridded standard deviation of ERS 1+2 SSH observations (colors) and bathymetry (contours) in the Faroe Bank Channel region. The positions of the ERS ground tracks are overlaid in black and only observations obtained at depths >300 m have been used. The red dots indicate the T/P ground track used in figures 2.10 and 2.12. The black dashed line indicates the sill.

the sill in the Faroe Bank Channel as expected from section 2.6. The peak of ~9

cm which is 1-2 cm above the background level of 7-8 cm, is located about 60 km from the sill where the plume descends towards greater depths. The overflow plume is detected in several ground tracks and the spatial scales are $\sim$ 50 km in latitude and longitude. The steric height variability of up to 2 cm $\sim$140 km from the sill (table 2.2) is not seen in figure 2.9 which is probably due to the higher uncertainty in the standard deviation estimates.

Due to the large spacing between the TOPEX/POSEIDON ground tracks at this latitude it is not feasible to interpolate the results to detect the mean path of the overflow. Instead, the results shown in figure 2.10 are from the individual satellite ground tracks located about 60 km downstream of the sill (see figure 2.9), it is clear

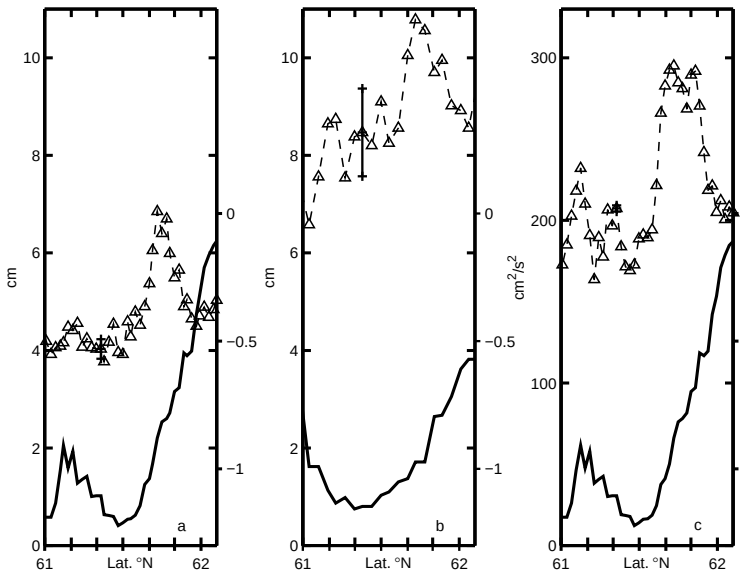

Figure 2.10: Along track results from the Faroe Bank Channel. The solid lines denotes the water depth in km (left axis). a: Dashed lines with triangles are standard deviation of ssh from TOPEX/POSEIDON track 32. b: As a but for the ERS satellite track 405 c: Eddy Kinetic Energy from the T/P tracks 32. see figure 2.9 for location of the tracks.

from figure 2.10 a and b that the two independent estimates are consistent because both satellites detect an increase in sea level variability of $\sim$ 3 cm on the slope where the ground tracks crosses the overflow plume. The ground tracks are almost perpendicular to the mean path of the overflow and can be used to estimate a spatial scale of the eddies under the assumption that the eddies propagate along the plume. Enhanced SSH std deviation is detected in 7 observations along the T/P ground track and 5 observations along the ERS track which gives a spatial scale of about 30-50 km for the variability. The higher background noise level for the ERS observations are due to larger errors in single observations.

Errorbars are calculated under the assumption that we only consider changes from the along track sea level and not absolute values. Orbit errors and errors in the corrections applied to the data have a much larger spatial scales than the signal from the overflow plume (see e.g. *JGR 101, Special issue*,[1994]). Thus, the measurement

errors are assumed to be the instrumental noise of ∼2 cm for the T/P and ∼ 5 cm for the ERS satellite. With the criteria of minimum 30 observations for ERS and 100 observations for T/P, the presicions of the along track standard deviations are 0.9 cm for ERS and 0.2 cm for the T/P results. Similarly, the presicion of the eddy kinetic energies were $20cm^2/s^2$. The peak in variability is more distinct in the T/P data than in the ERS data due to a combination of more observations and higher accuracy of the individual observations.

Figure 2.10c displays elevated time mean eddy kinetic energy from the T/P data derived by using equation 2.28. The increase in K_e of $\sim 75cm^2/s^2$ is calculated without any alongtrack smoothing prior to the gradient calculation. Smoothing over 21 km reduced the K_e with about $100cm^2/s^2$ for all the points along the track but the peak was still highly significant. The TOPEX/POSEIDON groundtracks to the west of the one in figure 2.9 is located about 200 km further downstream. No significant enhancement of the surface variability was seen in this track, indicating the rapid decrease in the variability downstream of the sill. Eddy kinetic energy calculated from ERS observations shows higher values associated with the overflow but the increase is not significantly above the background noise level and the results are therefore not included here.

2.7.2 Denmark Strait

The high latitude of the Denmark Strait close to the turning point of the T/P satellite makes the data favorable for this study. The ground tracks are closely spaced and oriented almost east-west, perpendicular to the mean path of the overflow along the East Greenland slope. Thus it is possible to grid the results from the T/P data. The same gridding routine and parameters was used as described in section 2.7.1. The sill is located around 66.2°N and from figure 2.11 a and b it is evident that enhanced SSH variability and K_e is seen immediately downstream of the sill in the T/P data. The ERS satellite also detect the SSH variability but as for the FBC too few observations were available to give a reliable K_e result. Both satellites reveal that elevated SSH variability is centered on the western side of the Denmark Strait with a peak of about 13-14 cm compared to background levels of 6-10 cm, highest for the ERS 1+2 satellites. Elevated SSH variability is extending about 150 km downstream from the sill. The time mean eddy kinetic energy calculated from the T/P observations also depict the path of the overflow. The picture is more clear than for SSH variability and details like a shift of the plume from the center of the strait to the left hand side is clearly seen. Peak values are $K_e \sim 550cm^2/s^2$ with background noise levels around 200 cm^2/s^2

2.7.3 Seasonal variability

With the increasing observation period of the satellite missions we can reliably calculate the standard deviation of SSH for the 4 seasons for the two overflows throughout the period of observations. Only results from the T/P satellite will be shown here because seasonal estimates are based upon a quarter of the observations used in the previous sections. Thus, with standard deviations of SSH based upon 10-20 observations (compared to ∼60 for all the record) the uncertainty in the ERS results is too

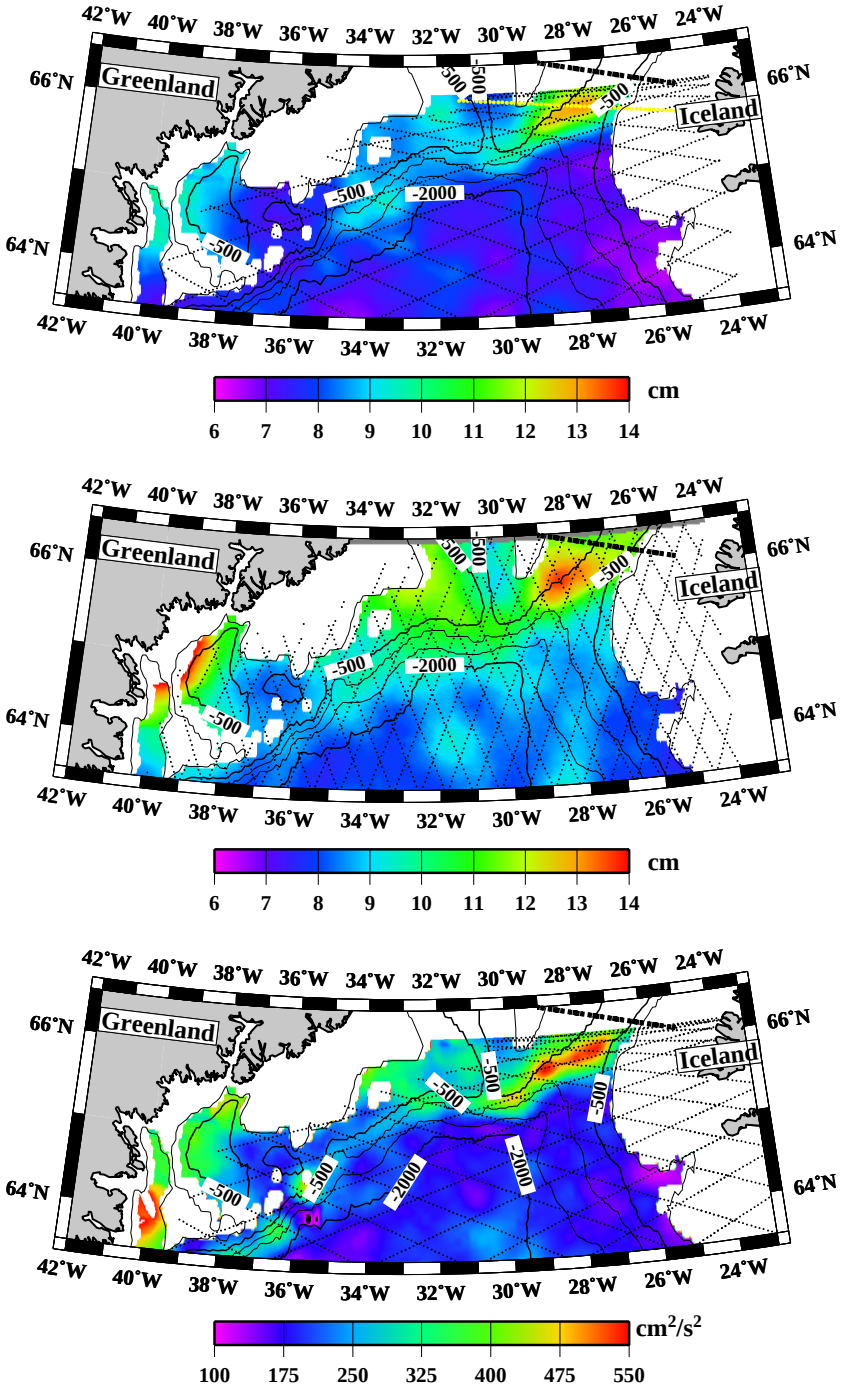

Figure 2.11: Gridded results from the Denmark Strait. Upper: SSH Standard deviation from T/P, middle: SSH standard deviation from ERS 1+2, lower: Eddy Kinetic Energy from T/P. Bottom depth is contoured and satellite ground tracks are overlaid in black. The yellow ground track in the top figure is used for the results in figure 2.12. Shallow observations ($\leq$ 300 m) have been excluded.

high compared to the signal we want to detect. The seasonal behavior of the variability was examined in two T/P ground tracks, located in the regions with enhanced variability through all the years and perpendicular to the mean paths of the overflow (see figure 2.9 for FBC and figure 2.11 for DS). Bad observations were discarded in the same way as in the previous section, but the criteria of minimum observations was lowered to 25 observations per season. Figure 2.12 shows the results from the DS and FBC regions, where the variability is calculated for the individual seasons throughout all years of the record. The peaks in SSH variability are clearly seen

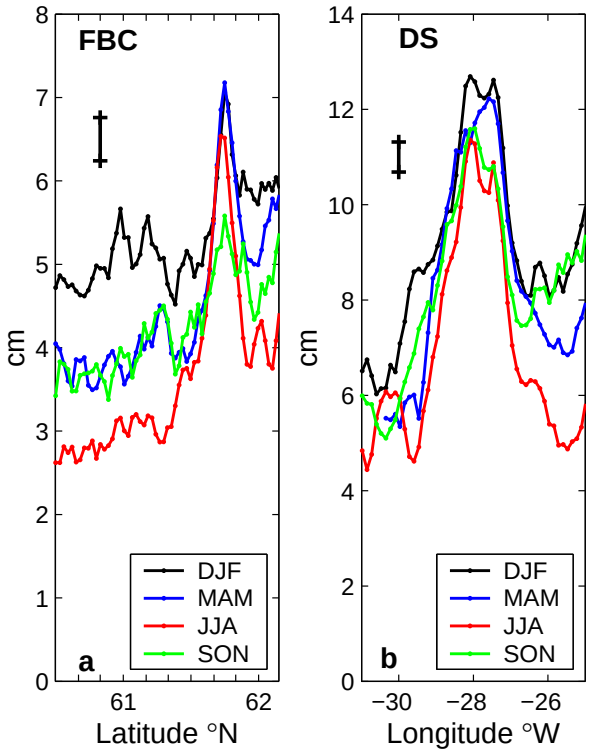

Figure 2.12: SSH variability calculated from the T/P for the different seasons: December-January-February (DJF), March-April-May (MAM), June-July-August (JJA) and September-October-November (SON). a) Along a ground track 30 km from the Faroe Bank Channel sill (red dots in figure 2.9). b) Results from a ground track in the Denmark Strait (Yellow line in figure 2.11).

during all seasons for both overflows, even though the uncertainty in the estimates are higher due to the reduced number of observations. In the Denmark Strait, the number of available observations decreases towards the East Greenland coast due to ice contamination. However, the standard deviations for the peak values in figure 2.12a are all based upon a minimum of 40 observations and the precision is therefore 0.3 cm. The ice free conditions in the Faroe Bank channel region result in better data return and the standard deviations in figure 2.12b are based upon minimum 60 observations (precision of 0.26 cm). Error bars are added according to these results.

The background noise level is defined to be the SSH variability in the ground

tracks which is found outside the peaks associated with the overflows (e.g. south of 61.5°N in FBC and east of 27°W in the DS). It is seen from Figure 2.12 that the seasonal differences are primarily due to variations in this background noise level with a maximum during winter (Dec-Jan-Feb) and minimum during summer (June-July-Aug). The other satellite observations away from the overflow plume display a similar seasonal cycle in the variability, which is probably due to variations in the amount of eddies generated by the wind. White and Heywood (1995) related seasonal varying eddy kinetic energy of the subpolar North Atlantic to changes in wind forcing and Stammer and Wunsch (1999) found a significant correlation between eddy kinetic energy and wind forcing in 10 by 10 degree areas in the eastern North Atlantic. In addition, Stammer et al. (2001) used an eddy resolving model of the North Atlantic to show the importance of high-frequency wind forcing in generating eddy kinetic energy. Figure 2.12b reveals the differences between the DS and the FBC: The DS increase above the background level is relatively constant for all the seasons with an increase of 4-5 cm but the FBC overflow shows some seasonal variation. The late fall (Sep-Oct-Nov) increase is of 1-2 cm above the background level of ∼4 cm. This is significantly lower than the summer (June-July-Aug) values, where the background level of ∼3 cm and the peak variability of ∼6.5 cm represent an enhancement of up to 3.5 cm due to fluctuations in the overflow plume. It is not yet clear if these variations are related to changes in the transport or the density of the overflow, but sensitivity studies with a high resolution model of the overflows could give insight into this matter.

2.7.4 Discussion

The overflow regions downstream of the DS and the FBC exhibit a significant increase in sea surface height variability and eddy kinetic energy close to the two sills. The regions coincide with the mean locations of the plumes in areas where the overflows experience large bottom slopes and where high meso scale eddy activity is observed. The spatial scales with enhanced variability detected by altimeters are about 30-50 km which is in good agreement with the scale of the overflow plume and the generated eddies.

The magnitude of the observed SSH variability is consistent with estimates derived from in situ measurements. Discrepancies can arise from the fact that the steric estimates are derived only from density changes in the water column. Barotropic eddies are not connected with density changes and will only be included in the satellite observed ssh. Thus, we would expect the observed SSH variability to be higher than the variability derived from in situ observations.

The effects from changes in salinity are not included in the estimated variability for the Denmark strait but the salinity differences between Atlantic water and overflow water are relatively small $\leq$ 0.1 (Price and Baringer, 1994, Ross, 1983) and will not effect the steric height variability from temperature variations. Furthermore, as the altimeter observations are averages over a footprint of $\sim$ 5 km in diameter the observed variability will be reduced compared to the in situ.

Contributions to the sea surface height variability from e.g.: Insufficient subtraction of the tides, errors in the inverse barometer effects and high frequency barotropic

motion (Stammer et al., 2000) can induce a variability of several centimeters. However, in all the cases the spatial scale of the variability is much larger than the spatial scale of the signal observed here and the contributions will only affect the background noise level.

A SSH variability signal similar to the observed in figure 2.10 may be induced in the altimeter observations through a combination of a gradient in the geoid and misplacement of the ground tracks (see e.g. Tapley and Kim, 2001). The estimation and minimization of this effect was dealt with in three ways: i) To avoid large deviation from the ground tracks only observations within 1 km from the nominal ground tracks were used without any significant alteration of the result. ii) To minimize the induced variability, observations located off the nominal ground track were interpolated to the ground track position by the Pathfinder team by using the GSFCMSS mean sea surface. iii) The mean sea surface slopes from the KMS2000 mean sea surface (which is similar to the GSFCMSS) were examined in the DS and FBC region to assess the magnitude and structure of the variability that could be induced if the mean sea surface was. The magnitudes of the sea surface slopes are shown in figure 2.13 for the Faroe Bank Channel and the Denmark Strait. The figure shows that the

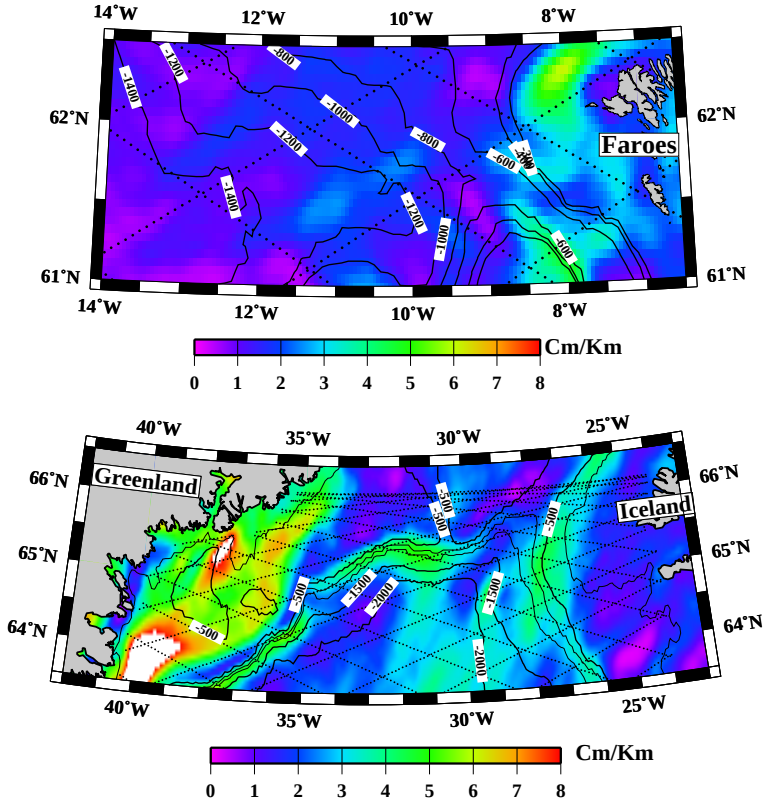

Figure 2.13: Magnitude of the mean sea surface slopes from the KMS2000 mean sea surface. Top: The Faroe Bank Channel region and bottom: The Denmark Strait area. T/P satelite tracks are overlaid in black and bathymetry is contoured.

the FBC region is associated with small gradients in the sea surface. This is seen

in particular in the region of enhanced SSH variability associated with the overflow plume (figure 2.9) with slopes < 2 cm/km.

The gradients in the mean sea surface in the DS are larger than for the FBC with up to 10 cm/km off the Greenland coast. A concern to this study is the band of enhanced gradients (4-5 cm/km) along the east Greenland slope that coincides with the mean path of the overflow. However, this region is located downstream of the region with maximum SSH variability (figure 2.11). The slopes immediately downstream of the sill are very low and can not contribute to the observed maximum in SSH variability. Uncertainty in the mean sea surface may induce a signal further downstream from the sill but the VEINS results in figure 2.8 suggest that the deep overflow accounts for the enhanced SSH variability at 64.3°N. Based upon these results we can therefore conclude that the off-track geoid induced SSH variability is unlikely to have any significant effect on the results from both the DS and the FBC.

In the FBC, the absence of strong fronts or swift currents not associated with the overflow thus makes the interpretation easy. Investigation of AVHRR SST data revealed that there is no significant SST signal in this area. The Iceland-Faroes front is situated north of the Iceland-Scotland ridge and do not influence the area around the Faroe Bank. To conclude: There exist no other known processes that can produce a peak in variability with the same spatial scales and located at the plume over a period of 8 years.

In the Denmark Strait the altimetry results are also in agreement with the in situ data, with largest variability very close to the sill that decreases further downstream. The shift from the center of the strait to the left side as seen in the K_e is consistent with recent model results (Käse and Oschlies, 2000). However, the DS is not a simple two layer exchange flow as the FBC and several oceanic processes can contribute to SSH variability. The East Greenland current is a very cold and relatively fresh southwestward surface current along East Greenland. Changes in the current or eddies generated by instabilities along the East Greenland Front can give rise to a SSH signal. Frontal processes will always be accompanied by a SST signal hence AVHRR SST observations can be used to locate the regions with statistically maximum variability. The 9 km Pathfinder SST data as described in chapter 1 revealed a maximum DS variability that was located downstream from the peak in SSH variability in figure 2.11. Persistent cloud cover in combination with an annual cycle in SST could induce a false variability signal in some regions. To reduce this contamination, the annual and semiannual harmonic were fitted and removed in every pixel but it did not change much in the structure of the variability. Thus it appears that frontal processes can contribute to the background noise level along the East Greenland slope but they are not able to induce the downstream behavior in the variability as observed by the satellites.

The Northward flowing Irminger Current west of Iceland is another possible source of SSH signals but the current is mainly confined to the shelf on water depths shallower than 200 meters. The possible SSH contamination is therefore avoided by masking out all results from water depths shallower than 300 meters as in figure 2.11.

The presence of sea ice that are being exported southward through the Denmark Strait is another process which was absent in the region around the Faroes. Sea ice

will tend to dramatically increase the return signal of the radar pulse. Contaminated observations like that will be flagged and the larger percentage of flagged data in the Denmark indicate that observations influenced by sea ice are indeed discarded in the processing.

2.8 The off-track geoid correction in other overflows

Overflows of dense bottom water from one basin to another is an important mechanism in the distribution of water masses throughout the world oceans (Whitehead, 1998). Several important overflows such as the Charlie-Gibbs Fracture Zone, the Mediterranean outflow and the Romanche Fracture Zone overflow exhibit fluctuations and mixing similar to the FBC and the DS (Saunders, 1994, Iorga and Lozier, 1999b, Polzin et al., 1996). With the above findings it is therefore interesting to extend the analysis to some of these regions where dense water flows over a sill and descends. However, several of the overflows with significant transport occur in fracture zones and other areas with large variations in the mean sea surface due to a gravity signal. The sea surface slopes in these regions can exceed 10 cm/km which introduces a significant SSH signal if the satellite ground tracks are displaced off the track. As mentioned above, the Pathfinder team try to correct for this error by interpolating the observations to the exact repeat track with the use of a mean sea surface. Thus, if the mean sea surface was correct the Pathfinder processing would remove the signals introduced by this effect. However, a closer examination of the results reveal that inaccuracies in the mean sea surface might limit the investigations of some overflows. Two examples will be given here, from the Chalie-Gibbs Fracture Zone overflow and the Mediterranean outflow.

Mediterranean outflow

As the Mediterranean Sea is an evaporative basin, the outflow through the Strait of Gibraltar into the North Atlantic is dense and salty compared to the surrounding waters. The outflow follows the continental slope off the Iberian Peninsula but is strongly modified by mixing and entrainment in the Gulf of Cadiz where the plume descends the continental slope (Wesson and Gregg, 1994, Price et al., 1993, Killworth, 2001). With salinity anomalies higher than 2 and plume speeds exceeding 1 m/s over a 100 meter thick bottom layer, it is clear that variability due to mixing and meandering of the overflow plume would give rise to a SSH signal on the order of centimeters. Such a signal is large enough to be observed by the altimetry satellite as enhanced variability similar to the DS and FBC overflow. In addition, Westward propagating eddies (MEDDIES) with 40-100 km diameters and up to 30 cm/s currents are generated by the overflow off Portugal (Richardson et al., 2000). The associated temperature anomalies of up to 4°C and salinity anomalies over 1 in a 500-1000 m thick layer are also related to surface height variations on the order of centimeters (Stammer et al., 1991).

The results looks promising at a first glance with the same data processing as above including the cross track geoid correction and only using observations within 1 km from the exact repeat track. The variability along the track is shown in figure 2.14a and show significant enhancement of SSH variability in the vicinity of the overflow plume an in the region of large mixing. However, the KMS2000 mean sea surface

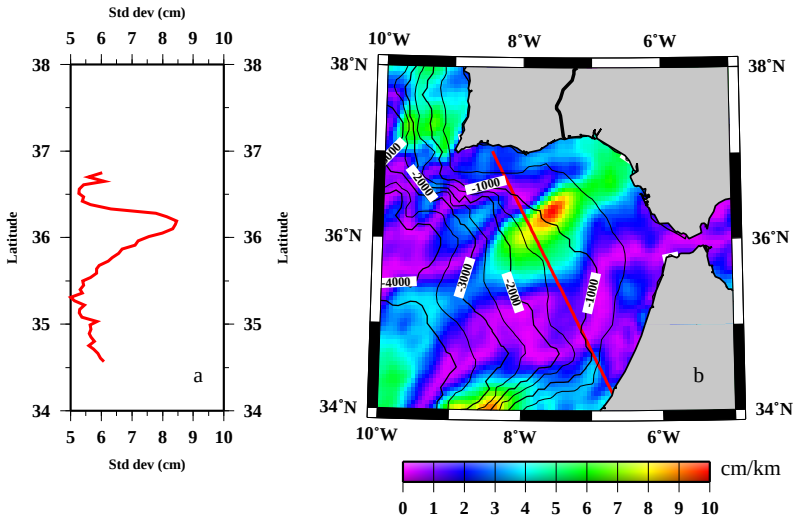

Figure 2.14: a) Sea surface height variability downstream of the Mediterranean outflow along the T/P ground track shown in red in b). b) Magnitude of the KMS2000 mean sea surface gradient perpendicular to the red T/P ground track (colors). The contour lines denote the bathymetry

(which is similar to the GSFCMSS) reveals that the region with enhanced variability coincides with large gradients in the mean sea surface (figure 2.14b). The slopes perpendicular to the satellite ground tracks shown in the figure exceed 8 cm/km and According to the Pathfinder team the algorithm that performs the interpolation of the data is correct (B. Beckley, personal communication) but there might be some inconsistencies in the mean sea surface on smaller scales. As the mean sea surfaces are derived from T/P and ERS altimeter observations, it is clear that whereas the mean surface is well determined along the tracks, higher uncertainties exists perpendicular to the tracks, since the track spacing is much higher than the alongtrack sampling. At the moment it is thus not clear whether the enhancement in figure 2.14a is due to mixing processes in the Mediterranean outflow plume or arise from an incorrect correction of observations up to 1 km away from the exact repeat ground track. As mentioned above, examination of the mean sea surface gradients perpendicular to the satellite tracks in the DS and FBC overflow showed that errors in this correction is not an issue in these overflow regions because MSS variations were small and did not coincide with the variability signal observed here.

Charlie-Gibbs Fracture zone overflow.

The overflow through the Charlie–Gibbs Fracture Zone is related to the Faroe Bank channel overflow as noted in section 2.1.2 because the North East Atlantic Deep Water that overflows from the east to the west is the product of the ISOW that has entrained ambient water along the way from the sills. Saunders (1994) reported a westward overflow from Iceland basin into the Irminger and Newfoundland basins of 2.4±0.5Sv. The overflow occurs mainly through the northern transform valley with a

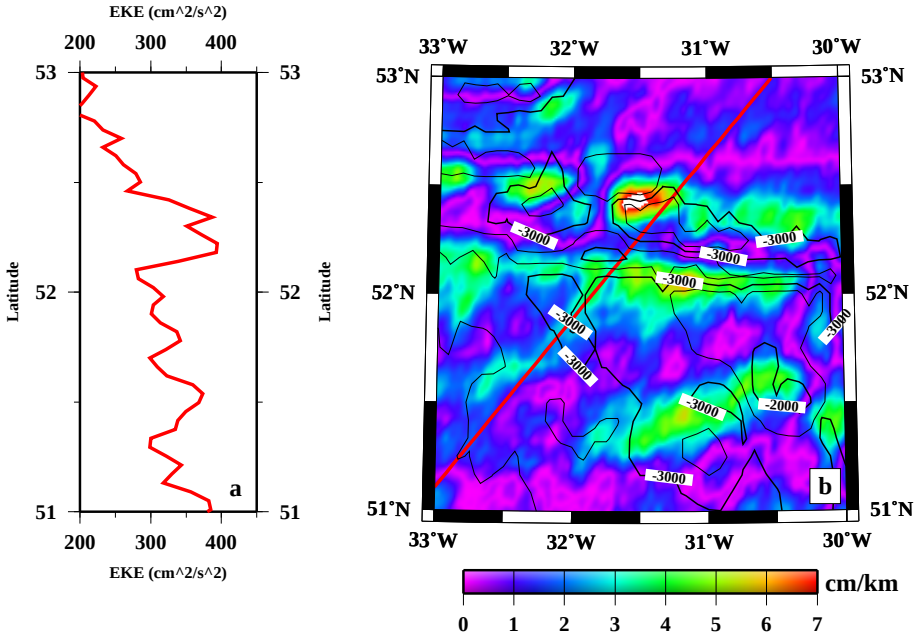

Figure 2.15: a) Eddy kinetic energy from T/P observations in the Charlie-Gibbs Fracture Zone along the T/P ground track shown in red in b). b) Magnitude of the KMS2000 mean sea surface gradient perpendicular to the red T/P ground track (colors). The contour lines denote the bathymetry

sill of 3600-3700 m close to 35°W but overflow water was also found in the southern transform valley with a sill near 30W at the same depths. Year long current meter observations detected large fluctuations with eddy kinetic energy up to 60 cm^2/s^2 distributed over periods of 10-400 days, in principle large enough to be detectable with the satellites

Figure 2.15 shows the time mean eddy kinetic energy from T/P observations along a groundtrack that crosses the Gibbs-Fracture Zone (left) and the magnitude of the mean sea surface gradient perpendicular to the track (right). The contour lines in the right figure represent bottom depth and show the complex topography in this region with depth variations of 2000 meters within 10-20 km. The large variations are also associated with mean sea surface gradients that can induce significant variability in the satellite data if not corrected for. The sill in the southern transform valley is located close to where the T/P track detect a large increase in Eddy Kinetic energy of about 100 cm^2/s^2 above the background level of 250-300 cm^2/s^2. The enhancement might be due to fluctuations in the overflow water but again the gradient in the mean sea surface coincide with enhanced variability in the satellite data, questioning the origin of the enhancement.

The two examples above demonstrate the limitations in detection of overflows with satellite altimetry. Uncertainty in the mean sea surface perpendicular to the ground tracks makes interpolation of displaced observations a crucial task in regions with large mean sea surface variations on small scales. Investigation of other overflows such as the Romanche and Vema Fracture Zone overflows revealed the same problems with coincidence of enhanced variability and large mean sea surface gradients in some

tracks.

Future satellite gravity missions such as GRACE, GOCE and CHAMP as well as more altimetry observations off the repeat ground tracks hopefully will reduce the uncertainty in the mean sea surfaces substantially, thus allowing to use satellite altimeter observations to investigate overflows in all areas including the fracture zones. One development which can be future work is to use the exact satellite positions for every track to estimate the cross-track slope. The altimeter record with more than 300 observations should provide good statistics for a narrow band of $\pm 1-2$ km around the exact repeat ground tracks and the data can thus be used directly to estimate the cross track slope.

3

Mixed layer deepening estimated from satellite data

3.1 Motivation

This chapter deals with the possibility of using satellite altimetry sea surface height (SSH) observations in combination with AVHRR sea surface temperature (SST) observations during fall and winter to estimate the deepening of the ocean mixed layer.

The importance of the description of the oceanic mixed layer is evident as this is the layer through which the atmosphere communicates with the oceans and the oceanic interior. The depth and temperature of the late winter mixed layer are, e.g. important for the process of subduction of water into the main thermocline. Iselin (1939) was one of the first to discover a close relationship between waters in the main thermocline and March surface waters at higher latitudes. Later, Stommel (1979) noted that it was as if a demon[1] operated to select mixed layer properties during a short interval in late winter ($\sim$ 1 month) to pass into the permanent thermocline. At present it is considered well-known that the source for waters in the main subtropical thermocline is the sea surface at higher latitudes where the isopycnals outcrop during winter. Temperature anomalies have been followed from the surface advecting to the south and down into the main thermocline in the North Pacific with a time scale of around 10 years (Deser et al., 1996, Schneider et al., 1999, Zhang et al., 2001).

The water masses which are being subducted are very homogeneous in the vertical and over large spatial distances and they stand out in a volumetric census in the ocean basins. The large water masses are called Mode Waters, and examples from the North Atlantic are: North Atlantic Subtropical Mode Water (or 18 degree water) with temperature around 18°C (Worthington, 1959) and Subpolar Mode Water with temperatures of 8-12°C (see e.g. McCartney and Talley (1982)).

The role of mode water variability in the climate fluctuations due to e.g heat transport is not yet understood in detail (Hanawa and Talley in: Siedler et al., 2001) but it is clear that key questions are the late winter mixed layer depth and temperature in the regions that ventilate the main thermocline. The North Atlantic has been chosen here as the study area because, as seen in figure 3.1, this is one of the areas outside of the Southern Ocean where the largest late winter mixed layer depths are found. The thick mixed layers are associated with large fluxes of heat from the ocean to the atmosphere which also give rise SSH variations due to a steric effect. As the study region thus is associated with large seasonal SSH variations, effects of measurement errors in the T/P observations will be reduced.

The structure of this chapter is as follows: Section **??**,**??** and **??** give a short

[1] In analogy with Maxwells demon in the kinetic gas theory

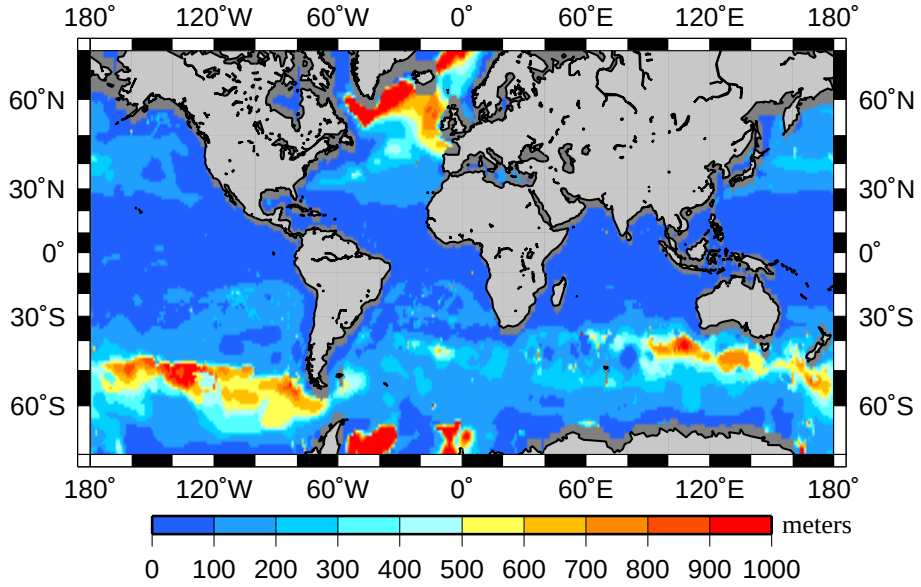

Figure 3.1: Maximum mixed layer depth from monthly WOA 1998 climatology. The criteria used here is the $\Delta\sigma_\theta = 0.125 kg/m^3$

introduction to mean conditions and the variability of the currents in North Atlantic. Estimates will be given in section 3.3 of the contribution to SSH variability from other processes than mixed layer deepening. The principles behind the mixed layer deepening are presented in section 3.4 followed by a sensitivity analysis in 3.5. Finally, in section 3.6 and 3.7, the theory will be tested against hydrographic data at two test locations: The Ocean Weather ship MIKE and along the repeated XBT line AX03.

3.2 Mean conditions and variability in the North Atlantic

The following section will describe the pathway of the ocean circulation from the Straits of Florida via the Gulf Stream and the North Atlantic Current towards the Atlantic inflow to the Nordic Seas. This is the main oceanic path for poleward heat transport in the North Atlantic and is associated with large heat fluxes from the ocean to the atmosphere and hence large winter mixed layer depths. The literature on the upper ocean circulation in the North Atlantic is very large and it is not the intention to give a review of all the results here. The section will focus upon the conditions in the region of interest to this study.

3.2.1 Mean Conditions in the North Atlantic

Strait of Florida to Midatlantic Ridge

This description initiates with the 30 Sv flow of warm water through the Strait of Florida (see e.g. Schmitz and McCartney, 1993). Along the East coast of the United States, the Gulf Stream is joined by recirculating waters from the Sargasso Sea and the transport is increased to 70-100 Sv at Cape Hatteras, where the current separates from the coast. After the separation, the Gulf Stream Extension has the form of a free flowing jet that entrains water and enhances the transport to a maximum of ~150 Sv

around 65°W (Rossby, 1996). The inertial jet that separates the cold subpolar water from warm subtropical water, meanders and generates eddies. Cold core cyclonic eddies are found south of the jet and warm core anticyclonic eddies north of it. The cold core eddies are most pronounced with a diameter of 100-200 km, lifetimes longer that one year and maximum velocities comparable to the jet (> 100 cm/s) (Käse and Krauss, 1996).

The region south of the Gulf Stream Extension is the formation area of Subtropical Mode Water (Woods and Barkmann, 1986). Large mixed layer depths are found here during winter (figure 3.1) and the southward subduction of the 18°C mode waters fills the thermocline in the western subtropical gyre (Hanawa and Talley in: Siedler et al., 2001, Marshall et al., 1993).

The mean path of the current east of 65°W is sketched in figure 3.2 and it reveals that the main current is divided into three branches around 45°W. The branches are:

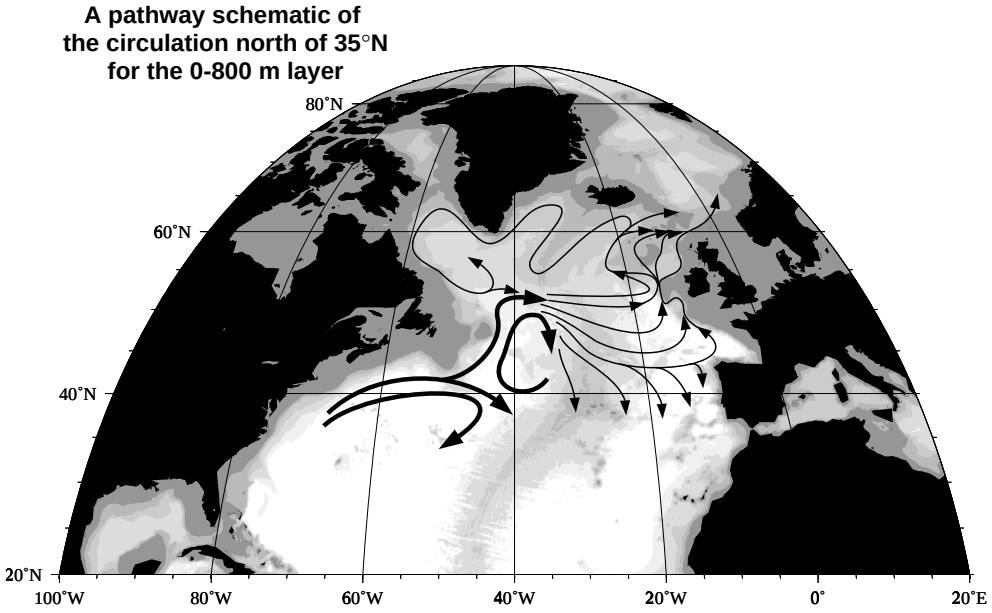

Figure 3.2: Schematic of the circulation for the upper 800 m in the North Atlantic, from McCartney and Mauritzen (2001).

A southward recirculating branch in the Sargasso Sea, a weak eastward flow of the Azores Current and the North Atlantic Current (NAC) that follows the continental slope to the north. The schematic also outlines an anticyclonic recirculation in the Newfoundland basin (around 40°W, 40-50°N) which is known as the Northern gyre after Worthington (1976). His view of a closed Northern gyre circulation has been modified and today it is widely believed that the northward NAC turns eastwards in what is called the Northwestern Corner about 52°N, 42°W. The NAC current broadens significantly after the Northwest Corner and becomes much weaker with a transport of around 20-25 Sv (Rossby, 1996, Krauss, 1986, Pollard et al., 1996).

The Subpolar Front is the boundary between the subpolar and subtropical gyre and is related to the northernmost branch of the NAC. Due to the transient nature of the currents, it is difficult to estimate the mean location of the Subpolar Front

but the maximum SST gradient in figure 1.5 indicates that the front is almost zonal along 52°N from 45°W to 25°W. The front appears to be topographically fixed at the Charlie Gibbs Fracture Zone at $35°W$, 52°45′N (Sy, 1988, Sy et al., 1992). The fixation of the front is supported by altimeter results which, using the eddy variability as a surrogate for the mean current, show no significant seasonal change in the NAC location across the MAR (White and Heywood, 1995).

East of Midatlantic Ridge

The currents east of the Midatlantic Ridge (MAR) are drawn with thin lines in figure 3.2 to illustrate the weak circulation (< 10 cm/s) in this region (see e.g. Fratantoni, 2001). Due to the weak flow there is still some debate about the exact pathways of the NAC and e.g. papers by Krauss (1995), Sy et al. (1992) and Pollard et al. (1996) do not find any southward recirculating branches from the NAC eastwards of the MAR as indicated in the figure here. There is agreement, however, that most of the NAC turns northwards and broadens. According to data from the VIVALDI 1991 survey (Pollard et al., 1996) the current turned between 20-25°W with a transport of 20 Sv in 1991. This is in agreement with Aken and Becker (1996) who estimate the northward transport in the north-eastern North Atlantic to be 23 Sv, where the NAC contributed 20 Sv and the eastern boundary current carried 3 Sv.

The transition region between the North Atlantic subpolar and subtropical gyres in the eastern North Atlantic between 40 and $55°N$ has a very weak and complex circulation on the order of centimeters (Arhan, 1990). As the water from the NAC progressively loses heat along the way, the winter mixed layer depths in this region are very large as seen in figure 3.1. The sharp southward decrease in winter mixed layer depth at around 42°N together with southward circulation in this region lead to subduction of Subpolar Mode Water[2] (Paillet and Arhan, 1996) with temperatures around 11-12°C. Aken (2001) estimates the southward velocity east of 20°W between 32°N and 52°N to be about 1 cm/s leading to a subduction of 4.5 Sv.

The northward flowing water poleward of 50°N in the northeastern North Atlantic with very large winter mixed layer depths (> 700 m) was also named Subpolar Mode Waters by McCartney and Talley (1982). A more appropriate name for this water mass might be Modified North Atlantic Water with $7.5 \leq T < 8.5$. The circulation of this water mass before it enters the Nordic Seas or the Labrador Sea is still under debate and even recent circulation schematics such as figure 3.2 differs significantly from the suggested circulation in Hansen et al. (2001). The discrepancies will not be discussed here as the circulation in this region is not the scope of this study.

Inflow to Nordic Seas

The inflow of North Atlantic water to the Nordic Seas across the Scotland-Greenland ridge occurs west of Iceland (1 Sv), between Iceland and the Faroes (3.3 Sv) and along the continental slope in Faroe-Shetland channel (3.7 Sv) (Hansen and Østerhus, 2000). North of the ridge, the Atlantic inflow is confined to the slope off Norway in a western and an eastern branch as detected in the Svinøy section running northwest from the Norwegian coast at $62°N$ (Orvik et al., 2001). The western branch has the characteristics of an 400 meter deep unstable jet carrying about 3.4 Sv whereas the

[2]Note that the southward flowing water is called Subpolar Mode Waters (McCartney and Talley, 1982) even though it participates in the northeastern subtropical gyre circulation

eastern branch is a topographically trapped barotropic current with a mean transport of 4.2 Sv. Both branches have a jet like appearance with width of about 30-50 km and maximum velocities around 1 m/s.

3.2.2 Current Variability

The number of papers that has been written on the temporal variability of the currents in the North Atlantic is substantially lower than papers on the mean conditions and very few papers deal with the seasonal variability of the North Atlantic Current. The lack of papers on this subject may indicate that variations with annual timescale do not dominate.

Several studies using in situ observations of current, temperature and salinity and satellite observations of SSH and SST have concluded that the annual variability in the Gulf Stream is small (Frankignoul et al., 2001, Esselborn, 2001, Rossby and Gottlieb, 1998). However, Yaremchuk et al. (2001) have used an inverse model to show that seasonal variations in the NAC may be important for the currents in the area $40° - 55°$N and $10° - 40°$W. The maximum westward transport was found in April-May (61 $\pm$5 Sv) and minimum in October-November (42 $\pm$3 Sv) but the results depend upon the method they use. Small ($\sim$2 Sv) seasonal variation was found when altimetry observations were added to the model.

One of the few studies that focus upon temporal variability of the NAC is the paper by Belkin and Levitus (1996). They find the subpolar front around the MAR to vary up to 300 km meridionally within a few months with no distinct seasonal cycle. Interannual variations were also observed and were probably related to arrivals of Great Salinity anomalies (Belkin et al., 1998). The variations in the front are seen both east and west of the ridge but appear to be topographically fixed immediately south of OWS C at 35°W, as reported by Sy et al. (1992).

In the region east of the MAR, Bersch et al. (1999) reported on interannual changes in the location of the Subpolar Front, which is oriented north-south in this region due to the northward turn of the NAC. Repeated occupations of a transect between Greenland and Ireland showed the location of the front to vary significantly from year to year (Bersch et al., 1999). The most pronounced changes were observed in the Iceland Basin in 1996 where warmer and saltier water was associated with a westward retreat of the Subpolar Front from 24-28 W in 1991 to 32W in 1996 along the transect. The changes in the front are related to the atmospheric conditions which can be represented by the North Atlantic Oscillation index (Hurrell, 1995). The index is defined as the standardized sea level pressure difference between Lisbon and Iceland and the winter values are shown in figure 3.3. The negative NAO index during 1996 indicates a lower westward wind stress in this year resulting in a decreased gyre circulation and hence a westward retreat of the SPF (Bersch et al., 1999). These results are corroborated by White and Heywood (1995) who observed an eastward shift of the Irminger Current in winter 1994 compared to the winter 1993 which could also be related changes in the NAO.

The inflow of Atlantic water to the Nordic Seas has been monitored five years and a strong variability was found in the inflow, with monthly transport values ranging from 2 to 8 Sv. (Orvik et al., 2001). A seasonal cycle was also observed in the inflow

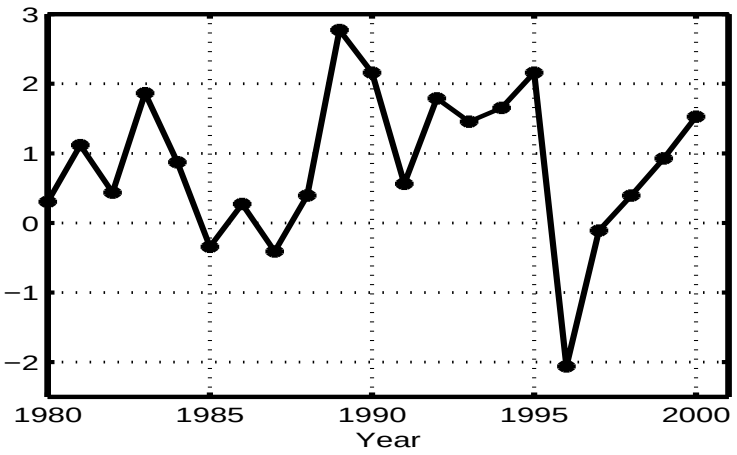

Figure 3.3: North Atlantic Oscillation Index, defined as the standardized sea level pressure difference between Lisbon and Iceland. Shown are winter values.

with a winter maxima and a summer minima in the transport and four out of the five years showed good agreement between changes in the NAO index and the estimated transports.

Recent results indicate that on the scales of gyre circulation, the NAO index is an important index on interannual and inter decadal timescales. Curry and McCartney (2001) have shown that a weakened transport in the Gulf Stream and North Atlantic current during the 1960s was related to low NAO and an increase in the transport over the last 25 years was related to increasing NAO values.

3.2.3 SSH variability

Compared to the variability of currents in the North Atlantic, sea surface height changes are much easier to document due to the availability of satellite altimetry observations. The structure of the large scale SSH variability is shown in figure 3.4 where the T/P SSH standard deviation has been calculated in every point along the tracks and subsequently gridded with smoothing scales of 200 km. The two test sites use later in this chapter: The repeated XBT line AX03 and the Ocean Weather Ship Mike are also displayed. The figure shows that the SSH variability in the northwestern subtropical gyre is almost an order of magnitude larger than the SSH variability in the eastern North Atlantic and in the subpolar gyre. The region with elevated variability extends from the separation of the Gulf Stream to the Northwest corner and is primarily due to meandering of the current and Gulf Stream rings. The timescales of the meanders depend upon the size of the meanders but the most energetic meanders have timescales between 4 and 100 days Käse and Krauss (1996).

Esselborn (2001) examined how much of the North Atlantic SSH variability in gridded ERS and T/P observations that that could be explained with a simple annual harmonic fitted to the data. The percentage of explained variance by the annual harmonic (r-squared value) was generally below 50 in the region with SSH variability

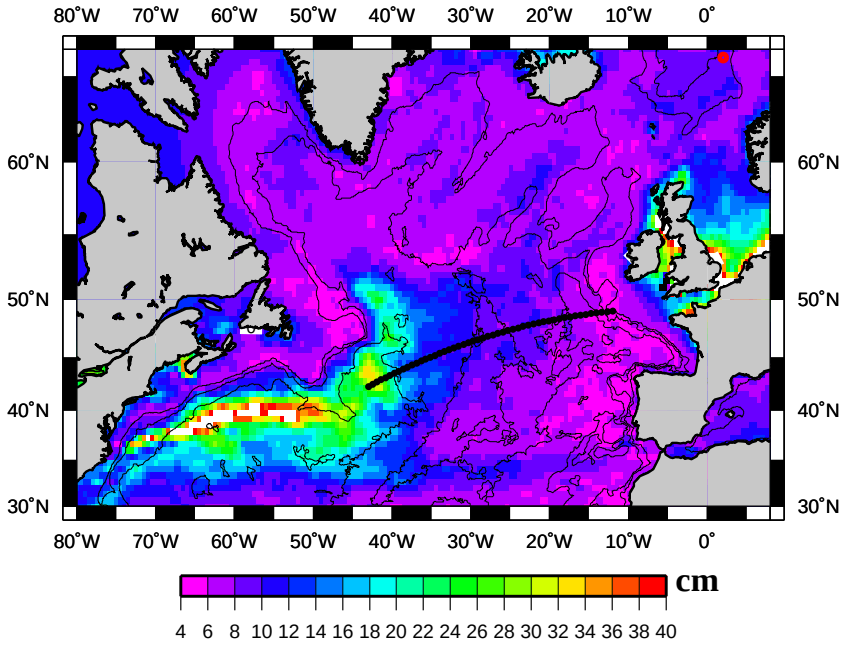

Figure 3.4: Sea surface height variability in the North Atlantic from T/P observations. The solid black line indicate the mean location of the AX03 line and the red circle the location of the Ocean Weather Ship Mike. The bathymetry is contoured with contour interval of 1500 m.

above 10 cm in figure 3.4 whereas more than 70% of the variance in the eastern North Atlantic arise from annual variations.

Interannual changes of several centimeters over the subpolar and subtropical gyres have been observed in the North Atlantic (Esselborn and Eden, 2001). The large drop in NAO index in the winter 1996 (figure 3.3) represent large changes in the atmospheric circulation. Compared to the previous winter, the changes in the atmospheric forcing during winter 1996 led to a sea level drop of of 3-8 cm in the subtropical gyre and a rise in sea level of 2-7 cm in the subpolar gyre.

The discussion above demonstrates that the by far largest variability is found in the region of the Gulf Stream Extension, west of the MAR. This variability is due to eddies and meandering of the mean current. East of the MAR, a significant part of the variability arises from the annual sea surface height variations. The annual variability in NAC appears to be low for most of the northeastern North Atlantic but seasonal variability in the warm inflow to the Nordic seas has been observed. Interannual changes in the NAO index are related to changes in the North Atlantic conditions such as the locations of the subpolar front and the large scale gyre circulations. Recent studies suggest that decadal changes in the NAO index are also related to changes in the Subtropical Mode Waters at Bermuda (Joyce et al., 2000).

3.3 Contribution to sea level variability

In this section we will first assess the errors introduced by assuming that the heat storage over a given area in the North Atlantic is due to Air-Sea heat fluxes. Next,

the relationship between variability in Sea surface heights and changes in heat content will be addressed and finally we will focus on the error sources in the North Atlantic and estimate the errors involved in converting winter SSH drop over 5 degrees bins into heat content changes.

3.3.1 Local Heat balance

The balance of heat in the water column can essentially be described by the equation below, relating temperature changes to surface heat fluxes and advection

$$Q_{surf} = \int \rho c_p \frac{\partial T}{\partial t} dz + \int \rho c_p \vec{u} \cdot \nabla T dz \tag{3.1}$$

Where the integral is carried out from the bottom to the surface. Gill and Niiler (1973) used scaling arguments to show that on large spatial scales on the order of 1000 km and seasonal ($\sim$ 2 months) time scales, advection of heat is negligible compared to the surface heat fluxes. Their conclusions are supported by (Yan et al., 1995) who demonstrated a very good agreement between monthly local heat storage from XBT observations and surface heat fluxes. The study was carried out for $5^\circ \times 5^\circ$ bins all across the North Pacific at 30-40°N latitude and the basin–wide difference between monthly heat flux and storage rate was $3.76 W/m^2$. Reducing the averaging scales to $2^\circ \times 2^\circ$ led to significantly lower correlation especially in the western region associated with the Kuroshio.

3.3.2 Air-sea heat flux and SSH changes

When the correlation between surface heat fluxes and temperature changes exist as described above, surface heat fluxes and SSH changes are also coupled through the steric height equation. An estimate of the size of the SSH drop can be given from climatological winter surface heat fluxes at a given position in the North Atlantic (60°N, 15°W). The mean outgoing heat flux from December through March is 160 W/m^2 and the integrated heat flux during these 4 months corresponds to a depression of the sea surface of 6.2 cm, when winter mixed layer values are taken from McCartney and Talley (1982) ($T = 8^\circ C, \rho = 1027 kg/m^3$ and mixed layer depth of $400m$).

In general, the equation for seasonal sea level variations consists of three terms

$$\eta_{obs} = \eta_{sal} + \eta_{temp} + \eta_{bt} \tag{3.2}$$

where the sal and temp refer to the vertically integrated steric changes due to salinity and temperature anomalies, respectively. The last term in equation 3.2 is the barotropic term that represents the sea level changes related to changes in bottom pressure. Sea level variations from changes in sea level pressure are not included in equation 3.2 because they are corrected for in the T/P observations used here. Gill and Niiler (1973) showed by scaling arguments that a balance between the left hand side and the second term on the right exists on large scales. They used climatology in $5 \times 5^\circ$ bins to support their results.

The seasonal behavior in the North Atlantic of upper ocean temperature, surface heat fluxes and total steric anomaly (including salt) is illustrated by figure 3.5. The

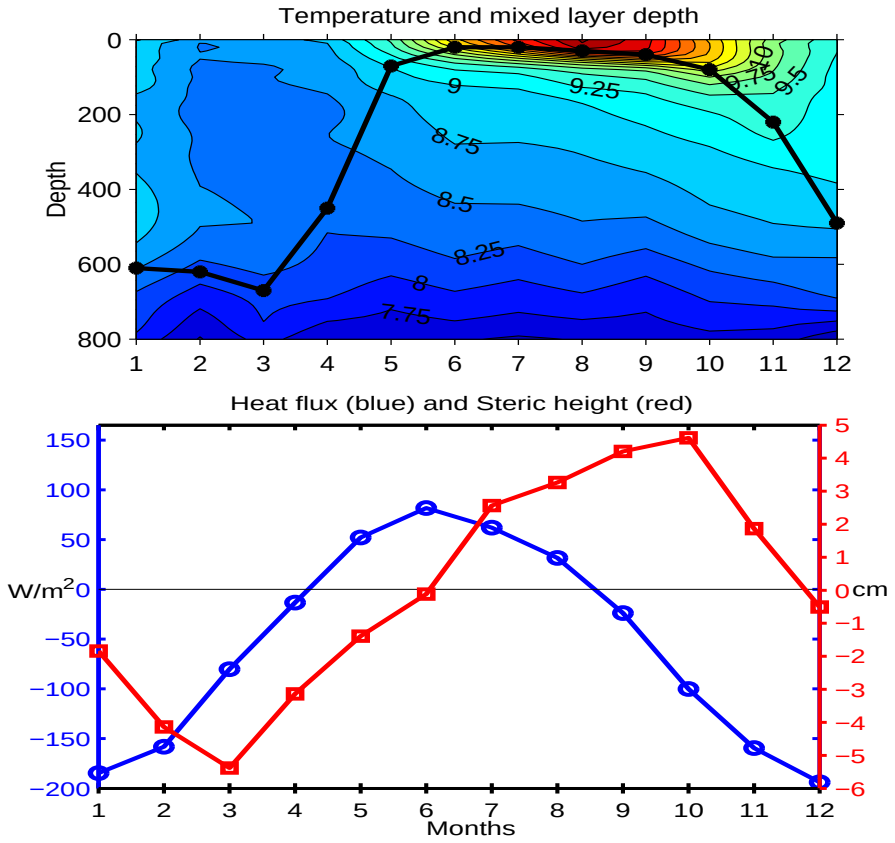

Figure 3.5: Upper: Time-depth plot of upper ocean climatological temperature in colors. The mixed layer depth is overlaid in black. Lower: Climatological downward surface heat fluxes from Esbensen and Kushnir (1981) (blue) and steric heights anomalies from WOA 1998 (red). All time series are from the North Atlantic 15°W 60°N

figure demonstrates the close correlation between winter mixed layer depths and steric heights with March being the turning point for both values. The steric drop in SSH during winter corresponds to the 6.2 cm estimated only from sea surface heat fluxes at the same position. The difference includes discrepancies between the (Esbensen and Kushnir, 1981) and the WOA 1998 climatologies, the steric height due to salinity and heat contribution from the advection term.

Large scales, O(1000 km)

Several studies support the strong coupling between surface heat flux and SSH changes on large spatial scales. In situ temperature observations from XBT lines and T/P observations have been used in several studies (White and Tai, 1995, Wang and Koblinsky, 1997, Gilson et al., 1998) and corroborate the results in Gill and Niiler (1973): The agreement between heat fluxes derived from SSH observations and derived from temperature observations is very good on large scales. Of particular interest to this study is the results by Wang and Koblinsky (1997) where heat content changes along the XBT line Ax03 in the Northeastern Atlantic are compared with T/P derived results. The heat flux estimates agree within the uncertainty which is on the order of

$20 - 30 W/m^2$.

Model results

Various model products have been used together with T/P to examine the individual terms in equation 3.2. Stammer (1997) compares the steric sea level variability derived from ECMWF heat fluxes with 3 years of T/P observations in basin averages over 10 degrees meridionally. The residuals between steric variability and satellite observed SSH decrease toward north in the Atlantic with a variance of $\simeq 3cm^2$ at $45°N$ compared to a total signal variance of $15cm^2$. A regional model of the North Atlantic, is used in Ferry et al. (2000) to examine the annual amplitude of the different terms in equation 3.2. Heat fluxes contribute to a dominating part of the SSH variations. The advection term is the second largest term with amplitudes < 0.5 cm in the northeastern Atlantic. The other terms such as the deep steric changes, the haline component and the bottom pressure component have amplitudes smaller than the advection term and are thus not significant. In the interpretation of the model results it is, however, important to remember that these two coarse resolution models underestimate the variability due to meso-scale eddies.

In general, the uncertainty in the seasonal heat fluxes derived from T/P is on the order $3 - 40 W/m^2$ depending on the averaging region. Some of the studies uses the heat fluxes from meteorological reanalysis data set such as ECMWF and NCEP as reference. These data set contain errors of the same size (Josey, 2000) which also contribute to the uncertainty in the T/P derived seasonal and longer term heat fluxes.

Some of the results derived above are derived for spatial scales O(1000 km) that are too large to be used with winter mixed layer depth and subduction. As seen in figure 3.1 there is substantial spatial variability in the maximum mixed layer on the 1000 km scales. Averaging scales scales of $5 \times 5°$ will be used here which affect the magnitude of some of the terms in equation 3.1 and 3.2.

Averaging scales <1000 km

The assumption that advection can be neglected in equation 3.1 is more valid when the spatial scales are large but the results in Yan et al. (1995) indicate that averaging over 5 degrees bins gives a very good correlation between the first and the second term in equation 3.1. The paper finds significant degrading of the results on 2×2 bin sizes but results from weather ships in the Atlantic and Pacific indicate that good point wise agreement between local heat fluxes and heat storage can be obtained (Gill and Niiler, 1973, Tabata, 1965). These studies focus upon the heat balance throughout the year but the importance of the advection term in this study is likely to be reduced even more, as large negative surface heat fluxes are found in the study region during winter.

The largest effect of a reduction in the spatial scales is probably in the estimation of SSH where the barotropic term in equation 3.2 can become important. As described in section 3.2.2, large changes have been observed in the position of the subpolar front. In analogy to such a change we investigate the effect it would have on the sea surface if a meridional barotropic current of 10 Sv over a zonal distance of 5 degrees at a latitude of 60°N was shifted 5 degrees. If the geostrophic velocities are assumed

to be barotropic, the slope of the sea surface is

$$\frac{\partial \eta}{\partial x} = \frac{Vf}{gHL_x} \tag{3.3}$$

Where V is the total transport through a plane of depth H and distance L_x. With typical values of $H = 2500m$, $V = 10 \cdot 10^6 m^3/s$, $f = 2\Omega sin\theta$, $L_x = 5 \cdot 111 \cdot cos\theta$ km the mean current speed over 5° longitude is 1.5 cm/s and the slope is: $\partial\eta/\partial x = 1.8 \cdot 10^{-7}$. The maximum sea surface signals associated with a longitudinal shift of this meridional current is thus $\sim$ 5 cm. The estimated surface signal is derived under the assumption that the temperature and salinity properties of the water remain the same.

Another concern as the bin size decreases is the effects from eddies. According to Stammer and Wunsch (1996) the typical spatial scales of the eddies at latitudes around 50°N in the Atlantic is $\sim$75 km with an integral time scale of $\leq$30 days and will therefore give a minimal effect on the seasonal SSH variability. It is also clear that the bathymetry in the North Atlantic region is important to the circulation. Slope currents along the Eastern boundary in the North Atlantic and the East Greenland current are two examples of currents that should be avoided in the analysis.

On the basis of the results presented above it is a good approximation to assume that sea level variations observed in $5 \times 5°$ regions on time scales of several months are to first order related to surface heat fluxes. A conservative estimate of the sea level variability from other sources than surface heat flux is an error variance of $\leq$ 2 cm away from topographic features such as the Reykjanes Ridge and areas with swift currents such as the NAC west of the Midatlantic ridge. This is in agreement with Wang and Koblinsky (1997) that estimate errors of annual steric height variations of about 0.7 cm including the barotropic term in equation 3.2 and treat advection of heat as noise with variance 0.5 cm.

3.4 Principles of mixed layer deepening from SSH and SST

The idea of estimating the late winter mixed layer depth rests upon the assumption that the mixed layer deepening which is observed through late fall and winter is associated with a heat loss from the mixed layer to the atmosphere. When the dominating mechanism behind the deepening is convective adjustment, changes in SSH and SST can be converted to two estimates of the heat loss and the discrepancies gives the mixed layer deepening.

The observed SSH change is transformed into a heat loss via assuming that observed SSH changes correspond to steric height changes. The steric height η_s is

$$\eta_s = \frac{1}{\rho_0}\left(\int_{-h}^{0} \frac{\partial \rho}{\partial T} T dz + \int_{-h}^{0} \frac{\partial \rho}{\partial S} S dz\right) \tag{3.4}$$

Where ρ_0 is a reference density. If the variability below the mixed layer is zero, the equation holds when the $z = -h$ is chosen as the maximum mixed layer depth throughout the year. If the contribution from salinity to the steric height is neglected

the steric height is defined only from temperature

$$\eta_s = \frac{1}{\rho_0}\int_{-h}^{0}\frac{\partial\rho}{\partial T}T dz \tag{3.5}$$

The 3 dimensional heat conservation equation on seasonal time scales can be used for water column above the maximum mixed layer depth (Yan et al., 1995)

$$c_p\rho\int_{-h}^{0}\frac{\partial T(z)}{\partial t}dz = H_{tot} \tag{3.6}$$

Where c_p is the specific heat capacity. The heat flux H_{tot} normally represents the surface heat flux but in this formulation it also includes the contribution from divergence of advective heat flux in the mixed layer. Combining the temporal derivative of equation 3.5 with the heat flux from equation 3.6 we get the relation between steric changes and heat flux in the mixed layer

$$\frac{\partial\eta_s}{\partial t} = \frac{\partial}{\partial t}(\int_{-h}^{0}\frac{1}{\rho_0}\frac{\partial\rho}{\partial T}T dz) = (\frac{1}{\rho_0}\rho\alpha\int_{-h}^{0}\frac{\partial}{\partial t}T dz) = \frac{\alpha H_{tot}}{\rho_0 c_p} \tag{3.7}$$

Where the thermal expansion coefficient, $\alpha = \rho^{-1}\partial\rho/\partial T$, is assumed constant throughout the mixed layer. Under the assumption that changes in steric height corresponds to changes in SSH we can estimate the changes in heat content from time t_1 to t_2 from SSH changes by

$$Q_{SSH} = \frac{\rho c_p}{\alpha}(\eta(t_1) - \eta(t_2)) \tag{3.8}$$

In this context, positive heat content changes are associated with a heat loss out of the mixed layer. SST is equal to the mixed layer temperature under the assumption of a perfectly mixed layer that is homogeneous in T and S. Temporal changes in SST together with a mixed layer depth can therefore be used to give an estimate of the heat loss from one time to the next, if the mixed layer depth (mld) does not change.

$$Q_{SST} = \rho c_p(SST(t_1) - SST(t_2)) \cdot mld \tag{3.9}$$

From changes in SST and SSH we now have two independent estimates of the heat flux out of a mixed layer of constant depth. Note that the mixed layer depth is not explicitly stated in equation 3.8 but it enters through the pressure dependance of the thermal expansion coefficient. Without introducing large errors we can thus assume that the relation applies, even if the mixed layer is deepening. This is not the case for equation 3.9 where the mixed layer depth is a requirement.

The two estimates of heat loss are equal for a constant mixed layer and we can use the disagreement between these estimates to assess the deepening of the mixed layer from one time to the next. If the vertical temperature profile below the mixed layer is approximated with a straight line from the old mixed layer depth down to the new mixed layer depth the heat loss which is not described by equation 3.9 is

$$Q_{rest} \simeq \frac{\rho c_p(T(t_1) - T(t_2))\Delta mld}{2} \tag{3.10}$$

Where Δmld is the deepening of the mixed layer. Through balancing the heat losses and use of equation 3.8, 3.9 and 3.10 we are now able to compute the deepening of the mixed layer from one time t_1 to the next, t_2 where the only required input are the SSH and SST changes and an initial mixed layer depth $mld(t_1)$

$$Q_{SSH} = Q_{SST} + Q_{rest} \tag{3.11}$$

$$\Updownarrow$$

$$\Delta mld = \frac{2(Q_{SSH} - Q_{SST})}{\rho c_p (T(t_1) - T(t_2))} \tag{3.12}$$

$$\Updownarrow$$

$$\Delta mld = \frac{2(\eta(t_1) - \eta(t_2)\rho_0}{\alpha\rho(T(t_1) - T(t_2))} - 2mld(t_1) \tag{3.13}$$

The principles behind the computation of the mixed layer deepening are sketched in figure 3.6. The relation applies for one time step but can be used for several time steps

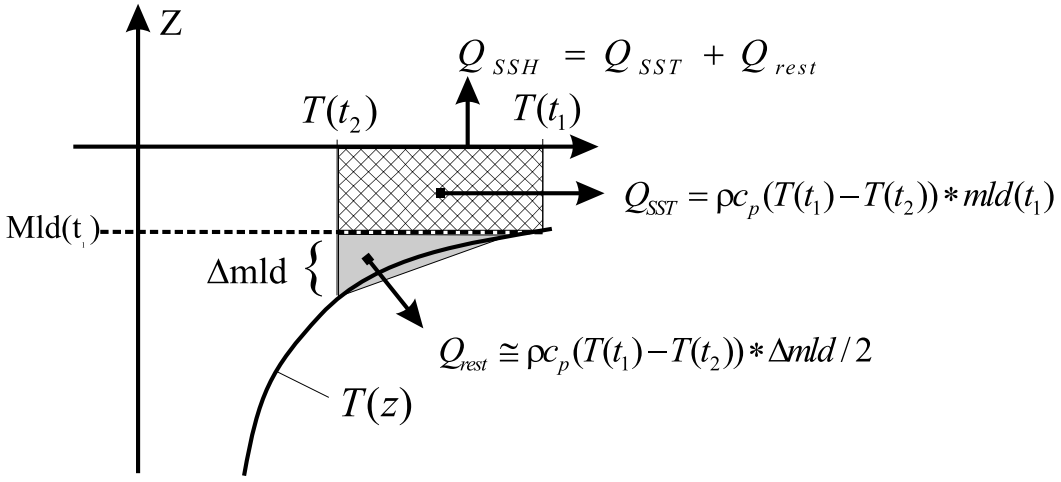

Figure 3.6: Schematic of the principles behind mld deepening estimated from satellites. The hatched area represents the heat loss calculated from SST changes and with a constant mld (equation 3.9). The gray shaded triangle represents approximated additional heat loss in equation 3.10 from the deepening of the mixed layer. The heat loss estimated from SSH (equation 3.8) includes the additional heat loss from the deepening of the mixed layer.

as long as the mixed layer is deepening. A priori knowledge about the mixed layer depth is only required for the initial conditions. In the following time steps, the mixed layer can be taken as the previous mixed layer plus the deepening from equation 3.13. Note also, that information is obtained about the vertical temperature profile when the mixed layer is deepening because the mixed layer temperature is equal to the original temperature at the depth of the mixed layer in every time step.

Several assumptions are involved in the development of the model, and their validity will be discussed below.

3.4.1 Validity of assumptions

In the heat balances for the mixed layer it was assumed that no heat transport occurred across the base of the mixed layer. This is of course a simplification because vertical diffusion of heat to the interior depends on the vertical temperature gradient which has a maximum at the base of the mixed layer. The impact of this effect was tested by adding a diffusion term to the heat balance of the mixed layer. Vertical diffusion based upon monthly climatological temperature gradients exported heat vertically out of the mixed layer at every time step. Several test with varying diffusion coefficients showed that the impact of vertical diffusion on the estimated mixed layer deepening was small (O(5m)) and the extension of the model is therefore not presented here.

An important assumption made here is that it is the convective adjustment mechanism that is responsible for the mixed layer deepening. From 1-d mixed layer models like the Krauss and Turner (1967), Niiler (1975) and Mellor and Yamada (1974) which include both differential and bulk formulation of the mixed layer, it is clear that the two primary mechanisms to account for deepening of the mixed layer are wind driven turbulence and cooling at the sea surface. Whereas the former mechanism only considers wind generated mechanical redistribution of properties within the water column, the latter requires a sea surface buoyancy flux essential to this study. In the classical boundary layer theory (see e.g Kraus (1972)), the surface wind influence on the currents decreases logarithmic away from the surface due to the law of the wall:

$$u(z) = \frac{u_\star}{k} ln \frac{z}{z_0} \tag{3.14}$$

Where k is the Von Karman constant ($\simeq 0.4$), z_0 is the roughness parameter and $u_\star = \sqrt{\frac{\tau_0}{\rho}}$ is the friction velocity. It thus clear that the region influenced by the winds is limited in the vertical. Experiments with several mld models (Martin, 1985) indicate that typical depths are about 50 meters with maximum values around 100 meters for strong wind forcing in the most sensitive models. When the mixed layer is deeper than 50-100 meters, the dominating mechanism acting to deepen the mixed layer is thus convective adjustment when the water column becomes unstable due to cooling at the surface. In the North Atlantic where late winter mixed layer depths are of the order 200-600 m as seen in figure 3.1 we therefore conclude that convection must play a dominating role in the deepening of the mixed layer through late fall and winter.

The thermal expansion coefficient α depends on the temperature, pressure and salinity but in the model we have assumed one value for the whole mixed layer. The salinity value is taken as the climatological mean of the upper 200 meters at the specific location, the pressure is half the mixed layer depth and the temperature is from the previous time step. In that way we approximate for every time step t and for the whole mixed layer, one α given by

$$\alpha(S, T, P) \simeq \alpha(S_{Clim}, T(t-1), mld/2) \tag{3.15}$$

It is therefore only the nonlinear pressure effects and the salinity deviations from climatology that give rise to uncertainties. Even drastic changes such as a salinity

decrease of 5 psu for a 10°C mixed layer result in $\Delta\alpha \leq 8\%$ indicating the validity of this assumption.

From the formulation above and from figure 3.6 it is evident that advection of heat in the mixed layer is to some extent included in the model. If the advected heat is distributed uniformly over the mixed layer it is included in both estimates of the heat content change in the mixed layer and the model still applies as long there is a net heat loss out of the mixed layer. In the North Atlantic, with the thick winter mixed layers a significant part of the advection takes place within the mixed layer. The error in estimating the heat content is thus due to advection of heat below or variations within the mixed layer and the size of these errors are therefore less than the total advection of heat.

3.5 Idealized model test

Equation 3.13 involves a ratio of differences in SSH and SST which makes the mixed layer deepening sensitive when the SST changes in the denominator are small. This often occurs during late winter before the warming begins and the effect of noise on the input data must therefore be assessed. Synthetic data generated by a 1-dimensional convective adjustment model and different noise levels will be used for this task.

The 1-dimensional model is a very simple convective adjustment model to be used only during the months of negative surface heat fluxes. It is initialized with climatological salinity and temperature profiles at the position $25°W$,$47°N$. The vertical resolution of the model is 10 meters with a time step of 1 day. Monthly surface heat fluxes are taken from the Oberhuber (1988) climatology and cooling occurs at the sea surface over the entire mixed layer, which is defined to be homogeneous. When the mixed layer becomes denser than the underlying water it deepens and entrains water from below until vertical stability is regained.

The model is initialized in September as this is the first month with negative heat fluxes at this position. The initial T and S profiles are shown in figure 3.7 as the blue lines. Shown in red are the mixed layer values after 100 and 210 days of cooling. No exchanges are allowed across the base of the mixed layer and the salinity in the mixed layer is therefore the vertical mean value for the mixed layer which is also seen for the two model profiles. Despite the simplicity of the model, it performs well in predicting the mixed layer depth. The 210 days correspond to the 7 months with negative heat fluxes at this position and the predicted late winter mixed layer depth of 360 m is not far from the maximum climatological mixed layer depth of $\simeq$390 m.

To assure a consistency between the generated data and the mixed layer model, the salinity was set to a constant of 35 in the vertical. This reduced the final mixed layer depth to 280 meters after 210 days of cooling. The steric height anomalies were calculated in every time step and the synthetic data thus consist of 210 daily values of: Steric height anomaly, mixed layer depth and mixed layer temperature.

The generated daily time series of steric heights and SST (or mixed layer temperature) was used as input data in equation 3.13 with an initial mixed layer depth of 30 m. As the input data were prefect, it was not surprising that the mixed layer depth was reproduced by the model within 1 m. When gaussian noise was added to the generated steric heights and SST data it was clear that the input data could not be

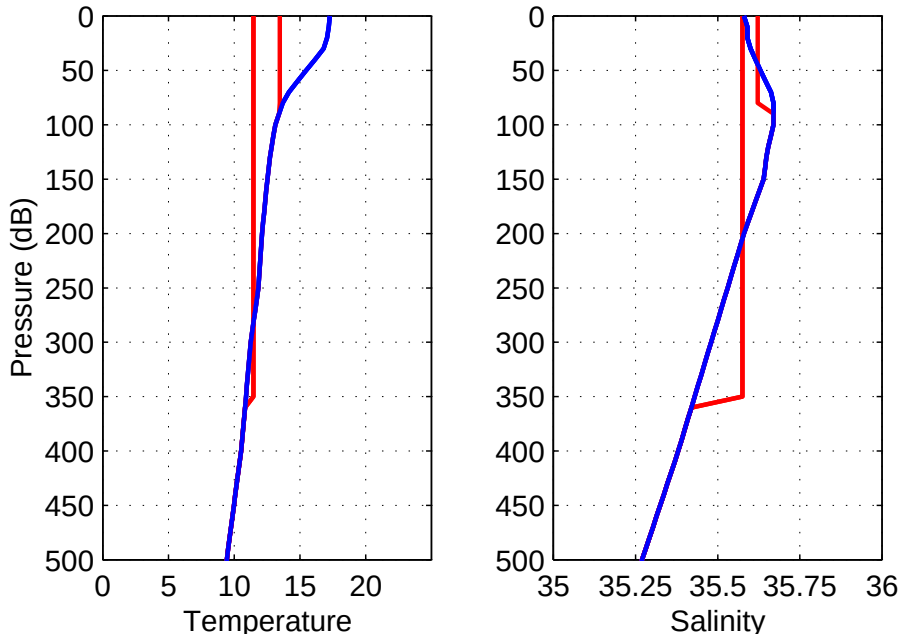

Figure 3.7: Initial climatological profiles of temperature (left) and salinity (right) shown in blue. Shown in red are the model results after 100 and 210 days of cooling

used without smoothing. Least squares fitting of 3 and 4th order polynomials were tested but found to be less robust to noise than least squares fit of an annual and semiannual harmonic. In the case of no noise on the input data the use of data from harmonic fit to the data led to an underestimation of the end mixed layer depth of 48 m due to the misfit of the annual and semiannual harmonic.

Gaussian noise was added on the steric heights and the SSTs to test the sensitivity of the estimated mixed layer depth to noise on the input data. The mixed layer deepening was estimated 25 times for every noise level and the mean difference between estimates and true end mixed layer depth is shown in figure 3.8 as a function of noise. The left and middle figures show the effect when noise is added to either steric heights or SST and the right figure shows the effect on noise on steric heights and SST at the same time. The noise levels in the last case was calculates as linearly increasing noise over the 40 levels (0-2 cm on steric heights and 0-0.4°C on SST).

The errorbars represent the standard deviation of the mixed layer depths from the 25 iterations at each noise level. Least squares fit of the semi annual and annual harmonics have been used to smooth SST and steric height signal which explains the underestimation of 48 m of the final mixed layer depth even when no noise is added. The estimated mixed layer depth after 210 days is very robust with standard deviations of less than 25 meters at noise levels below 1 cm and 0.20°C. However, as increasing noise is added, the uncertainty in the estimated mixed layers increases and exceeds 50 meters for noise levels above 2 cm. The SST appears robust with variability below 40 m in figure 3.8, but for noise levels above 0.4 °C the variability raises to several hundred meters. Noise are added on both steric heights and SST is

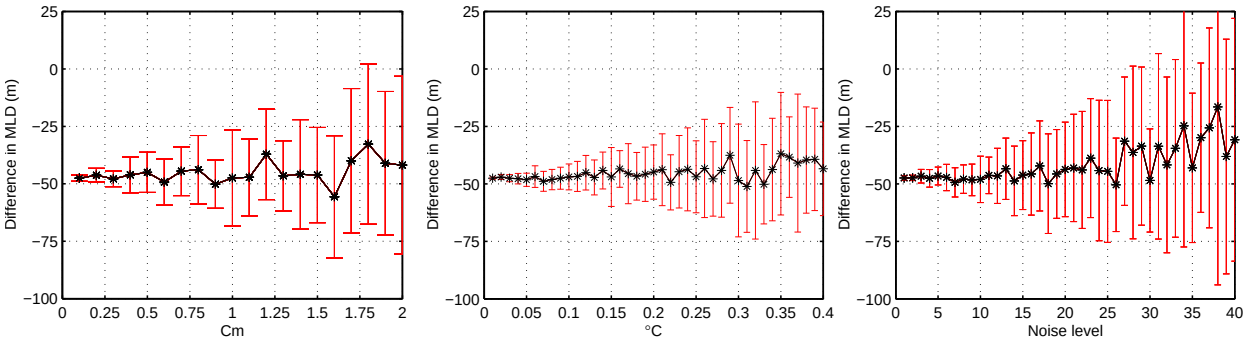

Figure 3.8: Mean difference (Estimated mld - true mld) in estimated mixed layer depth after 210 days as a function of noise added to steric heights (left) and SST (right). The errorbars represent the standard deviations of the 25 mixed layer depths for each estimate. [SST label incorrect]

seen to increase the uncertainty in the mixed layer depths but the effect is not large.

With the expected accuracies obtainable from satellites we can thus expect to estimate the late winter mixed layer depth with an accuracy of $50 - 100$ m. The agreement between SSH and surface heat flux is probably one of the most important factors together with the harmonic fitting to the steric heights. The uncertainty in the SST observations will not introduce large errors.

A time step of 1 day was used when deriving the mixed layer deepening results above but the idealized model can also be used to test the dependency of the end mixed layers on the time step. Harmonic fitting was applied to the the perfect input data with no noise and the only changing parameter was the time step in days along the harmonic curves. The difference between the estimated final mixed layer depths and the truth are shown in figure 3.9. As expected the difference is about 47 for a

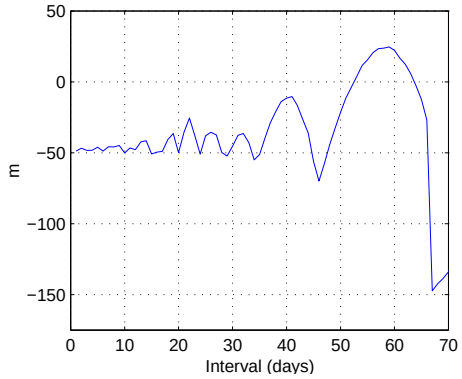

Figure 3.9: Difference in end mixed layer depths as a function of time intervals used in the mixed layer model. No noise on input data and harmonic fitting has been applied.

time step of 1 day. The difference is relatively constant for time steps below 20 days but it is clear that larger time steps involve significant uncertainties in the estimated mixed layer of minimum 25 meters. The extreme case with only the start and end

values of SST and SSH gives a mixed layer deepening of only 135 m indicating the significant error introduced by approximating the temperature profile with a straight line as in figure 3.6.

It is now clear that the principle of estimating winter mixed layer deepening from satellites involves many crucial assumptions where the assumption that SSH changes can be converted to heat content changes is the most crucial. The errors associated with the assumptions have been assessed based upon scale analysis and literature studies. Data generated from a simple mixed layer model were used to test the sensitivity to noise in the SSH and SST observations, revealing that the expected accuracy in the estimated late winter mixed layer depths is below 100 m. This should be compared to an inter annual variability in the thickness of the North Atlantic SPMW of several hundred meters (Bersch et al., 1999) and encourage us to proceed with testing of the model against real data in the following section.

Two regions in the North Atlantic have been selected to validate the mixed layer deepening estimates from satellites. Both sites are in areas with large negative heat fluxes throughout most of the year and deep mixed layers during late winter. In addition, the two sites represent some of the most frequently observed regions and they provide a good reference to test the results against. The regions may not be the first choice in relation to the validity of the assumptions, but reliable estimates of the contributions from other processes can be estimated due to the frequent temporal sampling.

3.6 Ocean Weather ship M

The Ocean Weather Ship Mike (OWSM) is located at $66°N, 2°E$, which is on the continental slope in the Norwegian Sea in the path of the warm northward flowing Atlantic surface water (Mauritzen, 1996). The weather ship is marked by the red circle in figure 3.10. According to surface drifters, the weather ship is positioned in the westernmost branch of the Atlantic inflowing water in a region characterized by high mean velocities in excess of 40 cm/s and high eddy kinetic energies ($\geq 200 cm^2/s^2$) (Poulain et al., 1996).

The observational record from the weather ship is unique because regular observations of T and S on reference depths have been made since 1948. The observations used in this study are from 1992 and later to ensure a consistent comparison with T/P observations. The time series extends to August 1998 and includes more than 1000 stations with T and S observations deeper than 700 meters. The ~ 150 stations per year are distributed evenly over the seasons with a maximum gap of 15 days. Temperature time series on selected depths from the upper 600 meters are shown in figure 3.10 b and it is clear that the upper few hundred meters contain warm Atlantic water whereas NSDW is found in the deeper part. Hansen et al. (2001) used the $\sigma_t = 28.0$ as the interface between the two water masses at OWSM and found a mean depth of the interface of ~ 550 meters. As discussed below, the advantageous temporal sampling at the OWSM may be in contrast to the position in a swift flow and in a frontal zone which can violate some of the assumptions from section 3.4.

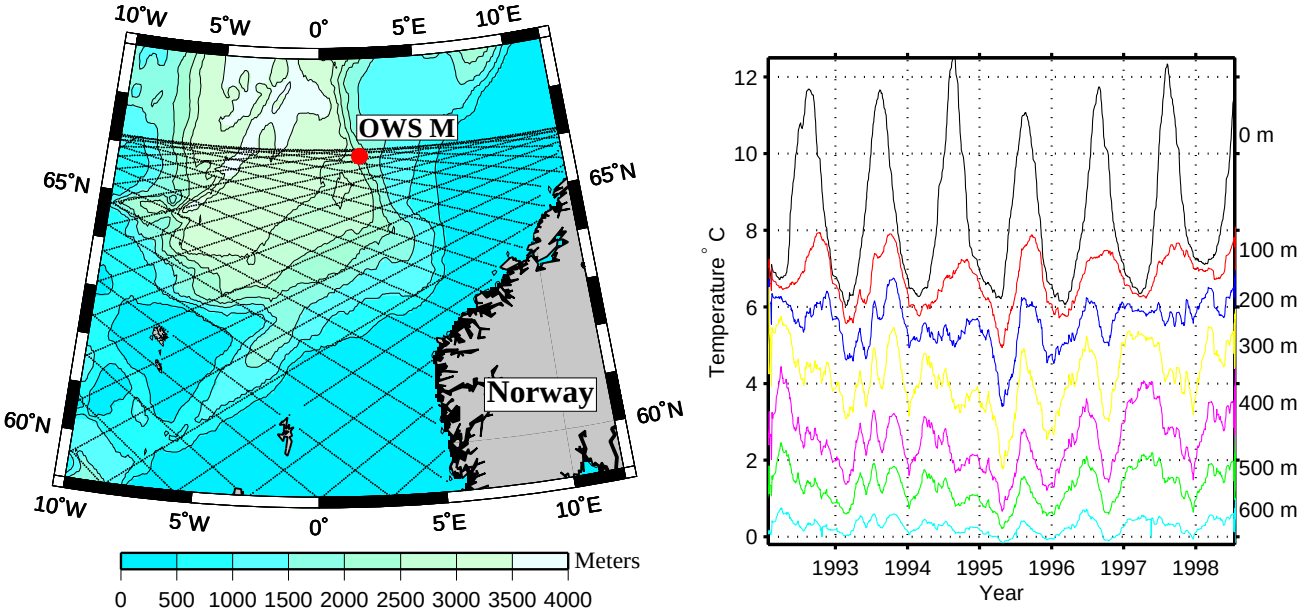

Figure 3.10: Position of Ocean Weather Ship Mike (OWSM) marked by red circle. The T/P satellite ground tracks are overlaid as solid black lines and the bathymetry is represented with the colored contours.

3.6.1 *In situ conditions*

As the OWS is situated where the warm Atlantic water flows into the Nordic Seas the region is characterized by large negative surface heat fluxes. The climatology from Oberhuber (1988) estimates an annual mean of $-84W/m^2$ with peak value in December of about $-230W/m^2$.

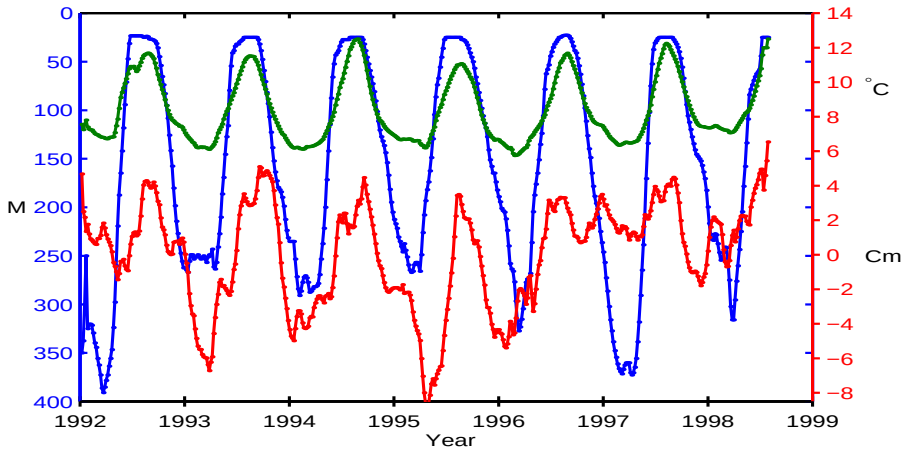

Figure 3.11: SST(green), Mixed layer depth (blue) and steric height (red) from upper 700 meters. All the results are derived from in situ observations from the OWSM.

AVHRR satellite sea surface temperature observations reveal that the weather ship is located in the Polar Front where the annual mean SST drops from about 9 to 6°C

over a few hundred kilometers. The influence from the front is also seen in the data because mesoscale eddies and other fluctuations with periods of a few days dominate the observations and smoothing is therefore required for this study. The time series from the OWSM in figure 3.11 were constructed by averaging observations within 10 days at every time step of 5 days and subsequently apply a running mean of total width 7 was before the data were plotted. The mixed layer depths were estimated as the depth where the potential density deviated more than $\sigma_t = 0.125 kg/m^3$ from the surface value. Interpolation was used between the reference depths to obtain profiles of T and S for the steric height calculation. The anomalies for the upper 700 meters are shown in red in figure 3.11 which also shows the observed SST in green.

The figure shows that the large buoyancy fluxes during winter are accompanied by large winter mixed layer depths of up to 390 meters. The depth of the mixed layer varies by more than 150 meters from year to year but the annual cycle is regular with maximum mixed layer depths during January and February. The SST also exhibit a regular annual cycle with an amplitude of 2-3 degrees which is in contrast to the irregular fluctuating steric heights that do not show a regular annual variation. An example is during the winter 1997 where no significant negative anomaly is observed despite cold SST and a very deep mixed layer. The uncorrelated fluctuations indicate that some of the assumptions about the advection of heat or the salinity contribution to steric height are not fulfilled during the year 1997.

The variability below the mixed layer is estimated by calculating the steric height anomalies from 500-1000 m. The standard deviation of smoothed anomalies is 0.49 cm which indicates that the assumption about no deep variability is good. For depths below 1000 m, the spacing between the reference depths does not allow interpolation. However, the T and S variability at the deepest reference depths is an order of magnitude smaller than at the surface and will thus not contribute very little to the SSH variability.

3.6.2 Satellite signals

From figure 3.10 it is evident that the spatial sampling of the T/P satellite close to the OWSM is dense due to the proximity of the weather ship to the turning latitude of the satellite. Within 100 km from the OWSM, the number of T/P observations per repeat cycle exceeds 200 from 12 different ground tracks. There is thus basis for constructing a precise annual SSH cycle. However, averages over regions larger than 20 km may be biased towards the south as the maximum latitude with T/P observations is 66.16°N

The average T/P time series was constructed by averaging data within 150 km from the OWSM which resulted in the best agreement for the different averaging scales that were tested. Observations were first averaged along each of the 15 tracks and subsequently a 10-day boxcar filter was applied with time steps of 5 days. The satellite observations are shown in figure 3.12 as the red curve. It is clear that while there is a clear correlation (0.65) between the observed SSH and the steric changes, there are also substantial differences with discrepancies of more than 10 cm. The differences between the blue and the black curves are small compared to the actual variations and this demonstrate that the steric height anomalies are dominated by the temperature

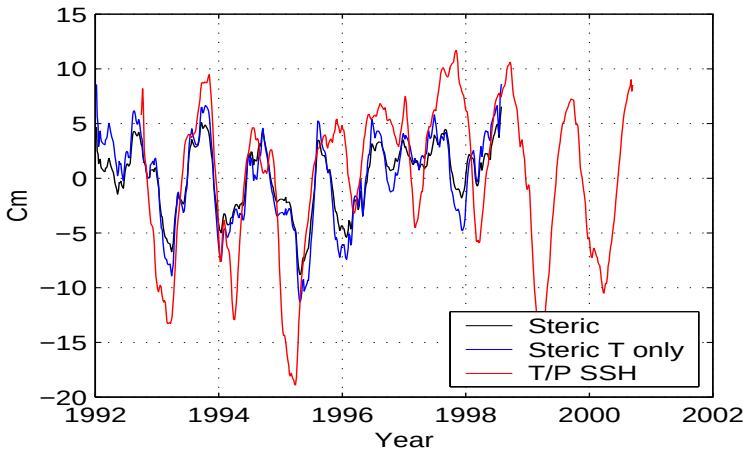

Figure 3.12: Smoothed T/P observations averaged within 150km (red) and steric heights calculated for the upper 700 meters (black). Shown is also steric height anomalies from temperature changes only (blue)

changes. The discrepancies between steric heights and SSH observations cannot be attributed to steric changes in the water deeper than 700 meters and averaging over larger or smaller areas for the T/P observations did not result in smaller discrepancies. It is therefore likely that the differences arise from variability in the bottom pressure at OWSM due to larger scale changes in the strength or meandering of the currents.

3.6.3 Mixed layer deepening from satellites

As a first test of the mixed layer deepening model, a mean annual curve for the years 1992 through 1996 was constructed for: SST, steric height and mixed layer depth. As the assumption about a relationship between heat content and mixed layer depth is obviously violated during 1997, data after 1996 are not used in constructing a mean annual height. Annual and semiannual harmonics were fitted to the SST and steric height anomalies and the daily values used for the mixed layer depth model. As seen in figure 3.13 the mixed layer deepening from the model reproduces the observed MLD well. During the cooling season, the discrepancies are up to 50 meters but the late winter mixed layer depth agrees within 2 meters. The model only works when both the height and the SST temperature are decreasing and this criterion is used to determine the start and end dates. To avoid instability when the SST changes are very close to zero, the model was only run as long as the SST drop was more than $0.004°C/day$. Several values were tested and the selected threshold was the lowest possible before the model turned unstable.

When the input data are the satellite observed SSH and SST, the discrepancies between steric heights and T/P SSH have an effect. The amplitude of the mean annual SSH variation from T/P is about 3-4 cm higher than the steric height amplitude from in situ data whereas the SST variations are very similar. This is also seen in figure 3.12 where the T/P variations are substantially larger than the steric height anomalies for most of the individual years. When harmonic fitting is applied, the annual observations of T/P SSH and AVHRR SST give an estimated mixed layer

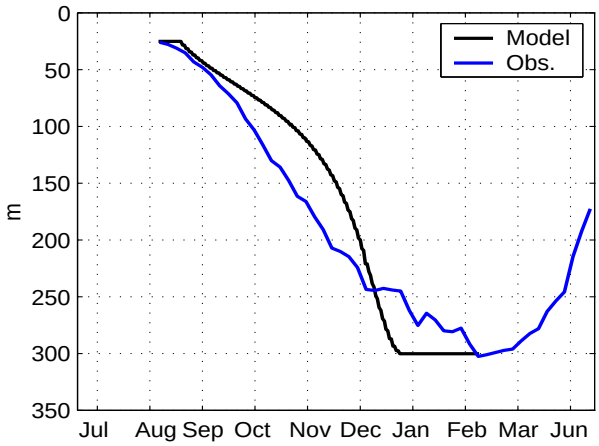

Figure 3.13: Mixed layer deepening (black) estimated from annual mean steric height anomalies and SST from in situ data. Mean annual mixed layer depths from in situ observations are shown in blue.

deepening of 1500 meters as seen in figure 3.14. The late winter mixed layer is

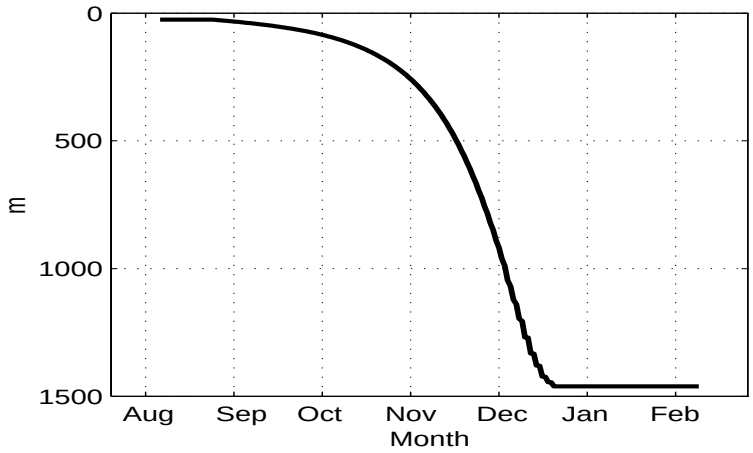

Figure 3.14: Mixed layer deepening estimated with input from T/P (SSH) and AVHRR (SST) satellites

obviously too large and is a consequence of the overestimated heat loss derived from the SSH changes. The variability in the SST observed from satellites is very similar to in situ observations and A very large mixed layer is thus needed to account for the large heat loss during winter.

From the investigation above it is now clear that there is a potential for this method to work. When the steric heights were used instead of SSH variations a very reasonable mixed layer deepening was obtained.

In the derivation of the model it was assumed that the annual SSH changes could be related to changes in the heat content. Apparently, this is not the case at the position of the OWS M where changes in heat content only accounted for about half of the mean annual variation in SSH. The different contributions to the error budget

such as the deep variability, changes in salinity and errors in the measurements can not account for the differences and we therefore conclude that changes in the swift currents associated with the polar front have to play a large role.

In other regions of the North Atlantic, away from fronts and strong currents, a much better agreement between heat changes and SSH changes is expected. With the good in situ results in mind, the mixed layer deepening model will thus be validated at another location.

3.7 Repeated XBT line Ax03

The second test site used for the testing mixed layer deepening model, is the ship of opportunity line from New York to the English Channel. The observations along this line consist mainly of the temperature observations from Expendable Bathythermographs (XBT) with additional observations from CTD casts. The observations from 1990 through 1998 are obtained from the WOCE project (WOCE Data Products Committee, 2000)[3] supplied with data from 1999-2001 (Hamilton 2001, personal communication). Figure 3.15 displays the position of the available XBT observations after 1991 and the number of observations during the different seasons. The line is occupied more frequently during summer than winter but no pronounced north-south seasonality was seen in the positions of observations and the number of observations during winter is probably high enough to construct a mean annual variation.

From the discussion in section 3.2 it is clear that the observations along the AX03 XBT line primarily are located in the water of subtropical origin. The region west of the Midatlantic Ridge is in the Gulf Stream extension characterized by strong fronts and shedding of baroclinic eddies.

East of the Midatlantic Ridge, the XBT observations are in a transition region between the subpolar and subtropical gyres where the currents are much weaker compared to west of the ridge. As described in Pollard et al. (1996) this region is bounded to the south by the Azores current and to the North by the NAC. The location south of the zero wind stress curl line (Leetmaa and Bunker, 1978) and the outcropping of isopycnals during winter means that water is subducted to the south into the main subtropical thermocline (Paillet and Arhan, 1996, Aken, 2001). The favorable conditions for subduction are also seen in figure 3.1 where the region is characterized by large winter mixed layer depths (> 500 m) that decreases to the south and west.

3.7.1 In situ conditions

The quality control of the XBT observations is an important task in order to remove obvious and more subtle errors. The quality control has been carried out according to the procedures described in Bailey et al. (1994) and observations have been used only if they had been classified as "good data" in the quality control (Data Quality Class 1). According to the WOCE project instrumental uncertainties are $0.1°C$ for the temperatures and 1% for the depth observations.

[3]The observations from 1996 on the CD rom was found to be in error and replaced with good data

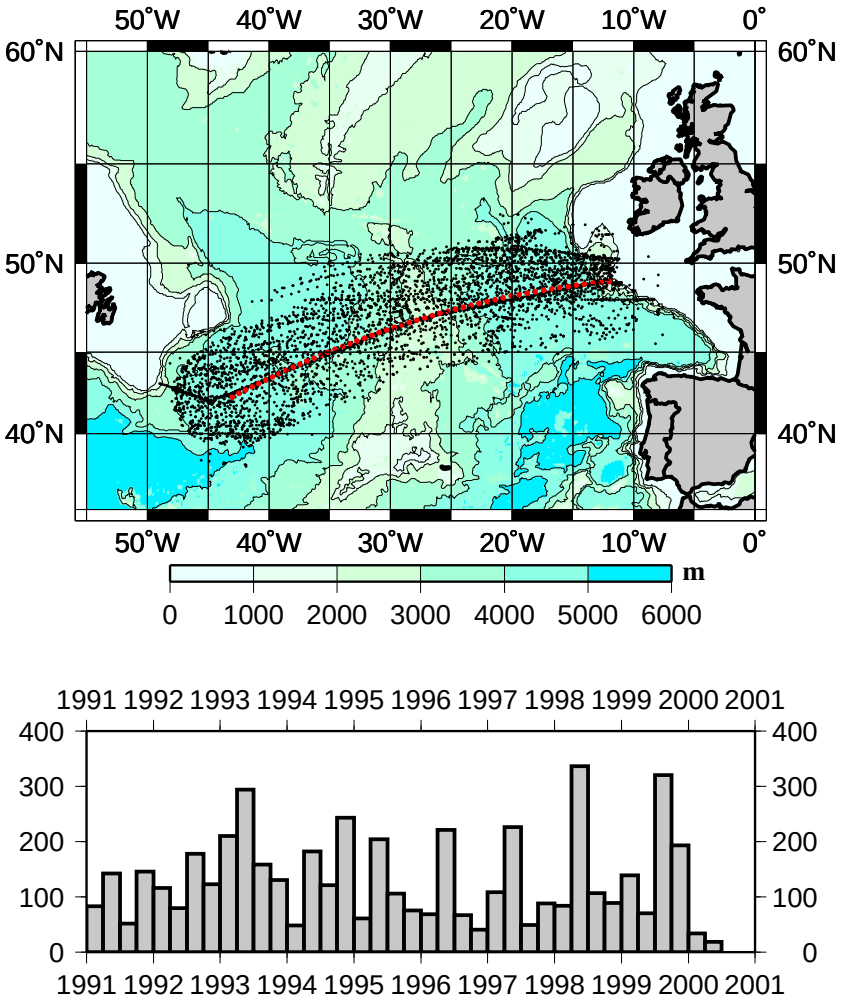

Figure 3.15: Top: Spatial coverage of XBT observations along the AX03 line. The red circles indicate the mean great circle and the colored contours illustrate the depth. Bottom: Number of data per year after the preprocessing

Only profiles deeper than 500 meters with a minimum of 20 observations within the upper 500 meters were used in this study. The profiles were all interpolated to 1 meter depth interval and a steric height anomaly calculated from 500 meters with $\rho_0 = 1030 kg/m^3$ and constant salinity $S = 35$. Bathythermographs are not very good at observing the SST and it was therefore estimated by linear extrapolation of the observations between 5-20 m. As an additional quality check, profiles with variability above 1°C in the upper 20 meters were discarded. In a comparison between the The SSTs obtained with extrapolation and the shallowest observations in the profiles it was clear that the extrapolation method gave more consistent results. Mixed layer depths were therefore estimated using the new SSTs and a potential temperature criteria of $\Delta T = 0.5$°C.

An average annual time series from in situ observations was constructed in every point along the great circle shown with red dots in figure 3.15. Observations within ±250 km and ±5 days were averaged every 5 day throughout a year. Figure 3.16

displays longitude-time diagrams of annual variation of steric height, mixed layer

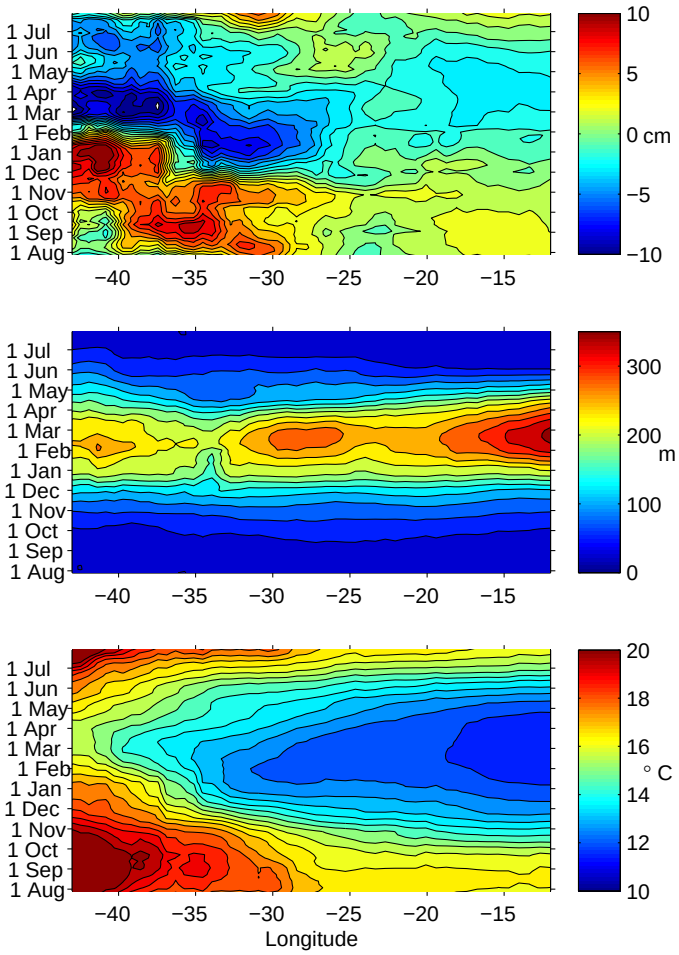

Figure 3.16: a: Longitude-Time plot of a) steric height anomalies in meters, referenced to 500 meters contour interval is 1 cm, b) Mixed layer depths with contour interval of 25 meters and c) Sea surface temperatures, contour interval is 1°C.

depth and SST, all derived from the temperature observations. It is clear from all three plots in the figure two regions exist divided by the the Midatlantic Ridge at around $25 - 30$°W.

West of the ridge, large irregular annual variations are seen in steric heights with summer and winter differences of up to 20 cm. The summer SSTs exceed 17°C and winter mixed layer depths are generally below 250 meters. The conditions are a consequence of the conditions in the Gulf Stream extension and the North Atlantic currents as described in section 3.2.

Currents are much weaker in the region east of the ridge and the steric heights display a more regular annual cycle with amplitudes of $1 - 4$ cm . Mixed layer depths are significantly larger in this region with deepest mixed layers in the east exceeding 350 meters. The horizontal isotherms in figure 3.16 furthermore indicate the absence of fronts in this region. The east–west difference in the strength of the fronts is clear

from the mean SST for the North Atlantic. Whereas the gradient within the 500 km averaging box is only 1-2 degrees in the east, north–south changes of more than 4°C are seen in the west. Enhanced variability to the west and the possible effect of undersampling is also seen in figure 3.17. where the variability in steric heights within the averaging boxes is shown for February and August along the mean great

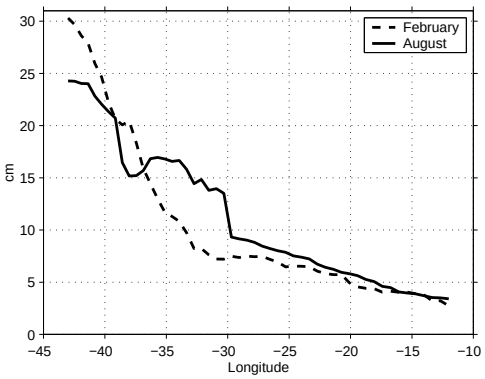

Figure 3.17: Standard deviation of steric heights within $5 \times 5°$ averaging areas along the mean great circle line during February and August.

circle. The standard variability is based upon minimum 40 steric height estimates and show variability up to 25-30 cm west of the Midatlantic Ridge that decreases to less than 10 cm in the eastern region. The variability represents the combined effects of a spatial variation in mean conditions and the meso scale activity within an averaging box. The two months shown here demonstrate that the variability does not depend on the time of the year or the number of observations as the results from August is based upon 3-4 times the observations than from February.

In addition to the stronger gradients within the averaging boxes to the west, figure 3.15 reveal that the ship tracks in the west tend to be more spread out compared to the Eastern part where most ship track converge towards the English Channel. This will reduce the sampling error further in the east compared to the western region of this section.

Most of the XBT probes are designed to measure temperature in the upper 750 meters. The number of profiles are therefore drastically reduced when extending below 800 meter which makes estimates of deep steric variability within a winter very uncertain. Monthly T and S profiles from the WOA98 was therefore used along the section to calculate the steric variability between 500m and 1500m. The standard deviation of total steric steric heights was generally below 0.3 cm except east of 15°W where the variability reached 0.5 cm. The maximum at this location is mainly due to the salinity contribution because this region is influenced by the Mediterranean outflow water, in particular in the Gulf of Biscay where a local cyclonic circulation of salty Mediterranean water exists (Iorga and Lozier, 1999a).

Climatology was also used to estimate steric height changes due to salinity changes in the upper 500 meters. The variability was highest in the western region with up to 2.5 cm and lowest in the east with values below 0.5 cm at 14°W. East of 30°W the standard deviation was below 1 cm.

3.7.2 Satellite signals

The frequent sampling of the T/P satellite is useful to study the SSH variability within the averaging bins and compare with the steric height results in figure 3.17. In every point along the great circle, all observations within 250 km are used to calculate the spatial SSH variability as in the previous section. The results are shown in figure 3.18 as SSH standard deviations for February and August throughout the record and for

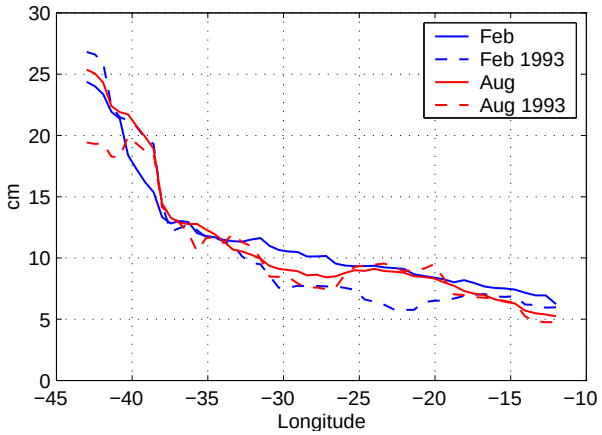

Figure 3.18: Standard deviation of TP SSH within the $5 \times 5°$ averaging areas along the mean great circle line during February (blue) and August (red). The variability for the year 1993 is shown with dashed lines

1993 in particular. The variability from SSH anomalies represents only the meso scale variability but the magnitude and the east-west shape of the variability in February and August resemble the steric height variability. East of 30°W the T/P variability is a few cm higher than the steric height variability. Variability calculated from 1993 observations does not differ much from the mean over all the years, indicating that inter annual differences are insignificant. The picture was consistent when the variability was calculated individually for the other years.

Steric heights calculated from 700 meters were grouped in bins of 0.25° and a mean steric height was calculated and subtracted. The steric anomalies were compared with the T/P observations from ground tracks located in the same bin and within time intervals of $\pm\Delta t$. The results are shown in figure 3.19 for three different time intervals and the correlation between T/P SSH and steric height anomalies is clearly seen in all three plots. When smaller time intervals is allowed between T/P observations and XBT profiles, the number of pairs is reduced from 466 pairs for $\Delta t = 4.5$ days to 18 for $\Delta t = 0.5$day. The agreement improves when the time difference reduces and this is seen as a convergence of the points toward the line with slope 1. Most of the outliers are removed when the time difference is as short as 0.5 days and all errors in the estimates are within 4 cm.

The point wise correlation between T/P and steric heights was calculated for different combinations of bin sizes and time differences. Increasing bin sizes resulted in a lower correlation as well as using steric heights calculated from a reference depth of 500 meters. However, the impact of these changes was smaller than changing the

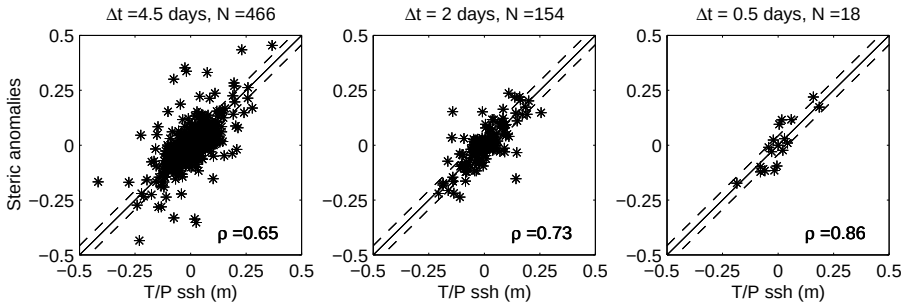

Figure 3.19: T/P SSH observations versus steric height anomalies. The steric height anomalies are calculated with respect to a mean in a 0.25×0.25 bin and only compared with T/P observations within $\pm\Delta t$ days. Solid lines indicate the one to one relationship and the dashed lines indicate deviations of 3 cm from the perfect relationship

time difference between observations which appeared to be the most important factor to obtain high point wise correlation.

An averaging procedure similar to the in situ data was used in the construction of a mean annual cycle for the satellite data. The data coverage is much more uniform but for consistency a 10 day averaging window was applied every 5 days. A 500 km averaging box included 4-6 T/P satellite ground tracks with 200-300 observations every 9.92 days. The daily 9×9 km AVHRR observations were averaged into 0.5° boxes every 5 days to reduce the gaps from clouds and subsequently averaged within 250 km from the great circle as for the other data.

The averaged annual variations in satellite observed SSH and SST along the AX03 line are shown in figure 3.20. The SST variations resembles the SSTs obtained from XBT data (see figure 3.16) whereas the T/P SSH variations are more regular than in situ steric heights. The east–west difference in amplitude is recognized in the SSH plot, but the winter SSH change of $\simeq$ 17 cm in the West is smaller than the steric heights whereas the $\simeq$ 6 cm drop in the east is higher. The T/P SSH minimum occur in March-April almost everywhere along the section. This is in agreement with steric height changes in the eastern region whereas the minimum to the west is as early as February at some locations.

The winter drop in SST of 10-12°C with a minimum in late March is similar in magnitude to the XBT results, but a discrepancy in the time of minimum SST is seen again in the region to the west where in situ data precedes the satellite observations with up to 2 months.

3.7.3 Estimation of mixed layer deepening

The mean annual variations in steric heights and extrapolated SST, both derived from the in situ data, were used as input parameters to the mixed layer deepening model. Similar to the model in section 3.5, harmonic fitting was applied to the smoothed SSH and SST input data and the model was only run for the time period during winter when both SST and SSH were decreasing. The threshold for SST changes was set to -0.004°C/day and the initial input mixed layer depth 30 meters. The mixed layer deepening results for every point along the mean great circle are shown in the

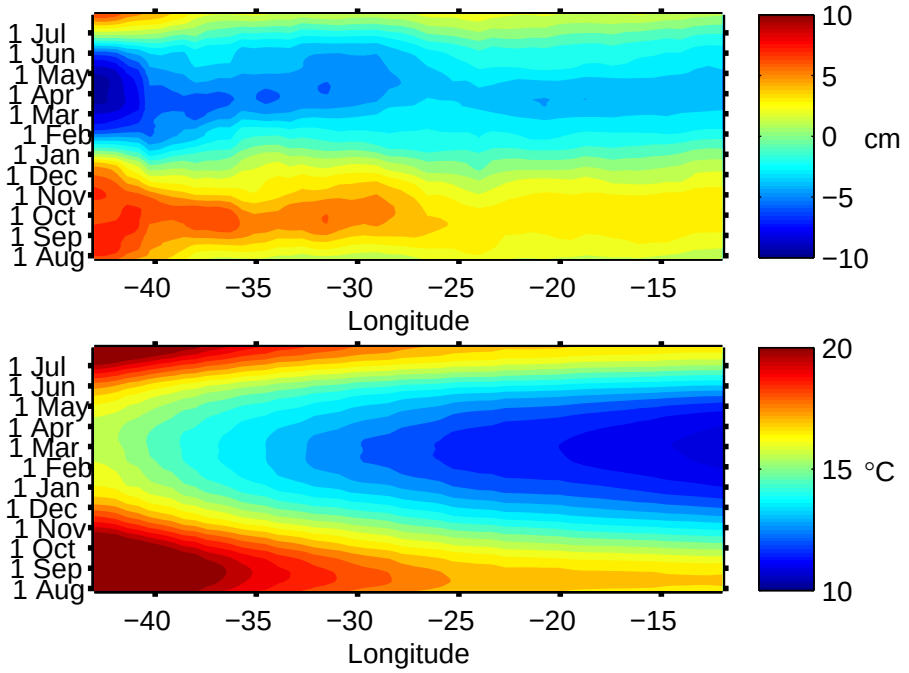

Figure 3.20: Longitude-time plot of annual mean SSH variation from T/P (top) and annual SST from AVHRR satellites (bottom) along the AX03 mean great circle. Contour intervals are 1 cm and 0.5°C.

longitude–time diagram in figure 3.21.

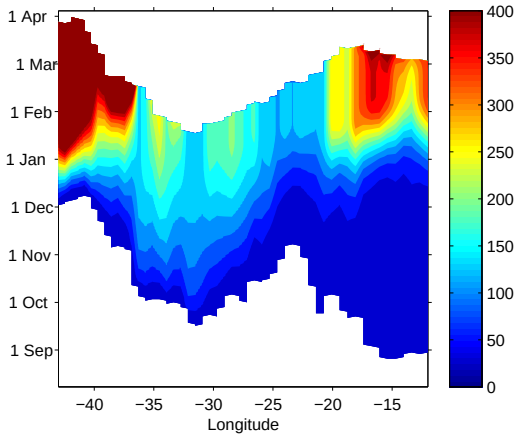

Figure 3.21: Mean annual mixed layer deepening estimated from steric height anomalies and SST from in situ observations. The contour interval is 25 meters.

The figure can be divided into three regions: East, west and in between. East of 20°W the mixed layer deepening starts in September-October, experiences a rapid deepening in January and ends with a maximum mixed layer depth in late February of 200-350 meters. Between 20-37°W the mixed layer starts deepening in October and deepens slowly with winter maximum mixed layer depth of 100-175m which is

reached in February. The mixed layer deepening in the region west of 37° begins very late, in November or December, and reaches end mixed layer depths of more than 1000 meters in a few locations (Note the colorbar saturates at 400m).

In a comparison with the mixed layer depths in figure 3.16, it is clear that the eastern region has the largest resemblance to the actual conditions. The beginning of mixed layer deepening in September-October and maximum mixed layer depths in March are in good agreement with the observations. The end mixed layer depths are within 100 meters of the observed, but the structure with deepest mixed layer at the eastern boundary is not reproduced.

The mixed layer depths in the middle region are underestimated with up to 150 meters around $20 - 25$°W. The deepening begins too late and terminates too early, especially around 35°W where the end mixed layer is reached in January, compared to medio February from observations.

In the westernmost part of the section, the deepening begins very late, in November and December and within 1 or 2 months, mixed layer depths of 400m are reached and end mixed layer depths of more than 1000 meters are found. This behavior is obviously not supported by the observations in figure 3.16 where maximum mixed layer depths are on the order 250m.

The next step is to use the satellite observed mean annual cycles of SSH and SST as shown in figure 3.20 as input to the mixed layer deepening model. The model configuration was the same as with the in situ data described above and the estimated mixed layer deepening is shown in figure 3.22 The starting dates in October and end

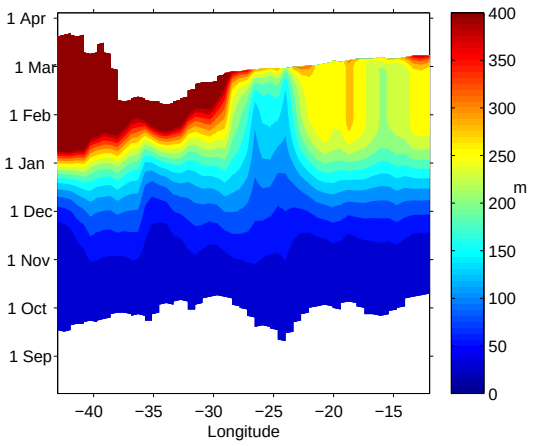

Figure 3.22: Mean annual mixed layer deepening estimated from steric height anomalies and SST from in situ observations.

dates in March are consistent along the section and corresponds to the observed deepening season. Late winter mixed layer depths in the east of 250-300 meters agree with the observations but the maximum towards the eastern boundary is not reproduced. The shallow mixed layers around 25°W in January and February of < 100 m are not supported by the observations in figure 3.16 where mld are around 175 m. The end mixed layer depths in the western part of the section resemble the results from in situ observations with depths of > 1000 m.

In general, the annual amplitude in SST from in situ and satellite observations does not vary much from east to west along the section and the east–west structure of the mixed layer deepening is therefore a consequence of the variations in SSH or steric height amplitudes. The very deep mixed layers west of the Midatlantic Ridge results from from large amplitudes in SSH and steric height on the order of 10 cm whereas the end mixed layers of 100 meters in the middle part result from amplitudes as low as 1-2 cm. The region east of the Midatlantic ridge show amplitudes of 2-3 cm for both the steric heights and SSH giving rise to mixed layer depths of 250-350 meters.

3.8 Discussion

The sensitivity of the model to changes in input parameters is important for determining the cause of the discrepancies. The fitting of curves to the observed data is a crucial but necessary task. In section 3.5, the harmonic fitting procedure was shown to be superior to the fitting of polynomial when noise was added and this was also seen when the real data were used as input. A running mean applied to the SSH and SST changes before the harmonics were fitted did not influence the phase and amplitudes significantly. However, the robustness of the harmonic fitting method can also be a weak point, because the annual and semiannual harmonics do not allow for reproducing all details in the steric height changes. This was illustrated by the idealized model in section 3.5 where the perfect input data gave an underestimation of about 50 meters when the harmonic fitting was applied.

The annual cycle in SSH often lags the SST cycle and the minimum in SST is therefore reached before the minimum in SSH. Due to instability for very small SST changes, the threshold on the SST changes is necessary in the very end of the time series but it only affects the very last points where the deepening is unrealistically high.

Vertical diffusion at the base of the mixed layer based upon climatological temperature gradients was applied. The export of heat of out the mixed layer with a diffusion coefficient of $1 * 10 - 4$ typically reduced the end mixed layer depths 5-10 meters. Another small effect was seen when a constant salinity of 35 was used instead of the spatially varying salinity. The difference between the two methods was less than 2 meters in the end mixed layer depths.

OWSM

From the in situ conditions at the OSWM it is clear that some of the assumptions which has been made in the derivation of the model do not apply at this position. The most important violation of the assumptions is the neglection of the bottom pressure term in the seasonal SSH budget in equation 3.2. The term gives rise to large discrepancies between amplitudes of steric heights and T/P SSH, hence the estimated mixed layer deepening is far too large.

The contamination from barotropic processes is avoided by using the steric heights anomalies instead of actual observed SSH changes. When observations from before 1997 are used, the winter mixed layer depth estimation is within 5 meters of the observed. The temperatures during 1997 at 200-500 meters depth are uncorrelated with SST and show a maximum during winter. Such a deep variation indicates that

neglecting advection of heat in equation 3.1 is not justified during this period. The observed signal may be related to changes in the large scale atmospheric conditions where the NAO index experienced a dramatic drop during the winter 1995/1996 (Esselborn and Eden, 2001). NAO is related to North Atlantic conditions, and 1 year lag from the North Atlantic (Faroe–Shetland ridge) to the OWSM is in good agreement with the advective time scale in Furevik (2000).

To conclude, the results from the OWSM are dominated by the oceanographic conditions at the position with rapid currents and meso scale activity. The temporal and vertical sampling of in situ temperature allow for determining the main error sources and mean annual mixed layer deepening is well reproduced when these errors are disregarded.

AX03

The conditions along the XBT line Ax03 show significant variability from the west towards east. The existence of a front and the elevated variability west of the Midatlantic Ridge have a large influence on the results. From the comparison between altimetry observations and steric height anomalies it was evident that a good correlation could be obtained if the observations were close in space and time. The most important parameter to obtain a high correlation was the difference in time between the two observations. This indicates that baroclinic processes, such as eddies, with time scales of a few days dominate the SSH and upper temperature fluctuations.

The largest influence from eddies is seen west of the ridge and averages in boxes can thus be influenced by effects of undersampling. The errors associated with the spatial and temporal averaging are not neglegible in this region which is clear from the irregular annual cycle in steric heights. Undersampling is not an issue with the temporal and spatial sampling of the satellites resulting in a regular annual SSH cycle. The T/P SSH amplitudes of $\sim$ 10 cm are similar to the steric height amplitudes but the drop during winter does not correspond to a change in local heat content during winter, indicated by steric height anomalies from WOA98 with an annual amplitude of 5-7 cm in this region. The discrepancy between climatology and average in situ steric heights probably arise from an overestimated in situ steric height due to undersampling errors.

East of the Midatlantic Ridge, in situ observations indicate favorable conditions for this study with good agreement between steric height changes and observed T/P SSH variability. The weak circulation in this region and the absence of fronts minimize the errors from undersampling in the in situ data. Thus, mixed layer deepening from both satellite observations and in situ observations give acceptable results that are within the expected errors. An error source in this region is salinity variations at middepth due to fluctuations in a local recirculation of Mediterranean water in the Bay of Biscay. According to climatology, the deep steric effect from this variability is up to 1-2 cm with highest values at the eastern boundary and with a maximum during winter. This counteracting effect may thus explain why the observed maximum in late winter mixed layers depths around 10°W is not reproduced in any of the two model estimates.

The main conclusion to be drawn from this study is that the estimation of the mixed layer deepening from satellite observed SSH and SST works under favorable

conditions in areas with weak currents, low meso scale variability, small fluctuations in bottom pressure and small spatial changes in the mean conditions. However, these requirements put a serious limitation to the sites around the global oceans useful for this method. In regions away from strong currents, the major error source appears to be fluctuations in the bottom pressure. This contribution can be reduced by averaging over large areas but the spatial variation in the mixed layer puts a limit to how large averaging boxes can be and still give a reasonable result. The limit chosen here of $5 \times 5^{\circ}$ averaging scales was apparently only valid east of the Midatlantic Ridge.

4

Improved description of sea level in the North Sea

4.1 Motivation

The histories in the countries around the North Sea report on exceptionally high sea level due to severe meteorological forcing back to 9 A. D. (Gill, 1982). These storm surges and the associated flooding have claimed many victims. An example from recent times is the surge on 31 Jan. 1953 where large areas were flooded in Britain and Holland and 2000 people drowned. The description and prediction of the sea level in the North Sea is therefore important to minimize the risk of flooding of the low lying and heavily populated countries around the North Sea.

The sea level variability in the North Sea is dominated by tides where the M_2 constituent reach amplitudes of 110 cm at some positions on the English east coast. The tidal sea level variations, which have been studied extensively for many years, are now well known and can be predicted with good accuracy (see e.g. Pugh, 1987, Andersen, 1999). The problems arise when surges with sea level variations on the order of meters amplify the tidal variability. As these surges are generated by atmospheric fluctuations they depend upon the performance of the weather forecasts and are therefore difficult to predict in the same way as with the tides (Heaps, 1983). Most of the countries around the North Sea run operational numerical models to predict storm surges (Flather, 2000). The models typically predict the sea level at the Danish west coast within $\sim$ 20 cm but occasionally, errors exceed 100 cm during some storm surges (Nielsen and Nielsen, 2000, Nielsen, 2001b). None of these models use any information from remote sensing satellite observations and only a few include information from tide gauge observations in the models. In addition, several models (e.g. the Danish and Norwegian) have open boundaries in the northern North Sea where no information about external surges is introduced.

In this study I will demonstrate that the satellite and tide gauge observations not included in the models contain much information about processes and sea level in all the North Sea. The processes of internal and external surges will be investigated with both satellite and in situ data and the two types of data will be combined in a real time description of the sea level in the North Sea with errors of the same size as the numerical models. The outcome of this study may serve as preliminary investigation towards implementing tide gauge and satellite observations in the models or it can serve as an independent tool towards which the model performances can be validated over all the North Sea. regardless of the purpose, the synergistic effect from the combination of satellite with in situ data will be demonstrated here.

The tidal sea level variations in the North Sea will be considered as known and focus will be on the sea level variability from surges generated by fluctuations in

the atmospheric conditions. The outline of this chapter is as following: A general introduction to the mean conditions in the North Sea and to the theory for the propagation of the surges will be given in section 4.2. Section 4.3 focus upon the time scales and the propagation of the signals as seen by the coastal water level recorders and section 4.4 estimates the spatial scales of the same processes from altimetry observation. The agreement between coastal observations and satellite observations from the interior (section 4.5) leads to the formulation of a multivariate regression model in section 4.6 that combines the two types of observations. Observations from the independent ERS satellites are used in section 4.7 to assess the performance of this model compared to using only one type of data.

4.2 Introduction to North Sea

The North Sea is a marginal sea to the North Atlantic located on the Northwestern European continental shelf. The bathymetry is shown in figure 4.1 and except for the the Norwegian trench where depths exceed 700 meters, the North Sea is a shallow sea with depths of 30-150 meters that is shallowing to the south-east. The mean circulation is cyclonic with a transport of 1 Sv (1 Sv $= 1 * 10^6 cm^3/s$) and a mean flushing time of 650 days (Furnes, 1980, Kauker and Storch, 2000). It is fed by inflow of salty water in the Fair Isle current between Orkney and Shetland islands, in the East Shetland Atlantic Inflow and along the western side of the Norwegian trench (Turrell et al., 1996, Holt et al., 2001). The mean surface salinity of the North Sea reveals an inflow of low salinity water from the Baltic Sea through the Danish Straits and in the German bight from the large German rivers (Holt and James, 2001). Outflow takes place primarily on the eastern side of the Norwegian trench and in the Norwegian coastal current. A detailed description of the mean temperature, salinity and currents will not be given here. More attention will instead be given to the description of the sea level variability as this is of primary interest to this study.

The nontidal sea level variability in the North Sea is dominated by surges that are typically generated by winds and atmospheric pressure changes related to low pressure systems. The surges can be divided into two kinds: External or internal surges. The former is generated by traveling low pressure systems North and Northwest of Scotland whereas the latter is generated by winds acting within the North Sea (Pugh, 1987).

The theory of externally generated surges begins with the unforced shallow water equations with a boundary parallel to the x-axis (see e.g. Gill, 1982). The boundary dictates that the v velocity must vanish and the momentum equations are

$$\frac{\partial u}{\partial t} = -g\frac{\partial \eta}{\partial x} \tag{4.1}$$

$$fu = -g\frac{\partial \eta}{\partial y} \tag{4.2}$$

where η is the sea level anomaly. The continuity equation becomes

$$\frac{\partial \eta}{\partial t} + H\frac{\partial u}{\partial x} = 0 \tag{4.3}$$

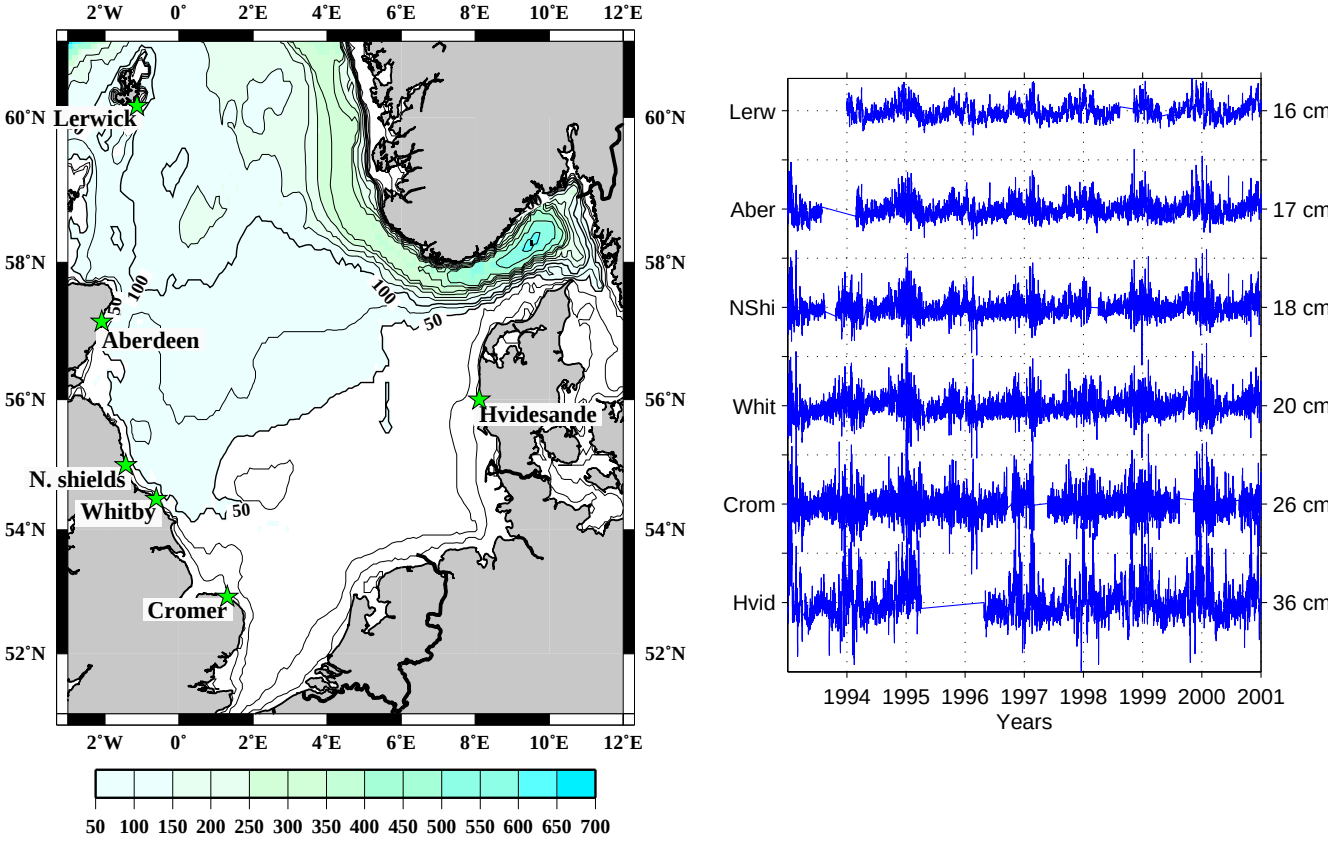

Figure 4.1: a: Bathymetry in the North Sea. The 6 water level recorders used for this study are indicated with the green stars. b: Detided sea level time series from the six water level recorders indicated in a. Standard deviations of the time series are indicated to the right of the time series

where H is the water depth.

The solution to equation 4.1 and 4.3 is a sum of two waves traveling in opposite directions parallel to the x axis

$$\eta = F(x + ct, y) + G(x - ct, y) \tag{4.4}$$

where F and G are two functions to be determined and $c = \sqrt{gH}$ is the propagation velocity of the waves. When the solutions in equation 4.4 are substituted into equation 4.2 it is clear that for $f > 0$, the only solution that decays away from the boundary is the solution represented by the G function, traveling in the positive x-direction. If G is a sinusoid the solution takes the form

$$\eta = \eta_0 e^{-y/a} cos(kx - \omega t) \tag{4.5}$$

where η_0 is the maximum amplitude at the coast, k is the wavenumber and $a = c/f$ is the barotropic Rossby radius. The waves described in equation **??** are called Kelvin waves and are nondispersive with dispersion relation

$$\omega = kc \tag{4.6}$$

The velocity can be shown to be

$$u = \sqrt{\frac{g}{H}}\eta_0 e^{-y/a} cos(kx - \omega t) \tag{4.7}$$

From the equations above, it is now clear that the Kelvin wave travels with $c = \sqrt{gH}$ only in the direction with the coast on the right hand side when looking in the direction of the propagation. In the North Sea it corresponds to a cyclonic propagation from Scotland towards Denmark. Equation 4.5 also shows that the spatial scale of the surge away from the coast is on the order of one Rossby radius which is 320 km for 150 m depth and 180 km for 50 m depth.

Internal surges are generated by winds within the North Sea that generate elevated sea level by two mechanisms: Ekman transport to the right of the wind and alongshore geostrophic current. The Ekman transport is set up when a wind W exerts a drag on the sea surface of

$$\tau_s = C_D \rho_a W^2 \tag{4.8}$$

where C_D is a dimensionless drag coefficient and ρ_a is the density of the air. In the ideal steady state case where bottom friction and pressure gradients can be neglected there exist a balance between the Coriolis force and the wind stress which create an integrated transport of

$$V_E k = -\frac{\tau}{\rho f} \tag{4.9}$$

Where τ is the windstress in the x direction and ρ is the constant density. From the minus sign in equation 4.9 it is evident that the Ekman transport is 90 degrees to the right of the wind stress in the northern hemisphere. In the presence of a shoreline such as the British east coast it is thus clear that winds from the North will pile up water on the coast due to the Ekman transport. More realistic conditions result in an angle less than 90 degrees but the transport is always to the right in the Northern hemisphere.

The elevated sea level on the coast due to the Ekman transport creates a pressure gradient away from the coast which leads to a geostrophic transport along the coast in the direction of the wind of

$$u = \frac{\tau t}{\rho H} \tag{4.10}$$

The associated sea level gradient is

$$\frac{\partial \eta}{\partial y} = -\frac{fu}{g} \tag{4.11}$$

In the absence of friction we thus have a steady increase in the u velocity with time but eventually bottom friction will limit the current as it gets large enough. Equations 4.10 and 4.11 also show that the velocity and associated sea level change are inversely proportional to the water depth D thus giving the largest effect in shallow waters like e.g the southern North Sea.

If variations are allowed in the alongshore windstress, the internal surge will propagate along the coast. The solutions to the equations resembles the Kelvin wave

solution where forcing has been added. They take the form

$$\eta = A(x,t)e^{-y/a} \tag{4.12}$$

Where the amplitude A has to be determined for a specific wind stress. The Kelvin wave solution can be shown to be a special case of equation 4.12 for no wind stress.

The operational model that will be used here for comparison with the predicted sea level, is the storm surge model from the Danish Meteorological Institute that covers the North Sea, the Baltic Sea and the connecting Danish waters (Nielsen, 2001a). The performance of the model is documented in yearly reports where the model is validated against 39 tide gauges (For validation, see Nielsen and Nielsen, 2000, Nielsen, 2001b). About 10 of the tide gauges are located on the west coast of Jutland in the North Sea and the mean RMS errors in predicting the sea level ranged from 13 to 24 cm. In terms of explained variance, the model performance varied from 55 to 92%.

The model performance at the Hvide Sande recorder is particularly interesting to this study because the observations are is also used in this investigation. During year 2000, the RMS errors were $\sim$ 18 cm and the model explained about 85% of the variance in the tide gauge observations. Included in this statistic is a maximal prediction error of 115 cm during year 2000. The performance in 1999 resembles the 2000 results except for the maximum error at Hvide Sande which was as high as 173 cm during the hurricane 3-4 December 1999.

4.3 Water level recorders

The water level data from the east coast of the United Kingdom have been obtained from the British Oceanographic Data Centre[1] as quality controlled hourly values of sea surface elevation. The hourly observations from Hvide Sande at the Danish west coast are from the outer water level recorder, quality controlled and provided by Kystdirektoratet[2] in Denmark. As seen in figure 4.1b the data return is good for most of the records. Exceptions are: Lerwick (no data are available before 1994), Aberdeen (210 days gap in late 1993, beginning of 1994) and Hvide Sande (1 year of missing data 1995-1996).

Detiding

In a power spectral analysis of the water level recorder data, it is evident that besides the usual tidal constituents like M_2 and S_2, additional shallow water tidal constituents like M_4 and MS_4 can be found. The constituents exist because the nonlinear terms describing advection $\vec{v}\cdot\nabla\vec{v}$ and bottom friction $\tau|v|\vec{v}$ are not negligible in the shallow waters momentum equation

$$\frac{\partial\vec{v}}{\partial t} + \vec{v}\cdot\nabla\vec{v} = -\vec{g}\nabla\eta - \vec{g}\vec{k} - f\vec{k}\times\vec{v} - \tau|v|\vec{v} \tag{4.13}$$

The magnitude of the shallow water constituents is therefore dependent on the water depth and the amplitudes increase to the south in the North Sea. According to

[1] http://www.bodc.ac.uk/
[2] http://www.kyst.dk/

Andersen (1999) the largest shallow water constituents are the quarter diurnal M_4 with an amplitude of 2-8 cm off the English and Dutch coast and the MS_4 which has amplitudes below 2 cm everywhere except in the southernmost part of the North Sea.

The detiding method used in this study is the response method developed by Munk and Cartwright (1966). The method assumes a spectral relationship between the constituents within a tidal band (e.g. diurnal or semidiurnal) and does not fit the individual constituents. For the ERS satellites it can be an advantage to infer the K_1 and P_1 amplitudes from the spectral relationship instead of direct fitting. With aliasing period of 365.25 days for these two constituents (chapter 1) non tidal signals evidently will contaminate the results. Studies have shown the response method to work well with T/P altimetry and perform similar to the harmonic analysis method even though fewer parameters are estimated (Andersen, 1995, Ma et al., 1994). However, as the response method deals with the linear response of the ocean to the gravitational tidal forces, it does not work well in estimating the shallow water constituents and these must be removed with other methods. A thorough description of the response filter method is not given here because the detiding method is used as a tool here to remove unwanted signals. Suffice to say the response method was used for the semi diurnal and diurnal bands to remove ~ 100 linear tidal constituents. For further studies on this method, the reader is referred to Munk and Cartwright (1966).

In addition to the response method, the largest shallow water constituent, M_4 was removed by harmonic least squares fitting. The contribution from the remaining shallow water constituents like MS_4,M_6 and MNS_4 is probably < 5 cm where the MS_4 term accounts for most of this variability.

The detided in situ sea level signals are displayed in figure 4.1 together with the sea level standard deviations to the right of the signals. The variability of the residuals represent reductions in the original signals of 100 and 111 cm at Cromer and Whitby, respectively, whereas the Hvide Sande variability is only reduced by 10 cm by the detiding. Fourier analysis of the residual time series revealed that not all the shallow water constituent were removed but the spectral energy in these constituents was small and did not play a significant role in the sea level variability. The figure also reveals that the remaining signal in the observations are characterized by rapid fluctuations that increase counterclockwise around the North Sea with a minimum in SSH standard deviations of 16 cm at Lerwick and a maximum of 34 cm at Hvide Sande. The SSH variability does not arise from the annual steric height because it is overshadowed by the rapid fluctuations. An annual signal is, however seen in the variability which has a maximum during winter and minimum during summer

The characteristic time scales of the coastal sea level signals are shown in figure 4.2a where the autocorrelations are shown for the 6 water level recorders. The observations used to construct the results were selected to avoid the largest data gaps and subsequently interpolated to 1 hour intervals. The number of observations in each water level record were thus reduced, but the shortest record contained about 3.5 years of data or 30000 observations, making the results very robust. The short time scales of the weather induced variability are clearly seen in all the records in figure 4.2 where the shortest time scale of 10 hour is found in North Shields and the longest are found for Lerwick and Hvide Sande with 50-60 hours. The longer timescales at

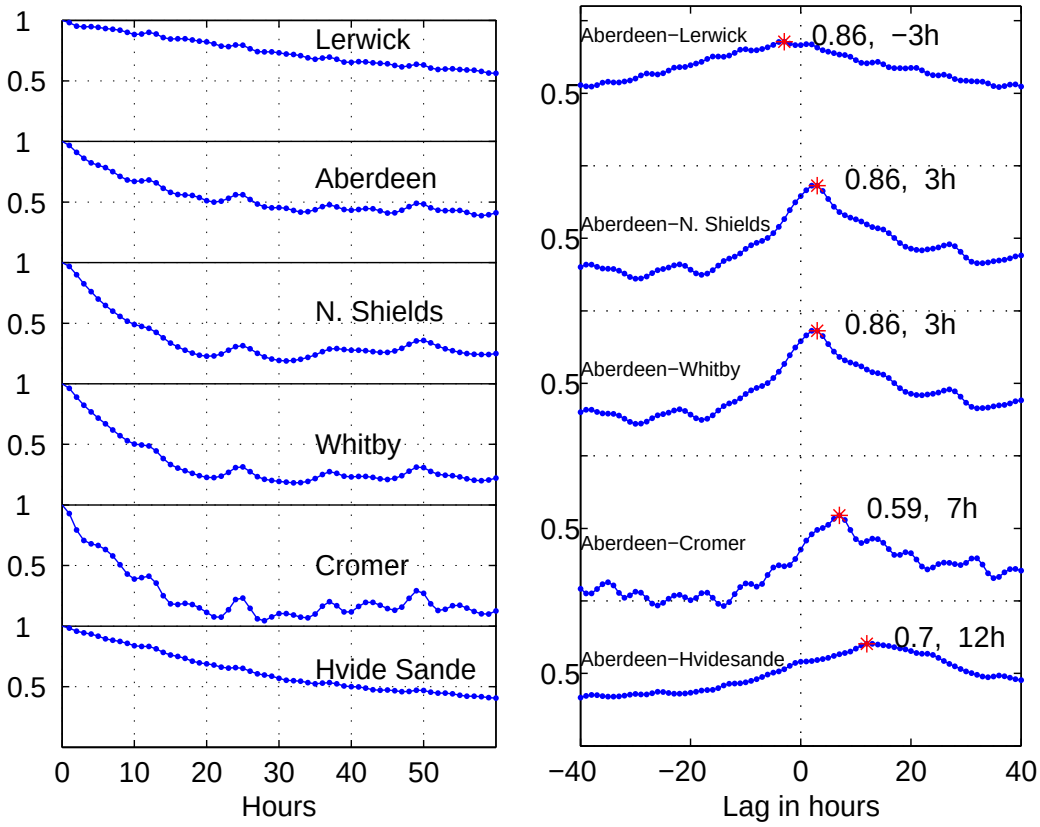

Figure 4.2: Left: Autocorrelation for the 6 water level recorders. Right: Crosscorrelation of the 5 water level recorders with the Aberdeen recorder. The numbers list the maximum correlation and the time lag which is also indicated by the red asterisk.

Lerwick were expected, as this is the record which is most influenced by deep open ocean processes with longer timescales. The other water level recorders on the British coast are more protected and feel only the influence from the North Atlantic through the external surges that propagate rapidly down the coast within 10 hours. The long timescales of the fluctuations at the Hvide Sande recorder indicate that the surges decay in this region probably due to large bottom friction. This hypothesis is corroborated by the DMI model where the southeastern region of the North Sea displays high bottom friction (Nielsen, 2001a).

Tidal residuals are seen in some of the records as an increase in the autocorrelation after 12 and 24 hours. This is most clear at Cromer where a quarter-diurnal constituent is seen but the tidal influence does not alter the results.

Counterclockwise propagation of the surges around the North Sea was predicted by the Kelvin wave theory in equation 4.5 and this is supported by the crosscorrelations in figure 4.2b. The results shown in the figure are calculated from the time series used for the autocorrelations and are based upon minimum 16000 observations in each record. All the coastal water level recorders are highly correlated with a maximum lag that corresponds to the distance between the recorders. A correlation of 0.7 between

the Aberdeen and the Hvide Sande water level recorder indicate the importance of externally generated surges. The propagation speed of the anomalies ranges from 80-112 km/h when the lag of maximum correlation and the shortest distance between adjacent recorders is used. The accuracy on the velocity is limited by the time step of one hour in observations and the distances may be to low but the values agree well with the values for the barotropic surges of $c = 114$ km/h for a water depth of 100 meters as discussed in section 4.2. Residual tidal signals are seen again in the Aberdeen vs Cromer correlation but the lag of max correlation can not be shifted more than 1-2 hours from this effect.

4.4 Altimetry results

The altimetry data used for this study are the TOPEX/POSEIDON version 8.4noib and the ERS version 5.0 noib as described in chapter 1. Tides have not been removed and the inverse barometer effect is included to be consistent with the water level recorders where the effect is also present. The enhanced variability due to the inverse barometer effect was examined with the T/P data and found to be highest in the north ($3-7$ cm north of 60°N) and lowest towards the south (< 4 cm south of 55°N). The study region for the altimetry is chosen to be the region within $2-9°W$ and $52-61°N$ and this is the region that will be referred to as the North Sea in the following.

The removal of tidal signals in the altimetry data was done using the same response filter method as for the water level recorders. The constituents were estimated in every point along the ground tracks and subsequently subtracted from the observations. The tidal subtraction is expected to perform better for the T/P than ERS data due to the limited number of ERS observations. To ensure a reliable tidal subtraction, results were only used from locations where more than 200 T/P observations or 50 ERS observations were available. Furthermore, a 3-standard deviation filter was applied to the time series after the tidal subtraction to remove outliers.

The standard deviation of the T/P detided observations was calculated in every point along the tracks and the values were gridded with decorrelation scales of 200 km and a noise level of 0.02 cm. The results are shown in figure 4.3 and it is evident that the shallow waters towards the south-east are associated with elevated SSH variability. The increase in variability towards the German Bight in the south-west is in agreement with the water level recorders from figure 4.1b but the satellite variability is 5-10 cm lower than the coastal observations. The discrepancy in the SSH variability arise from smoothing in the gridding and because the satellite observations do not extend all the way to the coast where the variability typically has maximum.

It is clear that repeat periods of 10 and 35 days for the T/P and ERS satellites, respectively, are too long to resolve the weather induced signals with time scales of 10-60 hours. The advantage of the satellite observations is the spatial sampling covering all the North Sea with an along track resolution of 6 km. The satellite velocity is 6 km/s and the T/P observations represent 300 snapshots of the sea surface height in every track. The statistical SSH variations of the surges are thus contained in the observations and it is possible to estimate the spatial scales of the fluctuations with statistical methods.

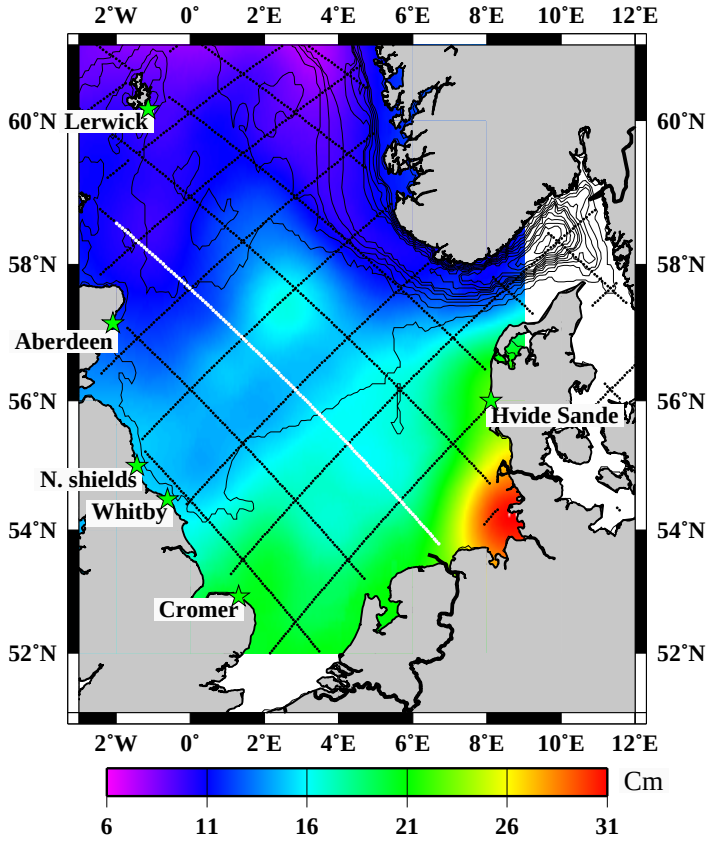

Figure 4.3: Gridded standard deviation of SSH from the detided TOPEX/POSEIDON observations in colors. The bathymetry is contoured with intervals of 50 meters and the satellite ground tracks are overlaid in black. The white ground track indicates where EOF results are calculated along in figure 4.4.

T/P observations were ordered along every track in a time-distance matrix F where missing observations were filled by interpolation. The data set was reduced by applying an Empirical Orthogonal Functions (EOF) method to the matrix. The reader is referred to Emery and Thomson (1998), Høyer (1999) for a description on the method. For this study it is only important to know that the method divides the original N observations in time at P locations into P modes which each have maximized variance and are orthogonal to each other. Each mode is associated with a spatial eigenvector $\vec{e}_j$ and a temporal principal component $\vec{a}_j$ and the original $N \times P$ data matrix F can be reconstructed by

$$F = \sum_{j=1}^{P} \vec{a}_j \vec{e}_j \tag{4.14}$$

The advantage of the EOF method is that the sum in equation 4.14 can be truncated at a low number without great loss of information. The EOF results for one T/P track running northwest-southeast are shown in figure 4.4 where the spatial variation in the first three eigenvectors are shown. Mode 1,2 and 3 explain 73, 14 and 5 percent of the

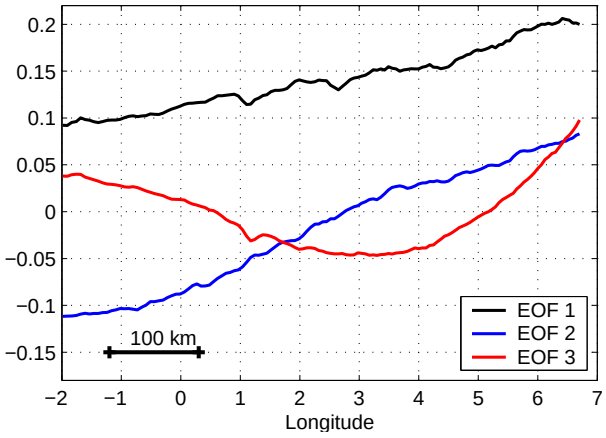

Figure 4.4: Eigenvectors for the first three EOF modes along the T/P track shown in white in figure 4.3. Total variance explained by the three modes is 92 %

original variance, respectively, which is 92 percent in total. The principal components that account for the temporal development of the three modes are not shown here. They display the 10 days observations to be uncorrelated fluctuations as expected from the short time scales of the fluctuations in figure 4.2. The influence from residual tidal signals in the T/P observations was examined with a power spectral analysis applied to the altimetry time series in every point. No significant peaks at the tidal aliasing frequencies from table 1.2 were revealed by this analysis.

The first mode in the figure does not change sign across the North Sea, which means that 73 percent of the variance can be explained by increasing or decreasing the sea level in all the North Sea, with largest amplitude in the south. Modes 2 and 3 changes sign across the North Sea with largest amplitudes towards the coast and resembles the sea surface variations associated with surges as described in section 4.2. The distance from the coast to where the amplitude changes sign is about 100-300 km for these two modes. The spatial scales agree well with decay scale of the Kelvin waves which is the Rossby radius. Examination of the EOF results from the other tracks reveals that the spatial variation of the EOF modes in figure 4.4 is representative for the North Sea. The spatial scales of sea surface height variations in the North Sea is thus on the order of several hundred kilometers and a significant fraction of the variability probably arise from the Kelvin waves that were also found in the water level recorders.

4.5 Pointwise correlation

In a combination of the satellite and in situ observations it is a requirement for a good performance that the T/P observations are correlated with the water level recorders within some distance from the recorders. The individual water level recorders were correlated with the satellite measurements in every T/P observation point along the ground track to determine the magnitude and spatial structure of the correlation.

The pointwise correlation between the T/P and water level recorders was calcu-

lated by subsampling the water level time series to the times where T/P observations were available. The subsampled observations were chosen as the in situ averages within 3 hours from the satellite observations. Different averaging intervals were tested and ±3 hours gave the highest correlations.

The results for the T/P satellite are shown in figure 4.5 for the Aberdeen, Cromer and Hvide Sande water level recorder for points where more than 150 pairs of observations were available. The figure shows that very high correlation (> 0.9) is obtained

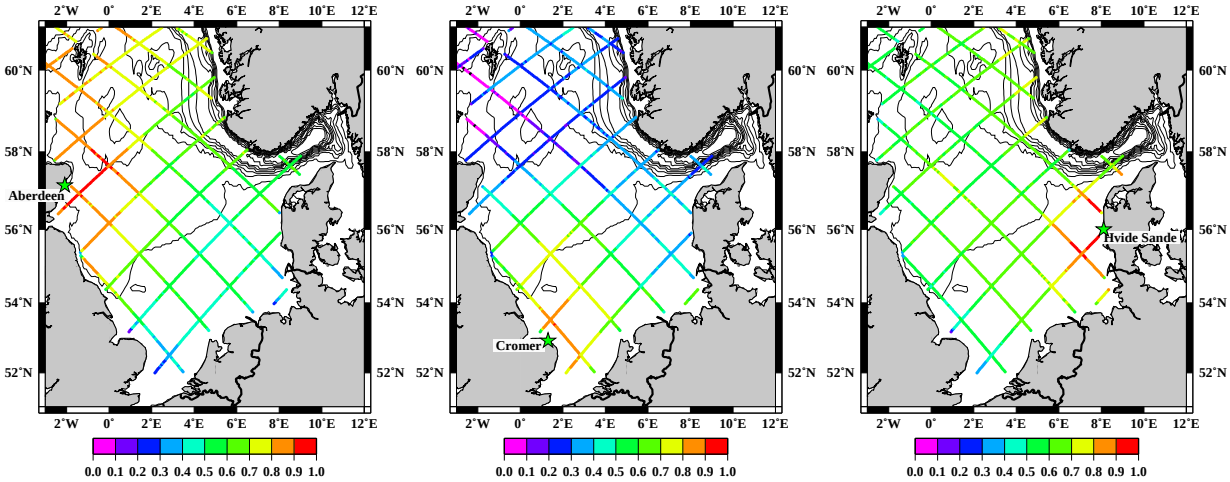

Figure 4.5: 3 examples correlation between T/P and individual water level recorders at Aberdeen (left), Cromer (middle) and Hvide Sande (right). Correlations have been calculated in every T/P point and no along track averaging has been applied. Bathymetry is contoured.

for all three water level recorders when the distance between the two observations is not too large.

The correlation between the T/P and in situ observations is generally highest close to the recorder and decrease away from it. The figure shows that the spatial scales with high correlation (e.g. $\rho > 0.5$) are largest for the Hvide Sande and Aberdeen recorders where correlations are above 0.4 for all the North Sea. The agreement between the T/P and the Cromer recorder has a more regional character than the other recorders and the satellite observations in the northern North Sea fall below the 99% significance level which is 0.2 for 150 independent observations.

land effects make it impossible to obtain satellite observations very close to land as described in chapter 1. The closest observations in the North Sea are generally 20-30 km away from the coastal recorders. The exception is at Hvide Sande where observations are obtained as close as 12 km from the water level recorder. The degrading of the observations due to land effects may explain why the highest correlations are not always obtained at the observations closest to the water level recorder as seen in figure 4.5

The results from the satellite cross overs provide a test for the consistency of the noise on satellite observations from different tracks. The correlations in figure 4.5 from the different ground tracks are similar at the cross overs for all three water

level recorders. This indicates a uniform T/P noise level which is independent of the specific track

The propagation of surges along the boundary, and the spatial scales of O(100km) is also evident from the figure. The T/P observations along the coast have higher correlation for the same distance to the water level recorder than T/P observations off the coast. This is e.g seen in the Aberdeen recorder where there is a significant difference between the north-south and east-west extend of high correlations.

To compare with the T/P observations and to get an idea of the quality of the ERS data, a pointwise correlation analysis was also carried out with the ERS 1+2 data. A minimum of 50 pairs of observations was required before the correlation was calculated, resulting in a 99% significance level of 0.35 when the 35 day observations are assumed independent.

Shown in figure 4.6 are the results from the same three water level recorders as

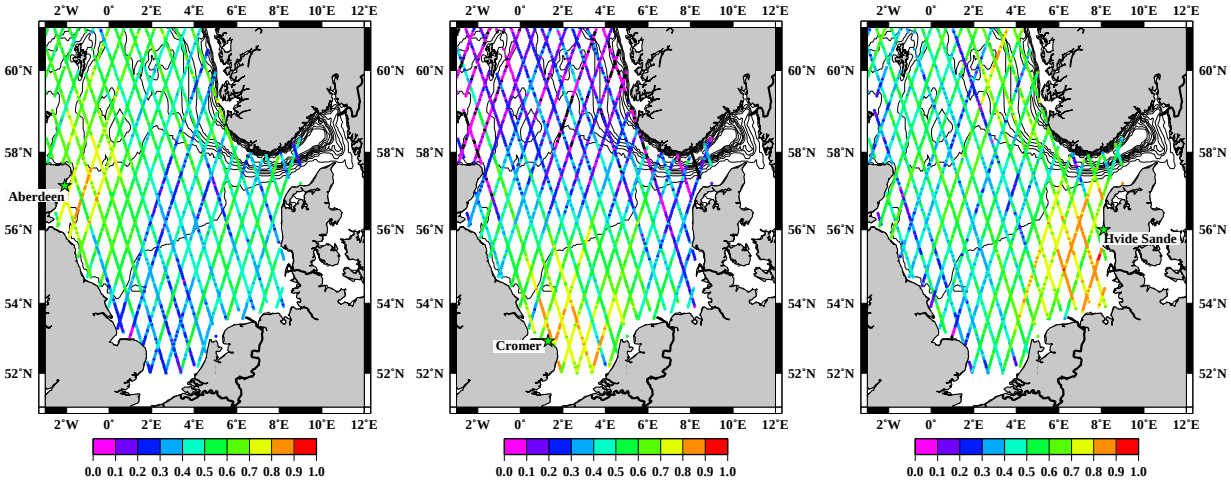

Figure 4.6: Same as figure 4.5 except for the ERS 1+2 observations.

for T/P in the previous figure and it is clear that the higher spatial sampling does not result in a spatially more uniform correlation compared to T/P. Highest values are again obtained close to the specific water level recorder but the correlations are significantly lower than the T/P observations. It is evident that the noise in some tracks is significantly higher than other tracks as they stand out with substantially lower correlation than other tracks. The cross-over discrepancies in the correlations are larger for the ERS data than the T/P. The uncertainty in the results are of course larger for the ERS data when fewer observations are available for the calculation, but it can not account for the difference in figure 4.5 and 4.6 which is ascribed to higher noise level in the ERS data. The lowered correlations along specific ground tracks, indicate that the errors arise from the uncertainty in the orbit determination because of the very large correlation scales of these errors as discussed in chapter 1.

The results from the comparison between the water level recorders and the satellite data are summarized in table 4.1 with maximum and mean correlations for all the water level recorders. The table shows that whereas the maximum T/P correlations are all above 0.9, ERS correlations are lower with maximum correlations around

	Max T/P	Mean T/P	Max ERS	Mean ERS
	ρ	ρ	ρ	ρ
Lerwick	0.96	0.67	0.80	0.45
Aberdeen	0.94	0.67	0.86	0.49
North Shields	0.94	0.61	0.86	0.48
Whitby	0.93	0.55	0.82	0.45
Cromer	0.90	0.41	0.85	0.38
Hvide Sande	0.95	0.63	0.91	0.52

Table 4.1: Maximum correlation obtained in the comparison of one water level recorder and the satellite observations. Shown is also the mean correlations of all the positions with satellite observations in the North Sea.

0.85. Both satellites obtain very high correlation with the Hvide Sande water level observations which was expected due to the maximum in SSH variability (figure 4.3).

The large spatial scales of the SSH fluctuations in the North Sea, found in section 4.4, are also seen in the T/P mean correlations where 4 of the recorders have correlations above 0.6 in in table 4.1. Lower correlations is again found with the ERS observations and both satellites agree that the Cromer recorder is worst of the 6 recorder to describe the sea level in all the North Sea. This is probably because the recorder is influenced by local shallow water processes such as nonlinear tidal constituents as evident from figure 4.2

Even though the tide gauges described exactly the SSH at the positions of the T/P satellite we would not obtain a correlation of 1 as the T/P measurement errors put an upper limit to the attainable correlations. For a signal variability of 20 cm the upper limit is 0.96 for the T/P satellite with 4 cm noise and 0.88 for the ERS with noise levels of 7 cm. These correlations can of course only be reached if the noise on the water level recorders is zero and if the detiding has removed the same signals from the two time series.

From the sections above, it can be concluded that the weather induced sea level variability in the North Sea has small time scales of 10-60 hours, large spatial scales of several hundred of kilometers and propagates counterclockwise along the coast with high correlation. In addition, the correspondence between T/P altimetry observations and water level recorders is very good to the times when altimetry observations were available and not too far away from the water level recorder. This indicates that the description of the sea level at a given position and time in the North Sea can be improved by combining altimetry and water level recorders. The agreement between altimetry and in situ sea level suggest that the T/P data can be used to determine how the different tide gauges can be combined in every position with T/P observations. The method used for this is the multivariate regression model which is described below.

4.6 Multivariate regression model

The regression analysis is derived with the notation from Emery and Thomson (1998) and Chelton (1998).

The idea with the method is to construct a model $\hat{\eta}$ that models the observed sea surface height by T/P, η

$$\eta(x, y, t) = \hat{\eta}(x, y, t) + \epsilon(x, y, t) \tag{4.15}$$

with an error ϵ which is the signal not explained by the model.

In every T/P observation point we want to perform a multivariate regression of T/P observations onto the water level recorder measurements, ζ and determine the coefficients β_i

$$\eta(t) = \sum_{i=1}^{M} \beta_i \cdot \zeta_i(t) + \epsilon(t) \tag{4.16}$$

Where M is the number of water level recorders used in the M-parameter regression model. If we at a given position have N observations in time of η and ζ and if the η observations are uncorrelated, the matrix version of equation 4.15 will take the form

$$\vec{y} = \mathbf{X}\vec{b} + \vec{e} \tag{4.17}$$

Where $\vec{y} = \eta_1, \eta_2, ..., \eta_N$ is the time series of altimetry observations, $\vec{b} = \beta_1, \beta_2, ..., \beta_M$ is the unknown weights to be determined, $\mathbf{X} = (\vec{\zeta_1}, \vec{\zeta_2}, ..., \vec{\zeta_M})$ is the data matrix that contains all the water level observations and $\vec{e} = \epsilon_1, \epsilon_2, ..., \epsilon_N$ is the error vector.

The system is overdetermined for $N > M$ and the regression coefficients are found by the least squares solution

$$\vec{b} = (\mathbf{X}' \cdot \mathbf{X})^{-1}\mathbf{X}' \cdot \vec{y} \tag{4.18}$$

which minimizes the mean of the squared errors:

$$< e^2 >= \frac{\sum_{i=1}^{N} {e_i}^2}{N} \tag{4.19}$$

The regression model above implies that the temporal mean is subtracted from the T/P data and that the altimetry observations are independent. The T/P repeat period of 10 days and the time scales of maximum 60 hours from figure 4.2 ensure that this assumption is valid

The performance of the regression model, or the model skill, is often measured as how much variance the model is able to explain of the true variance. This is called the hindcast skill S and is defined as

$$S = \frac{\sigma_{\hat{\eta}}^2}{\sigma_{\eta}^2} = 1 - \frac{< e^2 >}{\sigma_{\hat{\eta}}^2} = \rho_{\eta\hat{\eta}}^2 \tag{4.20}$$

where the correlation, ρ, is calculated over the all the observations available for the model. The estimated skill above gives a measure of the relative performance of the model, as it is dependant on the variance of the data. Alternatively, an absolute model skill which is independent of the variance of the observations can be expressed as the Root Mean Square (RMS) values of the residuals not explained by the model. This estimate is just the square root of the mean squared errors from equation 4.19

$$RMS_e = \sqrt{< e^2 >} \tag{4.21}$$

which is calculated in every point where the regression is performed. Both estimates of the model skill will be used here to assess the performance of the regression model.

When the mean is taken out of the observations, the maximum number of parameters in the regression model is 6, equal to the number of water level recorders. The minimum number of recorders is 1, in which case the regression would be a simple linear regression.

Model performance

The regression was performed pointwise upon the time series in every T/P observation along the ground tracks. The subsampling of the in situ observations was performed as in section 4.5, using averages within 3 hours of the T/P observations. As an example of the model performance, the time series of T/P observations in one point off Aberdeen is shown in figure 4.7 together with the regression model estimate from

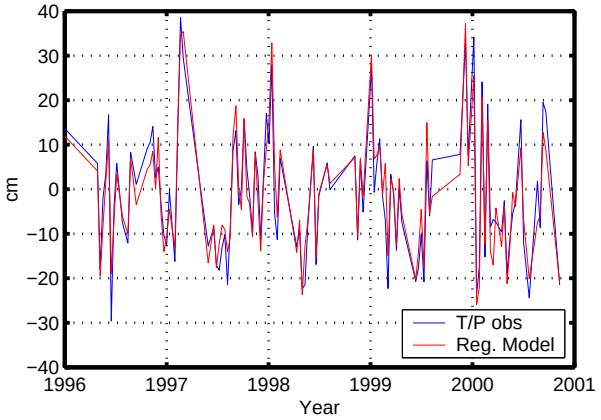

Figure 4.7: Timeseries of T/P observed sea level (blue) and estimates from the regression model that uses all 6 water level recorders (red).

all 6 water level recorders. The RMS_e error at this point which is located about 100 km off Aberdeen is 4.5 cm and the Hindcast skill is 0.9. The figure illustrates the high frequency nature of the fluctuations which look like random noise in the 10 days observations. However, the close relationship between the T/P and the regression model reveal that the fluctuations are real weather induced signals.

The model performance for all 6 water level recorders is shown in figure 4.8 where the hindcast skill S is displayed to the left and RMS_e to the right. The mean hindcast skill is 0.699 for all the points in the North Sea and the mean RMS_e is 8.2 cm. The figure displays that the model can explain >80 % of the variance in the north, along the British east coast and off Hvide Sande whereas lowest skill (< 0.5) is found in the central North Sea and in the end points in some tracks. The residuals in the left picture reveals that in terms of predicting the absolute sea level the smallest errors are in the North and along the British east coast where $RMS_e < 8$ cm. The region to the south and east with largest errors (>12 cm) coincides with the largest SSH variability seen in figure 4.3. The prediction with the 123456 regression model is summarized in figure 4.9 which is a scatterplot of all the pairs of T/P observations and model predictions in the North Sea, regardless of time and position of the prediction ($\sim 2 * 10^5$ pairs of observations). The figure shows the number of points in each 1 cm

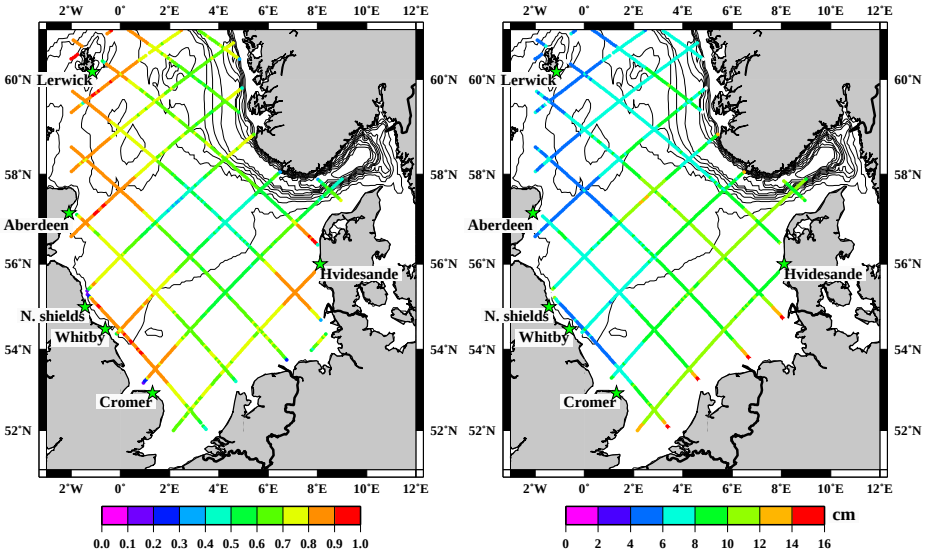

Figure 4.8: Performance of the regression model where the T/P observations have been regressed upon the 6 water level recorders indicated by the green stars. Left: Hindcast skill as in equation 4.20, right: RMS_e in cm of the residuals not explained by the model as in equation 4.21. The black contour lines denote the bathymetry.

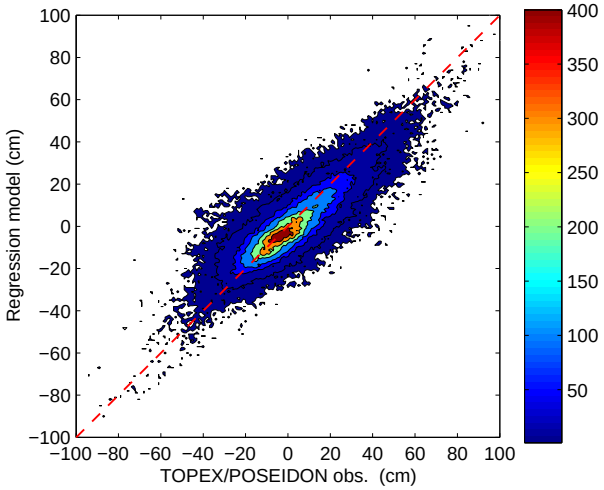

Figure 4.9: Scatterplot of all the observations and predictions in the North Sea, based upon the 123456 regression model ($\sim 2 * 10^5$). Shown in color is the number of points in every 1 cm square. The red dashed line indicate a line with slope 1. Contour lines are drawn at 1,10,50,100,200,300 and 400.

square and the red line indicate the line with slope 1 where the perfect predictions would be located upon. The figure shows that the regression model underestimates the T/P variations as we would expect since the model is regressed upon the T/P observations. More interesting is it that the error does not depend much upon the amplitude of the signal. Even SSH anomalies above 80 cm are predicted within 20 cm by the regression model, indicating that the regression model can also be used in

conditions with extreme water level anomalies.

Due to gaps in the water level recorders, we cannot expect to have observations from all water level recorders at all the times when T/P observations are available. It is therefore important to investigate how the model performance degrades as fewer than 6 water level observations are used in the regression. As noted by Chelton (1998) the hindcast skill of the model will always increase when additional water level recorders are included in the regression. This is also seen in table 4.2 where the mean hindcast skill in the North Sea is listed for different combinations and numbers of water level recorders. The importance of the Hvide Sande tide gauge is demonstrated

Water level recorders	S	RMS_e	N
26	0.557	10.4	209
256	0.653	9.1	187
1256	0.691	8.5	157
1236	0.677	8.7	170
1246	0.672	8.8	174
12456	0.697	8.4	155
12345	0.638	9.5	180
123456	0.704	8.2	148

Table 4.2: Hindcast skill of the regression model for different water level recorders. The water level recorders are numbered counterclockwise from Lerwick, i.e. Lerwick=1, Aberdeen=2, North Shields=3, Whitby=4, Cromer=5, Hvide Sande=6

in the table where the performance of the Aberdeen, Cromer and Hvide Sande (256) regression model is superior to a model consisting of all the water level recorders except the Hvide Sande (12345). However, it is also evident from the table that the gap in the Hvide Sande time series of one year results in a substantial decrease in the number of observations in each point. Changing the Hvide Sande recorder with the Cromer record for $M = 5$ thus gives a mean increase of 25 observations in each point.

When the Hvide Sande water level recorder is included in the regression model, table 4.2 shows that little is gained for $M > 4$ by adding extra information. The models explain more than 67 % and the maximum improvement in the skill is only 3% going from 4 to 6 parameter models.

In the estimation of regression coefficients, the water level observation were used for the same time as the T/P observations. However, the cross correlations showed that, e.g. the Aberdeen water level recorder lags Hvide Sande with 12 hours suggesting that better performance can be obtained if the water level recorders are shifted individually. The effect of lag or leads will be examined below

Regression with lag or leads

To examine the impact of lags or leads in the time series, the regression was performed 25 times with the 1246 model where the water level time series were shifted from $t_{T/P} - 12$ hour to $t_{T/P} + 12$ hour with a time step of one hour. The time lag with maximum model skill was close to $t = 0$ for most of the points and the maximum improvement in the correlation was only 0.011 larger in the mean than for $t = 0$.

Furthermore, the improvement in model skill was examined by shifting the individual time series with -6,0 and +6 hours. All combinations of these three lags for each of the 4 water level recorders were used in the regression, giving $3^4 = 81$ model estimations in every T/P position. The best model performance out of the 81 estimates in every point had mean correlations of 0.017 higher than using the non lagged time series for input.

The results above thus suggest that little improvement in the model skill can be obtained by shifting the water level time series in time to account for the cyclonic propagation of the surges. The explanation is probably that the two water level recorders in the end, Lerwick and Hvide Sande have larger time scales than the time it takes the anomalies to propagate around the North Sea. The regression results used in the following will therefore be from the water level observations taken at the same time as the T/P observations.

4.7 Prediction of ERS observations

ERS observations from version 5 noib (see chapter 1) are used to validate the performance of the model for positions and times that do not coincide with the T/P observations. The number of observations in the validation is increased by using ERS observations from cross-overs where the two tracks gives a maximum of 170 observations. The position of the crossovers were found as the exact position where two ground tracks intersect. The time series of SSH anomalies were constructed from the ERS 5 notide observations by interpolation in each track of the 5 observations closest to the cross-over position. The mean in each track was removed before the two time series were merged and detiding (described in section 4.3) was subsequently performed on the merged series to give a more robust tidal estimate. The S_2 tidal constituent is always sampled with the same phase within a ground track, due to the infinite alias period in table 1.2. This means that false SSH variability can be introduced in areas with a large S_2 constituents, when the mean is removed in every track prior to the tidal filtering. The cross over calculation was tested using the absolute heights in every ground track but this resulted in a poorer performance due to offsets in specific ground tracks.

A 4 parameter regression model was used in the validation of the ERS observations because as discussed in the previous section, the improvement in the hindcast skill is small, going from 4 to 5 or 6 parameters whereas the numbers of observations decrease substantially. The regression model based upon Lerwick, Aberdeen, Whitby and Hvide Sande (1246 in table 4.2) was chosen according to table 4.2 to get the optimal combination of good hindcast skill and few data gaps.

Regression results are only available at positions with T/P observations but these do not coincide with the ERS cross-over points and a method is therefore required to extend the results away from the T/P ground tracks. Methods like linear spatial interpolation in every timestep of the surrounding model SSH estimates, interpolation of model weights, and using nearest T/P results were examined. The performance of the different methods did not vary much and the simplest method of using the regression results from the nearest T/P observations was therefore chosen here.

The ability of the regression model described above to describe the SSH at the ERS

cross-over observations is shown in figure 4.10 as correlations between observed and predicted sea level variations (left) and RMS differences in centimeters (right). The

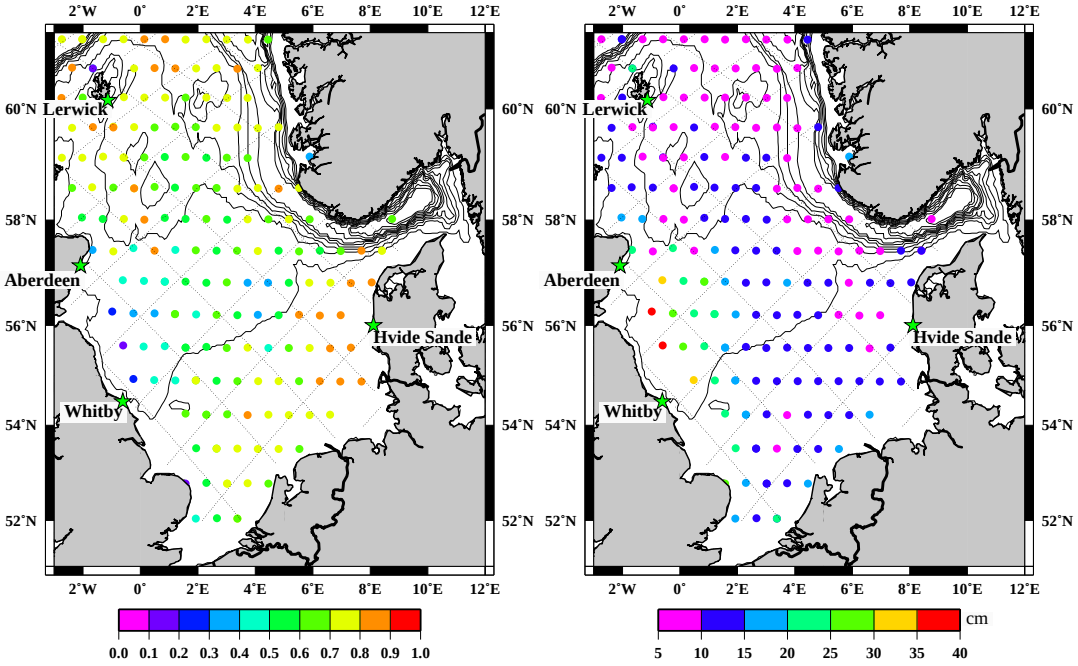

Figure 4.10: Correlation (right) and RMS differences (left) between ERS cross-over observations and predicted ssh from the regression model with Aberdeen, Lerwick, Whitby and Hvide Sande water level recorders. Bathymetry is contoured and T/P groundtracks are shown in black. The regression weights used here are estimated in the nearest T/P observations.

T/P ground tracks are overlaid in the figure to demonstrate that there is no apparent relation between the distance from the T/P ground track to the ERS cross-over and the correlation.

The figure shows that high correlations ($\rho > 0.8$) are obtained off the Danish west coast and in the northwestern North Sea. The lowest correlations are found off the British east coast between Aberdeen and Whitby. Higher correlations were found in this area between ERS along track observations and the Aberdeen tide gauge as seen from figure 4.6. It is therefore likely that the low correlations arise from a problematic cross-over calculation due to the S_2 tidal constituent. This is supported by the results in Andersen (1994) where the largest S_2 amplitudes in the North Sea are found along the British east coast.

The mean correlation in crossover points where more than 40 observations are available is 0.68 with RMS residuals of 13 cm in the mean. The RMS error estimates include noise on the ERS data and RMS of the residuals is thus an upper bound on the error in the regression model and in terms of describing the true sea level, the errors in this method are probably on the order of 5-10 cm. To test the results obtained here with the regression model, the performance will be compared to the results from using only in situ or satellite observations.

Sea level from T/P

To estimate the sea level at ERS cross-overs using only T/P, it was necessary to use observations several hundred kilometers away to increase the temporal resolution. A time series with high resolution in time was constructed at each cross-over from the closest observation in each track within 200 km. The temporal resolution was thereby increased from the 9.916 days to 1-3 days and the estimated SSH were obtained by interpolating among these observations to the exact time of the ERS observations. When this method is used for predicting the sea level, the mean correlation between T/P estimated SSH and observed by the ERS observations is 0.53 and the RMS difference is 21 cm. Other methods to estimate the SSH from T/P were tested but all displayed poorer agreement with the ERS observations.

Sea level from in situ

A simple method of predicting the sea level in the interior only from water level recorders is to use the observed sea level from the gauge closest to the position of prediction. When the same 4 water level recorders are used as for regression model, a mean correlation of 0.62 is obtained with this method for the cross overs in the North Sea. The results are maybe not far from the regression estimate but the absolute performance is limited by the fact that water level recorders are all situated at the coast where the variability is higher than in the interior. Without additional information from altimetry about the off shore decrease in variability, the water level recorders may capture the variations, but the amplitudes are in error which shows up in the RMS difference of 19 cm.

Sea level from Mike 21

The 2 dimensional hydrodynamic model, Mike 21 developed at Danish Hydraulic Institute, was run in a setup for the North Sea and Baltic Sea with a resolution of up to 1 nautical mile (Huess, 2001). The model was run for a year under the GEOSONAR project, forced with tides at the open boundaries and with atmospheric forcing from the HIRLAM model. The SSH variations modeled by Mike 21 was validated against 426 T/P ground track observation for a period of 3 months by subtracting the model SSH from the T/P observed SSH. The mean standard deviation of the residuals was 20 cm with atmospheric forcing and 17 cm with only tides in the Mike 21 model. The larger residuals for the HIRLAM experiments are probably related to a combination of larger variance and phase differences between observed and modeled SSH (*Huess, personal communication*).

The prediction results for the four methods are summarized in table 4.3. It is

Method	ρ	RMS Diff. (cm)
T/P only	0.53	20
In situ only	0.62	19
Mike 21 - TP		20
DMI operational, Hvide Sande 2000	0.92	18
Regression	0.68	13

Table 4.3: Performance of the different methods used to predict sea level at ERS cross overs. All values are mean over the all the cross overs in the North Sea.

thus clear from the results above that significant improvement is obtained when the coastal water level recorders are used in combination with the T/P observations in a regression model. The model works best at the T/P ground tracks where the regression coefficients have been estimated but good performance is also seen away from these positions due to the large spatial scales of the signals.

4.8 Conclusion

The observations from coastal sea level recorders and satellite altimetry each give a consistent picture of the weather induced variability in the North Sea. The dominating fluctuations propagate counterclockwise around the North Sea with time scales of 10-60 hours and large spatial scales. The in situ observations reveal propagation velocities of $\sim$ 100 km/day and the satellite observations indicate spatial scales of several hundred kilometers with largest variability at the coast. These findings correspond very well with the propagation of a Kelvin wave, together with shallow water amplification of SSH variability. In addition, the high correlation (>0.7) between Aberdeen and Hvide Sande time series at a 12 hour lag indicates the importance of the externally driven surges.

The comparison between one water level recorder and the T/P satellite, revealed that very good agreement could be obtained with maximum correlations above 0.9 for all the 6 sea level gauges. A similar comparison between ERS and water level recorders showed lower correlation due to enhanced noise in the ERS observations.

The weather induced processes in the North Sea with small time scales, large spatial scales and the good agreement between the T/P and in situ sea level observations provide a good basis for describing the sea level with a multivariate regression model. Regression of the water level recorder data onto the T/P observations could thus explain about 60 % of the T/P variance in the mean over the North Sea. The mean RMS difference between predicted and observed SSH of 8.2 cm includes the T/P measurement errors of several centimeters and the true RMS errors of the model is thus even lower.

ERS observations from cross overs served as independent data to test the model against. The test gave a mean correlation of 0.68 and RMS differences of 13 cm between the regression model and the ERS SSH. The best performance was found in the northern North Sea and off the Danish west coast with correlations above 0.8 and RMS of residuals below 10 cm. The higher performance of these cross-over points is probably because of the reduced influence from tides. In addition, the enhanced inverse barometer signal in the northern part is likely to give a good prediction result because the signal is spatially homogenous.

In the light of the performance of the regression model in describing the SSH observations from both T/P and ERS cross-over observations, we can thus conclude that the true sea surface height fluctuations in the North Sea can be described within 5-10 cm. This accuracy can be obtained all over the North Sea using real time input from only 4-6 coastal water level recorders in the regression model determined with T/P observations.

The performance of the regression model in describing the real time SSH in all the North Sea is thus significantly better than what has been obtained in a validation

of the Mike 21 model against T/P (Huess, 2001) and the operational storm surge model on the Danish west coast (Nielsen and Nielsen, 2000, Nielsen, 2001b). The explained variances are higher for the model results as they include the tidal variations. However, inclusion of tides in the regression model will probably not have a large effect on the RMS errors due to the deterministic nature of the tidal SSH variability. Furthermore, the RMS errors due to differences in the in situ and altimetry detiding are avoided when detiding is not applied. The largest effect of including the tides is therefore likely to be a substantial improvement in the Hindcast skill of the regression model.

The results above have thus demonstrated the potential for combining altimetry and tide gauge observations in the North Sea. The outcome is an accurate real time description of sea surface height at a give position in the North Sea from only 4 coastal tide gauges around the North Sea. The results can be used as an independent sea level product in the North Sea or to validate the models as they are more accurate than the models. The regression model can also serve as boundary conditions at the open boundaries or in a first step of a data assimilation. In any case, this study demonstrates the potential of combining the altimetry and water level observations.

5

Conclusions

Bibliography

Aken, H. M. (2001). The hydrography of the mid-latitude Northeast Atlantic Ocean - Part III: the subducted thermocline water mass. *Deep-Sea Res.*, 48:237–267.

Aken, H. M. and Becker, G. (1996). Hydrography and through-flow in the north-eastern North Atlantic Ocean: the NANSEN project. *Prog. Oceanography*, 38:297–346.

Andersen, O. B. (1994). Ocean tides in the northern North Atlantic and adjacent seas from ERS 1 altimetry. *J. Geophys. Res.*, 99(C11):22557–22573.

Andersen, O. B. (1995). Global ocean tides from ERS 1 and TOPEX/POSEIDON altimetry. *J. Geophys. Res.*, 100(C12):25249–25259.

Andersen, O. B. (1999). Shallow water tides in the northwest European shelf region from TOPEX/POSEIDON altimetry. *J. Geophys. Res.*, 104(C4):7729–7741.

Arhan, M. (1990). The North Atlantic Current and Subarctic Intermediate Water. *J. Mar. Res.*, 48:109–144.

Armstrong, E. M. and Cuervo, J. V. (2001). The New Global Satellite-Based Sea surface Temperature Climatology. *Geophys. Res. Letter*, 28(22):4199–4202.

Bacon, S. (1998). decadal variability in the outflow from the Nordic seas to the deep Atlantic Ocean . *Nature*, 394:871–874.

Bailey, R., Gronell, A., Phillips, H., Tanner, E., and Meyers, G. (1994). Quality Control Cookbook for Expendable Bathythermograph (XBT) Data . CSIRO Marine Laboratories Report No. 221 75 pp.

Barton, I. J. (1995). Satellite derived sea surface temperatures: Current status. *J. Geophys. Res.*, 100(C5):8777–8790.

Barton, I. J. (1998). Improved techniques for the derivation of sea surface temperatures from ATSR data. *J. Geophys. Res.*, 103(C4):8139–8152.

Barton, I. J., Prata, A. J., and Cechet, R. P. (1995). Validation of ATSR in Australian Waters. *J. Atm. Oce. Tech.*, 12(2):290–300.

Belkin, I. M. and Levitus, S. (1996). Temporal variability of the Subarctic Front near the Charlie-Gibbs Fracture Zone. *J. Geophys. Res.*, 101(C12):28317–28324.

Belkin, I. M., Levitus, S., Antonov, J., and Malmberg, S. A. (1998). "Great Salinity Anomalies" in the North Atlantic . *Prog. Oceanography*, 41:1–68.

Bersch, M., Meincke, J., and Sy, A. (1999). Interannual thermohaline changes in the northern North Atlantic 1991-1996. *Deep-Sea Res. II*, 46:55–75.

Blindheim, J. and Ålandsvik, B. (1995). Episodic formation of intermediate water along the Greenland Sea Arctic Front . *ICES CM/Mini*, 6:11.

Borenäs, K. M. and Lundberg, P. A. (1988). On the Deep-Water Flow through the Faroe Bank Channel. *J. Geophys. Res.*, 93(C2):1281–1292.

Borenäs, K. M. and Pratt, L. (1994). On the use of rotating hydraulic models . *J. Phys. Oceanography*, 24:108–123.

Broecker, W. S. (1991). The great ocean conveyor. *Oceanography*, 4:79–89.

Brooks, R. L., Lockwood, D., and Hancock III, D. W. (1990). Effects of Islands in the Geosat Footprint. *J. Geophys. Res.*, 95(C3):2849–2855.

Bruce, J. G. (1995). Eddies southwest of the Denmark Strait. *Deep-Sea Res.*, 42(1):13–29.

Buch, E., Malmberg, S. A., and Kristmannsson, S. S. (1992). Arctic ocean deep water masses in the Western Iceland Sea . *ICES CM*, 2(C).

Casey, K. S. and Cornillon, P. (1999). A Comparison of Satellite and In Situ-Based Sea surface Temperature Climatologies. *J. Climate*, 12:1848–1863.

Chelton, D. B. (1998). Physical Oceanographic and Atmospheric Data Analysis. OC682, Course Notes, Oregon State University.

Chelton, D. B., deSzoeke, R. A., Schlax, M. G., Naggar, K. E., and Siwertz, N. (1998). Geographical variability of the first-baroclinic Rossby radius of deformation. *J. Phys. Oceanography*, 28:433–460.

Chelton, D. B., Ries, J. C., Haines, B. J., Fu, L.-L., and Callahan, P. S. (2001). *In Satellite Altimetry and Earth Sciences*, volume 69, chapter 1, pages 1–122. Academic Press. Edited by Fu. L.-L. and Cazenave, A.

Cheney, R., Miller, L., Agreen, R., Doyle, N., and Lillibridge, J. (1994). TOPEX/POSEIDON: the 2-cm solution. *J. Geophys. Res.*, 99(C12):24555–24563.

Curry, R. G. and McCartney, M. S. (2001). Ocean Gyre Circulation Changes Associated with the North Atlantic Oscillation. *J. Phys. Oceanography*, 31(12):3374–3400.

Deser, C., Alexander, M. A., and Timlin, M. S. (1996). Upper ocean thermal variations in the North Pacific during 1970-1991. *J. Climate*, 9:1840–1855.

Dickson, R. R. and Brown, J. (1994). The production of North Atlantic Deep Water: Sources,rates and pathways. *J. Geophys. Res.*, 99(C6):12319–12341.

Dickson, R. R., Lazier, J., Meincke, J., Rhines, P., and Swift, J. (1996). Long-term coordinated changes in the convective activity of the North Atlantic . *Prog. Oceanography*, 38:241–295.

Emery, W. J., Castro, S., Wick, G. A., Schlussel, P., and Donlon, C. (2001). Estimating Sea Surface Temperature from Infrared Satellite and In Situ Temperature Data. *Bull. Meteorol. Soc.*, 82(12):2773–2785.

Emery, W. J. and Thomson, R. E. (1998). *Data Analysis Methods in Physical Oceanography*. Elsevier, 2 edition.

Esbensen, S. K. and Kushnir, Y. (1981). The Heat Budget of the Global Ocean: an Atlas based on Estimates from Surface Marine Observations. Technical report, Oregon State University.

Esselborn, S. and Eden, C. (2001). Sea Surface Height changes in the North Atlantic Ocean related to the North Atlantic Oscillation. *Geophys. Res. Letter*, 28(18):3473–3476.

Esselborn, S. C. (2001). *Meereshöhen und ozeanische Zirkulation im Nordatlantik zwischen 1992 und 1998*. PhD thesis, University of Hamburg.

Ferry, N., Reverdin, G., and Oschlies, A. (2000). Seasonal sea surface height varaibility in the north atlantic ocean. *J. Geophys. Res.*, 105(C3):6307–6326.

Flather, R. A. (2000). Existing operational oceanography. *Coastal Engineering*, 41:13–40.

Frankignoul, C., Coëtlogon, G., Joyce, T. M., and Dong, S. (2001). Gulf Stream Varaibility and Ocean-Atmosphere Interactions. *J. Phys. Oceanography*, 31(12):3516–3529.

Fratantoni, D. M. (2001). North Atlantic surface circulation in the 1990's observed with satellite-tracked drifters. *J. Geophys. Res.*, 106(C10):22067–22093.

Fu, L.-L. and Chelton, D. B. (2001). *In Satellite Altimetry and Earth Sciences*, volume 69, chapter 2, pages 133–169. Academic Press. Edited by Fu. L.-L. and Cazenave, A.

Fu, L. L., Christensen, E. J., Yamarone, C. A., Lefebvre, M., Menard, Y., Dorrer, M., and Escudier, P. (1994). TOPEX/POSEIDON Mission overview. *J. Geophys. Res.*, 99:24369–24381.

Furevik, T. (2000). On Anomalous Sea Surface Temperatures in the Nordic Seas. *J. Climate*, 13:1044–1053.

Furnes, G. K. (1980). Wind effects in the North Sea. *J. Phys. Oceanography*, 10:978–985.

Ganachaud, A., Wunsch, C., Kim, M.-C., and Tapley, B. (1997). Combination of TOPEX/POSEIDON data with a hydrographic inversion for determination of the oceanic general circulation and its relation to geoid accuracy. *Geophys. J. Int.*, 128:708–722.

Ganopolski, A. and Rahmstorf, S. (2001). Rapid changes of glacial climate simulated in a coupled climate model. *nature*, 409:153–158.

Gill, A. E. (1977). The hydraulics of rotating channel flow. *J. Fluid Mech.*, 80:641–671.

Gill, A. E. (1982). *Atmosphere-Ocean Dynamics*, volume 30 of *International Geophysics Series*. Academic Press.

Gill, A. E. and Niiler, P. P. (1973). The theory of the seasonal variability in the ocean. *Deep-Sea Res.*, 20:141–177.

Gilson, J., Roemmich, B., and Fu, L. L. (1998). Relationship of TOPEX/Poseidon altimetric steric height and circulation in the North Pacific. *J. Geophys. Res.*, 103(C12):27947–27965.

Girton, J. B. and Sanford, T. B. (2001). Synoptic sections of the Denmark Strait Overflow. *Geophys. Res. Letter*, 28(8):1619–1622.

Hansen, B. and Østerhus, S. (1998). ICES NANSEN Project. *ICES Cooperative Research Report*, 225:1–82.

Hansen, B. and Østerhus, S. (2000). North Atlantic-Nordic Seas exchanges. *Prog. Oceanography*, 45:109–208.

Hansen, B., Turrell, W. R., and Østerhus, S. (2001). Decreasing overflow from the Nordic Seas into the Atlantic Ocean through the Faroe Bank Channel since 1950. *Nature*, 411:927–930.

Heaps, N. S. (1983). Storm surges, 1967-1982. *Geophys. J. R. Soc.*, 74:331–376.

Holt, J. T. and James, I. D. (2001). An s coordinate density evolving model of the northwest European continental shelf 1, Model description and density structure. *J. Geophys. Res.*, 106(C7):14015–14034.

Holt, J. T., James, I. D., and Jones, J. E. (2001). An s coordinate density evolving model of the northwest European continental shelf 2, Seasonal currents and tides. *J. Geophys. Res.*, 106(C7):14035–14053.

Høyer, J. (1999). Detection of oceanic signals in the TOPEX/POSEIDON data. Master's thesis, Department of Geophysics, Niels Bohr Institute of Astronomy, Physics and Geophysics, University of Copenhagen.

Høyer, J. and Quadfasel, D. (2001). Detection of deep overflows with satellite altimetry. *Geophys. Res. Letter*, 28(8):1611–1614.

Høyer, J., Quadfasel, D., and Andersen, O. B. (2002). Deep ocean currents detected with satellite altimetry. *Submitted to Candian J. Rem. Sens.*

Huess, V. (2001). Sea level variations in the north sea - from tide gauges, altimetry and modelling. Technical Report 01-08, Danish Meteorological Institute.

Hurrell, J. W. (1995). Decadal trends in the North Atlantic Oscillation: regional temperatures and precipitation. *Science*, 269:676–679.

Iorga, M. C. and Lozier, S. M. (1999a). Signatures of the Mediterranean outflow from a North Atlantic climatology 1. Salinity and density fields. *J. Geophys. Res.*, 104(C11):25985–26009.

Iorga, M. C. and Lozier, S. M. (1999b). Signatures of the Mediterranean outflow from a North Atlantic climatology 2. Diagnostic velocity fields. *J. Geophys. Res.*, 104(C11):26011–26029.

Iselin, C. O. (1939). The influence of vertical and horizontal turbulence on the characteristics of waters at mid-depth. *Trans. of AGU*, 3:414–417.

Jiang, L. and Garwood, W. J. (1996). Three-Dimensional Simulations of Overflows on Continental Slopes . *J. Phys. Oceanography*, 26:1214–1233.

Jonsson, S. (1999). The circulation in the northern part of the Denmark Strait and its variability . *ICES CM*, 6.

Josey, S. A. (2000). A Comparison of ECMWF, NCEP-NCAR, and SOC Surface Heat Fluxes with Moored Buoy Measurements in the Subduction Region of the Northeast Atlantic. *J. Climate*, 14(8):1780–1789.

Joyce, T. M., Deser, C., and Spall, M. A. (2000). The Relation between Decadal Variability of Subtropical Mode Water and the North Atlantic Ascillation. *J. Climate*, 13:2550–2569.

Jungclaus, J. H., Hauser, J., and Käse, R. H. (2001). Cyclogenesis in the Denmark Strait Overflow. *J. Phys. Oceanography*, 31(11):3214–3229.

Käse, R. H. and Krauss, W. (1996). *The Gulf Stream, The North Atlantic Current, and the Origin of the Azores Current*, chapter 10, pages 291–337. The Warmwatersphere of the North Atlantic Ocean. Gebrüder Borntraeger, Berlin.

Käse, R. H. and Oschlies, A. (2000). Flow through Denmark Strait. *J. Geophys. Res.*, 105(C12):2827–2846.

Kauker, F. and Storch, H. (2000). Statistics of "Synoptic Circulation Weather" in the North Sea as Derived from a Multichannel OGCM Simulation. *J. Phys. Oceanography*, 30:3039–3049.

Kearns, E. J., Hanafin, J. A., Evans, R. H., Minnett, P., and Brown, O. B. (2000). An Independent Assessment of Pathfinder AVHRR Sea Surface Temperature Accuracy Using the Marine Emitted Radiance Interferometer (MAERI) . *Bull. Meteorol. Soc.*, 81(7):1525–1536.

Killworth, P. D. (1992). Flow properties in rotating, stratified hydraulics. *J. Phys. Oceanography*, 22:997–1017.

Killworth, P. D. (1995). Hydraulic control and maximal flow in rotating stratified hydraulics. *Deep-Sea Res.*, 42(6):859–871.

Killworth, P. D. (2001). On the rate of descent of overflows . *J. Geophys. Res.*, 106(C10):22267–22275.

Kilpatrick, K. A., Podest, G. P., and Evans, R. (2001). Overview of the NOAA/NASA advanced very high resolution radiometer Pathfinder algorithm for sea surface temperature and associated matchup database. *J. Geophys. Res.*, 106(C5):9179–9197.

Koblinsky, C. J., Beckley, B. D., Brenner, A., Tsaoussi, L. S., and Wang, Y. M. (1999a). NASA Ocean Altimeter Pathfinder Project Report 2: Data Set Validation. Technical report, National Aeronautics and Space Administration, Goddard Space Flight Center.

Koblinsky, C. J., Ray, R., Beckley, B. D., Wang, Y. M., Tsaoussi, L., Brenner, A., and Williamson, R. (1999b). NASA Ocean Altimeter Pathfinder Project Report 1: Data Processing Handbook. Technical report, National Aeronautice and Space Administration, Goddard Space Flight Center.

Kraus, E. B. (1972). *Atmosphere-Ocean Interaction*, volume 3 of *Oxford Monographs on Meteorology*. Oxford University Press.

Krauss, W. (1986). The North Atlantic Current. *J. Geophys. Res.*, 91(C4):5061–5074.

Krauss, W. (1995). Currents and mixing in the Irminger Sea and in the Iceland Basin. *J. Geophys. Res.*, 100(C6):10851–10871.

Krauss, W. (1996). A note on overflow eddies. *Deep-Sea Res.*, 43(10):1661–1667.

Krauss, W. and Käse, R. H. (1998). Eddy formation in the Denmark Strait overflow. *J. Geophys. Res.*, 103(C8):15525–15538.

Krauss, W. and Turner, J. S. (1967). A one-dimensionel model of the seasonal thermocline, 2, the general theory and its consequences. *Tellus*, 11:415–433.

Leetmaa, A. and Bunker, A. F. (1978). Updated charts of the mean annual wind stress, convergences in the Ekman Layers, and Sverdrup transports in the North Atlntic. *J. Mar. Res.*, 36(2):311–322.

Ma, X. C., Shum, C. K., Eanes, R. J., and Tapley, B. D. (1994). Determination of ocean tides from the first year of TOPEX/POSEIDON altimeter measurements. *J. Geophys. Res.*, 99(C12):24809–24820.

Macdonald, A. and Wunsch, C. (1996). A global estimate of the ocean circulation and heat fluxes. *Nature*, 382:436–439.

Mann, C. R. (1969). Temperature and salinity characteristics of the Denmark Strait overflow. *Deep-Sea Res.*, 16:125–137. Supplement.

Marshall, J. C., Nurser, G. A. J., and Williams, R. G. (1993). Inferring the Subduction Rate and Period over the North Atlantic. *J. Phys. Oceanography*, 23:1315–1329.

Marshall, J. C. and Schott, F. (1999). Open-ocean convection: Observations, Theory, and Models. *Rev. Geophysics*, 37(1):1–64.

Martin, P. J. (1985). Simulation of the Mixed Layer at OWS November and Papa With Several Models. *J. Geophys. Res.*, 90:903–916.

Mauritzen, C. (1996). Production of dense overflow waters feeding the North Atlantic across the Greenland–Scotland Ridge. *Deep-Sea Res.*, 43:769–835.

McCartney, M. S. and Mauritzen, C. (2001). On the origin of the warm inflow to the Nordic Seas. *Prog. Oceanography*, 51(1):125–214.

McCartney, M. S. and Talley, L. D. (1982). The Subpolar Mode Water of the North Atlantic Ocean. *J. Phys. Oceanography*, 12:1169–1188.

Mellor, G. L. and Yamada, T. (1974). A hierachy of of turbulence closure models for planetary boundary layers. *J. Atmos. Sci.*, 31:1791–1806.

Munk, W. H. and Cartwright, D. E. (1966). Tidal Spectroscopy and Prediction. *Philos. Trans. R. Soc. London, A*, 259:533–583.

Nielsen, J. W. (2001a). DMIs operationelle stormflodsvarslingssystem Version 2.0. Technical report, Danmarks Meteorologiske Institut . In Danish.

Nielsen, J. W. (2001b). Verification af vandstandsprognoser: 2000 . Technical report, Danmarks Meteorologiske Institut . In Danish.

Nielsen, J. W. and Nielsen, M. H. (2000). Verification af vandstandsprognoser: 1999. Technical report, Danmarks Meteorologiske Institut . In Danish.

Niiler, P. P. (1975). Deepening of the wind-mixed layer. *J. Mar. Res.*, 33(3):405–422.

Oberhuber, J. M. (1988). An atlas based on the 'COADS' data set: the budgets of heat, buoyancy and turbulent kinetic energy at the surface of the global ocean. Max-Planck-Institut fuer Meteorologie .

Orvik, K. A., Skagseth, O., and Mork, M. (2001). Atlantic inflow to the Nordic Sea: Current structure and volume fluxes from moored current meters, VM-ADCP and SeaSoar-ctd observations, 1995-1999. *Deep-Sea Res.*, 48(4):937–957.

Paillet, J. and Arhan, M. (1996). Shallow Pycnoclines and Mode Water Subduction in the Eastern North Atlantic. *J. Phys. Oceanography*, 26(1):96–114.

Parke, M. E., Stewart, R. H., Farless, D. L., and Cartwright, D. E. (1987). On the Choice of Orbits for an Altimetric Satellite to Study Ocean Circulation and Tides. *J. Geophys. Res.*, 92(C11):11693–11707.

Pollard, R. T., Griffiths, M. J., Cunningham, S. A., Read, J. F., Pẽrez, F. F., and Rios, A. F. (1996). Vivaldi 1991- A study of the formation, circulation and ventilation of Eastern North Atlantic Central Water . *Prog. Oceanography*, 37:167–192.

Polzin, K. L., Speer, K. G., Toole, J. M., and Schmitt, R. W. (1996). Intense mixing of Antarctic Bottom Water in the equatorial Atlantic Ocean . *Nature*, 380:54–57.

Poulain, P.-M., Warn-Varnas, A., and Niiler, P. (1996). Near-surface circulation of the Nordic seas as measured by Lagrangian drifters. *J. Geophys. Res.*, 101:18237–18258.

Pratt, L. J. and Armi, L. (1987). Hydraulic control of flows with nonuniform potential vorticity. *J. Phys. Oceanography*, 17:2016–2029.

Pratt, L. J. and Lundberg, P. A. (1991). Hydraulics of rotating sill and strait flow. *Rev. Fluid Mech.*, 23:81–106.

Price, J. F. and Baringer, M. O. (1994). Outflows and deep water production by marginal seas. *Prog. Oceanography*, 33:161–200.

Price, J. F., Baringer, M. O., Lueck, R. G., Johnson, G. C., Ambar, I., Parilla, G., Cantos, C., Kennelly, M. A., and Sanford, T. B. (1993). Mediterranean Outflow Mixing and Dynamics. *Science*, 259:1277–1282.

Pugh, D. T. (1987). *Tides, Surges and Mean Sea-level, A Handbook for Engineers and Scientists*. John Wiley & Sons.

Reynolds, R. W. and Smith, T. M. (1994). Improved global sea surface temperature analysis using optimum interpolation. *J. Climate*, 7:929–948.

Richardson, P. L., Bower, A. S., and Zenk, W. (2000). A cencus of Meddies tracked by floats. *Prog. Oceanography*, 45:209–250.

Robinson, I. S. (1985). *Satellite Oceanography, An Introduction for Oceanographers and Remote-sensing Scientists*. John Wiley & Sons.

Ross, C. K. (1983). Characteristics of the Overflow Water in the Denmark Strait. *ICES CM 1983/C*, 7.

Rossby, T. (1996). The North Atlantic Current and Surrounding Waters: At the Crossroads. *Rev. Geophysics*, 34(4):463–481.

Rossby, T. and Gottlieb, E. (1998). The Oleander Project: Monitoring the Variability of the Gulf Stream and Adjacent Waters between New Jersey and Bermuda. *Bull. Meteorol. Soc.*, 79(1):5–18.

Rudels, B., Friedrich, H. J., and Quadfasel, D. (1999). The Arctic Circumpolar Boundary Current . *dsr2*, 46:1023–1062.

Rudels, B. and Quadfasel, D. (1991). The Arctic Ocean Component in the Greenland-Scotland overflow. *ICES CM*, 30(C).

Saunders, P. M. (1990). Cold Outflow from the Faroe Bank Channel. *J. Phys. Oceanography*, 20:29–43.

Saunders, P. M. (1994). The flux of overflow water through the Charlie-Gibbs Fracture Zone. *J. Geophys. Res.*, 99(C6):12343–12355.

Saunders, P. M. (2001). *The Dense Northern Overflows*, chapter 6, pages 401–418. Ocean Circulation & Climate, edited by Siedler, Church and Gould. International Geophysics Series.

Scharroo, R. and Visser, P. (1998). Precise orbit determination and gravity field improvement for the ERS satellites . *J. Geophys. Res.*, 103(C4):8113–8127.

Schlax, M. G. and Chelton, D. B. (1994). Detecting aliased tidal errors in altimeter height measurements. *J. Geophys. Res.*, 99:12603–12612.

Schluessel, P., Emery, W. J., Grassl, H., and Mammen, T. (1990). On the Bulk-Skin Temperature Difference and Its Impact on Satellite Remote Sensing of Sea Surface Temperature. *J. Geophys. Res.*, 95(C8):13341–13356.

Schmitz, W. J. and McCartney, M. S. (1993). On the North Atlantic Circulation. *Rev. Geophysics*, 31(1):29–49.

Schneider, N., Miller, A. J., Alexander, M. A., and Deser, C. (1999). Subduction of decadal North Pacific temperature anomalies: Observations and dynamics. *J. Phys. Oceanography*, 29:1056–1070.

Shi, X. B., Røed, L. P., and Hackett, B. (2001). Variability of the Denmark Strait Overflow: A numerical study. *J. Geophys. Res.*, 106(C10):22277–22294.

Shum, C. K., Woodworth, P. L., Andersen, O. B., Egbert, G. D., Francis, O., King, C., Klosko, S. M., Provost, C. L., Li, X., Molines, J.-M., Parke, M. E., Ray, R. D., G., S. M., Stammer, D., Tierney, C. C., Vincent, P., and Wunsch, C. I. (1997). Accuracy assessment of recent ocean tide models . *J. Geophys. Res.*, 102(C11):25173–25194.

Siedler, G., Church, J., and Gould, J. (2001). *Ocean Circulation and Climate, Observing and Modelling the Global Ocean* , volume 77 of *International Geophysics Series*. Academic Press.

Smith, P. C. (1976). Baroclinic instability in the Denmark Strait Overflow. *J. Phys. Oceanography*, 6:355–371.

Stammer, D. (1997). Steric and wind-induced changes in TOPEX/POSEIDON large-scale sea surface topography observations. *J. Geophys. Res.*, 102(C9):20987–21009.

Stammer, D., Bning, C., and Dieterich, C. (2001). The role of variable wind forcing in generating eddy energy in the North Atlantic. *Prog. Oceanography*, 48:289–311.

Stammer, D., Hinrichsen, H.-H., and Käse, R. H. (1991). Can meddies be detected by satellite altimetry ? *J. Geophys. Res.*, 96(C4):7005–7014.

Stammer, D. and Wunsch, C. (1996). *Generation and Distribution of Mesoscale Eddies in the North Atlantic Ocean*, chapter 6, pages 159–191. The Warmwatersphere of the North Atlantic Ocean. Gebrüder Borntraeger, Berlin.

Stammer, D. and Wunsch, C. (1999). Temporal changes in eddy energy of the oceans. *Deep-Sea Res. II*, 46:77–108.

Stammer, D., Wunsch, C., and Ponte, R. (2000). De-Aliasing of Global High Frequency Barotropic Motions in Altimeter Observations. *Geophys. Res. Letter*, 27(8):1175–1178.

Stern, M. E. (1972). Hydraulically critical rotating flow. *Phys. Fluids.*, 15:2062–2065.

Stewart, R. H. (1985). *Mothods of Satellite Oceanography.* Univ. of Cal. Press, Berkeley.

Stommel, H. (1979). Determination of water mass properties of water pumped down from the Ekman layer to the geostrophic flow below. *Proceedings of the National Academy of Sciences*, 76:3051–3055.

Swift, J. H. (1984). The circulation of the Denmark Strait and Iceland–Scotland overflow waters in the North Atlantic . *Deep-Sea Res.*, 31:1339–1355.

Sy, A. (1988). Investigation of large-scale circulation patterns in the central North Atlantic: the North Atlantic Currrent, The Azores Current, and the Mediterranean Water plume in the area of the Mid-Atlantic Ridge. *Deep-Sea Res.*, 35(3A):383–415.

Sy, A., Schauer, U., and Meincke, J. (1992). The North Atlantic Current and its associated hydrographic structure above and eastwards of the Mid-Atlantic Ridge. *Deep-Sea Res.*, 39(5A):825–855.

Tabata, S. (1965). Variability of oceanographic conditions at Ocean Station "P" in the northeast Pacific Ocean. *Trans. R. Soc. Can.*, 15:367–418.

Tapley, B. D. and Kim, M.-C. (2001). *Applications to Geodesy*, chapter 10, pages 371–406. Satellite Altimetry and Earth Sciences, A handbook of Techniques and Applications, Edited by Fu and Cazenave. Academic Press.

Tapley, B. D., Ries, J. C., Davis, G. W., Eanes, R. J., Schutz, B. E., Shum, C. K., Watkins, M. M., Marshall, J. A., Nerem, R. S., Putney, B. H., Kloskko, S. M., Luthcke, S. B., Pavlis, D., Williamson, R. G., and Zelensky, N. P. (1994). Precision orbit determination for TOPEX/POSEIDON. *J. Geophys. Res.*, 99(C12):24383–24404.

Tomczak, M. and Godfrey, J. S. (1994). *Regional Oceanography: An Introduction*. Elsevier, 1 edition.

Turrell, W. R., Slesser, G., Adams, R. D., Payne, R., and Gillibrand, P. A. (1999). Decadal varaibility in the composition of the Faroe Shetland Channel bottom water. *Deep-Sea Res.*, 46:1–25.

Turrell, W. R., Slesser, G., Payne, R., Adams, R. D., and Gillibrand, P. A. (1996). Hydrography of the East Shetland Basin in relation to decadal North Sea variability. *ICES J. Mar. Sci.*, 53:899–916.

Vazquez, J., Perry, K., and Kilpatrick, K. (1998). NOAA/NASA AVHRR Oceans Pathfinder Sea Surface Temperature Data Set Userś Reference Manual, Version 4.0. Technical report, Jet Propulsion Laboratory, National Aeronautics and Space Administration .

Wang, L. and Koblinsky, C. (1997). Can the Topex/Poseidon altimetry data be used to estimate air-sea heat flux in the North Atlantic ? *Geophys. Res. Letter*, 24(2):139–142.

Wesson, J. C. and Gregg, M. C. (1994). Mixing at Camarinal Sill in the Strait of Gibraltar. *J. Geophys. Res.*, 99(C5):9847–9878.

White, M. A. and Heywood, K. J. (1995). Seasonal and interannual changes in the North Atlantic subpolar gyre from Geosat and TOPEX/POSEIDON altimetry. *J. Geophys. Res.*, 100(C12):24931–24941.

White, W. B. and Tai, C.-K. (1995). Inferring interannual changes in global upper ocean heat stroage from TOPEX altimetry. *J. Geophys. Res.*, 100(C12):24943–24954.

Whitehead, J. A. (1989). Internal hydraulic flows in rotating fluids - Applications to oceans. *Geophys. Astrophy. Fluid Dyn.*, 48:169–192.

Whitehead, J. A. (1998). Topographic Control of Oceanic Flows in Deep Passages and Straits. *Rev. Geophysics*, 36(3):423–440.

Whitehead, J. A., Leetmaa, A. A., and Knox, R. A. (1974). Rotating hydraulics of straits and sill flows. *Geophys. Fluid Dyn.*, 6:101–125.

Whitehead, J. A., Stern, M. E., Flierl, G. R., and Klinger, B. A. (1990). Experimental Observations of Baroclinic Eddies on a Sloping Bottom. *J. Geophys. Res.*, 95:9585–9610.

WOCE Data Products Committee (2000). WOCE Global Data: Upper Ocean Thermal Programme, Version 2. WOCE IPO Report No. 171/00, Southampton, U.K.

Woods, J. D. and Barkmann, W. (1986). Alagrangian mixed layer model of Atlantic 18°C water formation. *Nature*, 319:574–576.

Worthington, L. V. (1959). The 18°C water in the Sargasso Sea. *Deep-Sea Res.*, 5:297–305.

Worthington, L. V. (1969). An attempt to measure the volume transport of Norwegian Sea overflow water through the Denmark Strait. *Deep-Sea Res.*, 16:421–432. Supplement.

Worthington, L. V. (1976). *On the North Atlantic circulation*, volume 6. The Johns Hopkins Oceanogr. Stud.

Yan, X.-H., Niiler, P. P., Nadiga, S. K., Stewart, R. H., and Cayan, D. R. (1995). Seasonal heat storage in the North Pacific: 1976-1989. *J. Geophys. Res.*, 100(C4):6899–6929.

Yaremchuk, M. I., Nechaev, D. A., and Thompson, K. R. (2001). Seasonal variation of the North Atlantic Current. *J. Geophys. Res.*, 106(C4):6835–6851.

Zhang, R.-H., Kagimoto, T., and Zebiak, S. E. (2001). Subduction of Decadal North Pacific Thermal Anomalies in An Ocean GCM. *Geophys. Res. Letter*, 28(12):2449–2452.

Zwally, H. J. and Brenner, A. C. (2001). *In Satellite Altimetry and Earth Sciences*, volume 69, chapter 9, pages 351–369. Academic Press. Edited by Fu. L.-L. and Cazenave, A.